Distribution Agreement

In presenting this thesis or dissertation as a partial fulfillment of the requirements for an advanced degree from Emory University, I hereby grant to Emory University and its agents to the non-exclusive license to archive, make accessible, and display my thesis or dissertation in whole or in part in all forms of media, now or hereafter known, including display on the world wide web. I understand that I may select some access restrictions as part of the online submission of this thesis or dissertation. I retain all ownership rights to the copyright of the thesis or dissertation. I also retain the right to use in future works (such as articles or books) all or part of this thesis or dissertation.

Signature:

Clifton Trent Brunson	Date

A Renormalization Group Study of the Ising Model on the Hierarchical Hanoi Networks

By

Clifton Trent Brunson
Doctor of Philosophy
Physics

Stefan Boettcher, Ph.D.
Advisor

David Borthwick, Ph.D.
Committee Member

Fereydoon Family, Ph.D.
Committee Member

H.G.E. Hentschel, Ph.D.
Committee Member

Eric Weeks, Ph.D.
Committee Member

Accepted:

Lisa A. Tedesco, Ph.D.
Dean of the James T. Laney School of Graduate Studies

_____
Date

A Renormalization Group Study of the Ising Model on the Hierarchical Hanoi Networks

By

Clifton Trent Brunson
B.S., West Texas A&M University, 2005

Advisor: Stefan Boettcher, Ph.D.

An abstract of
A dissertation submitted to the Faculty of the
James T. Laney School of Graduate Studies of Emory University
in partial fulfillment of the requirements for the degree of
Doctor of Philosophy
in Physics
2014

Abstract

A Renormalization Group Study of the Ising Model on the Hierarchical Hanoi Networks

By Clifton Trent Brunson

Despite all the remarkable breakthroughs in the area of complex networks over the last two decades, there still lacks a complete and general understanding of effects that occur when long-range connections are present in a system. This thesis explores the Ising model using recursive hierarchical networks called Hanoi networks (HN) as a substrate. Hanoi networks are purely synthetic and are not found in nature, so it is important to establish and not lose sight of why they worth studying. In essence, we are not strictly interested in HNs themselves, but the generalized statements about phase transitions on complex networks that they provide via the renormalization group (RG).

The RG framework on HNs is established in this study and the thermodynamic observables for statistical models are derived from it. Traditionally, the RG has given physicists insight into the critical exponents of a system or model, which leads to universal behavior; however, hyperbolic networks, like the ones currently under investigation, do not contain constant exponents and do not exhibit universality. Instead, it is found that the scaling exponents are functions of the temperature. We ultimately want to answer the questions: What is it about long-range connections that create a break in universal behavior and can complex networks be designed to produce predicted and intended effects in phase behavior? The current state of research is several years or perhaps decades away from fully comprehending the answers to these questions. The research presented here is motivated by these questions, and our contribution here is intended to show a generalized picture of phase transitions on networks.

A Renormalization Group Study of the Ising Model on the Hierarchical Hanoi Networks

By

Clifton Trent Brunson
B.S., West Texas A&M University, 2005

Advisor: Stefan Boettcher, Ph.D.

A dissertation submitted to the Faculty of the
James T. Laney School of Graduate Studies of Emory University
in partial fulfillment of the requirements for the degree of
Doctor of Philosophy
in Physics
2014

To my dear friend, Dr. James C. Espinosa. For inspiring me to pursue a career in physics and for all his selfless acts, encouragement, and motivation.

ACKNOWLEDGEMENTS

Most importantly, I would like to thank my advisor, Dr. Stefan Boettcher. I could fill an entire book of everything I learned from him with chapters dedicated not only to physics, but on how to conduct yourself professionally, how to pursue ideas and interesting problems, and how to maintain a positive attitude and healthy lifestyle. He has influenced me in almost every aspect of my life, and I always try to model my professional demeanor after his.

I am grateful to my committee members, who have shown me nothing but support and encouragement. My thanks to Dr. Eric Weeks, who has always challenged me to address the physical meaning of my research and how it may apply to real-world experiments. At times, these challenges sent me into an existential crisis, but he always made himself available to sit down and masterfully explain the meaning of it all. Dr. H.G.E. Hentschel, who I had the privilege of taking the most courses, inspired me to admire and seek elegant solutions to scientific problems. Thanks to Dr. David Borthwick, whose series of lectures on the Ising model and conformal field theory opened my mind to the power that a simple toy model can hold. He has been nothing but helpful in seeing my thesis to completion. Last, and certainly not least, I would like to express my thanks to Dr. Fereydoon Family, who was the catalyst for inspiring me to pursue a research track in computational physics. The enthusiasm and clarity with which he delivered his graduate statistical mechanics lectures prompted me to sit through the course a second time and dictate every word he said.

Thank you to the other talented faculty members of the Emory University Department of Physics, specifically Dr. Kurt Warncke, Dr. Laura Finzi, and Dr. Connie Roth. During the first two years of my graduate studies, Dr. Warncke helped me enhance my writing

skills significantly and showed me how to write about science properly. My rotation in Dr. Finzi's lab gave me true insight into the contributions that physicists can make in biology. And Dr. Roth showed me how one starts a career as a young scientist after graduate school. Finally, I would like to thank Dr. Raymond DuVarney and Horace Dale for their friendship and sound advice throughout the years.

The pursuit of my graduate studies would not have been possible without the love and support from family members. Most of all, I want to thank my wife, Dr. Clare Fitzgerald, who I met during a 3 a.m. fire drill at Clairmont Campus during my first week of graduate school. She is the one person who was always there with kind words of encouragement when times were most difficult. To my parents, June and Jerry Brunson, who provided a loving Texan home and gave me the freedom to explore my independence even at a young age. I'd like to express my gratitude to my grandparents, Nell and Dinzel Leonard, who taught me that patience and kindness toward others will always result in the best outcome. To my grandfather, the late George Brunson, who's Great Depression upbringing taught me that "you'll get by in this world if you learn a little something about everything." Finally, I'd like to show my appreciation to my sisters, Cindy and Ebbie. They are always there to give me a good dose of humor when I need it the most.

TABLE OF CONTENTS

LIST OF FIGURES

CHAPTER I

INTRODUCTION

1.1 Phases of Matter

Our understanding of how the world works requires that we separate things we want to know about into their elementary components, and then figure out how these components interact. This approach applies to all areas of science, where we are essentially attempting to reverse engineer nature. Physicists use statistical mechanics to study the nature of collections of objects, or ensembles, according to different moments of the distribution of observables. The interaction between individual particles and the rest of the system can be modeled in one of three ways: each particle is considered to be independent, similar to the ideal gas; interactions may occur between neighboring particles, as in lattice models; or there may be long-range interactions between spatially-distant particles in the system, like in complex networks. This brief introduction will cover some of the different models studied with statistical mechanics, the different observables that are measured, and the canonical framework used to learn about the statistical nature of a system.

Phases are the macroscopic properties used to describe a collection of object or systems. Substances are typically described as being in their solid, liquid, or gas phase depending on the environment in which they are observed. Quantitatively, these states of matter can be determined by measuring different properties of the substance, such as its ability to shear, its density or its diffraction pattern. These observables provide insight into the symmetry properties of the system, which are used to define and classify the system.

Describing a system according to its phase extends far beyond the solid-liquid-gas model.

Ferromagnets, for example, have non-zero magnetization when kept below their Curie temperature, T_C. Above this temperature, the coupling between the electron spins loosens, and ferromagnets lose their overall magnetization. Thus, a magnet either operates as a magnet or is simply behaves like an ordinary, unmagnetized piece of metal.

Another classic example of phases is the electrical resistivity of superconductors. A superconductor can either exist in its superconducting state, in which the electrical resistance goes to zero below T_C, or it can exist in its non-superconducting form.

These examples show that a dynamical system can be characterized according to the way certain observables of a system respond to external influences. More generally, if a system's dynamics are described according to its phase point $G(\{q_i\}, \{p_i\})$ with generalized coordinates q_i and generalized momenta p_i, the system's equations of motions and its physical constraints determine the regions where different phases exist in its phase space [30].

In statistical mechanics, the thermodynamics of a system is given by its free energy, F, and its derivatives, which come from the Gibbs' formula

$$e^{-F/k_BT} = \sum_{\{q_i,p_i\}} e^{-H(\{q_i,p_i\})/k_BT}, \tag{1}$$

where the sum on the right-hand side is the sum over all the possible energy states of the system and is referred to as the partition function, often denoted by Z.

$$Z = \sum_{\{q_i,p_i\}} e^{-H(\{q_i,p_i\})/k_BT} \tag{2}$$

The partition function is the sum over all degrees of freedom according to the system's Hamiltonian, $H(q_i, p_i)$, and contains all the statistical information about a system. All phases of matter that a system can occupy are described by the same Hamiltonian, which leads to the discussion of how systems undergo phase transitions [16].

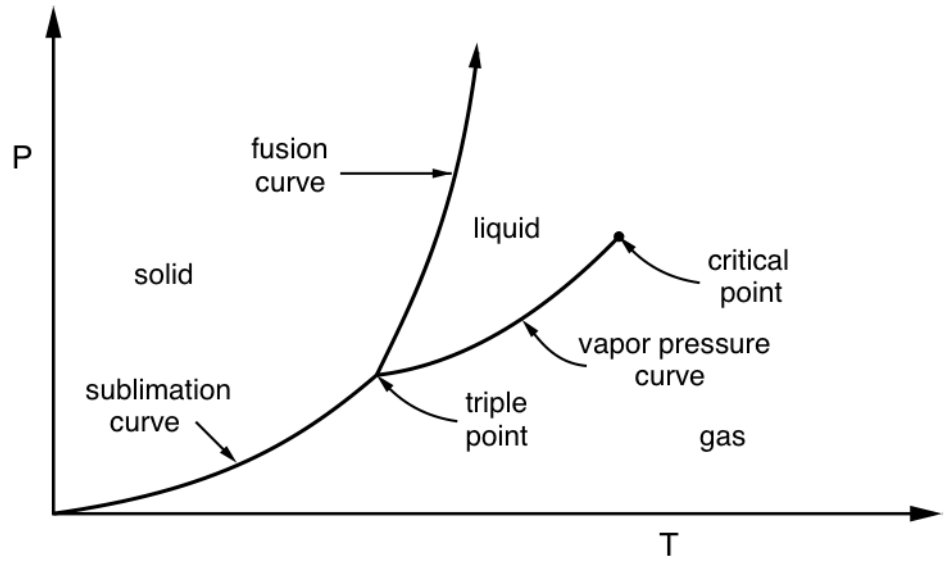

Figure 1: **Phase diagram:** This diagram, taken from Ref. [17], shows the different boundaries that separate the solid, liquid, and gas phases of a system. These types of boundaries are present in every model that undergoes a phase transition. In this study, the primary focus will be the phase diagram of the ferromagnetic behavior of complex networks.

1.2 Phase Transitions

This work examines the ferromagnetic phase transitions that occur when the Ising model is applied to hierarchical, recursive, small-world networks called Hanoi networks. To explain the motivation for studying purely synthetic networks and the dynamics of statistical models on them, it is important to establish the basis for understanding phases transitions in general.

Phase diagrams are plotted against the external parameters that can influence the system. For example, the pressure-temperature phase diagram for water shows the values for these external parameters in which water exists as a solid, liquid, and a gas.

The boundary at which the phase of a substance crosses over to another, shown in Figure 1, carries a substantial amount of information about the system. The system is

completely characterized according to the way it approaches these transition points from both above and below the critical transition point, T_c. Typically, statistical models are studied by varying the temperature while holding the pressure fixed, and T_c is the critical temperature. Above T_c, the entropy, S, dominates the free energy (*viz.* the free energy is minimized by maximizing the entropy), while below T_c, the free energy is dominated by the internal energy, E, and is minimized by minimizing E. If two macrostates of the system exist in these two different cases, a phase transition point exists [31].

The Ising model, a toy model for studying ferromagnetic phase transitions, is arguably the simplest and most thoroughly-studied model for studying phase transitions and will be the primary focus of this study. Figure 2 shows the phase diagram for the Ising model on a two-dimensional lattice. In the lowest energy configuration below the critical temperature T_c, the spins align with the external magnetic field, and the average magnetization per spin approaches one ($m \approx \pm 1$). Above T_c the entropy controls the free energy, and the coupling between the spins becomes loose, which creates a random orientation for each spin and an order parameter close to zero.

As the temperature approaches T_c from above or below, the dimensionality and the symmetry properties of the order parameter dictate how the lattice's universal behavior is classified according to its critical exponents and dimensionality. Models that only account for short-range interactions have been studied extensively and have constant critical exponents. It will be shown later that small-world networks possess critical exponents that are functions of the temperature instead of single values. Small-world networks do not strictly follow the definition a of universality class [16], and much of their critical behavior is classified as non-universal.

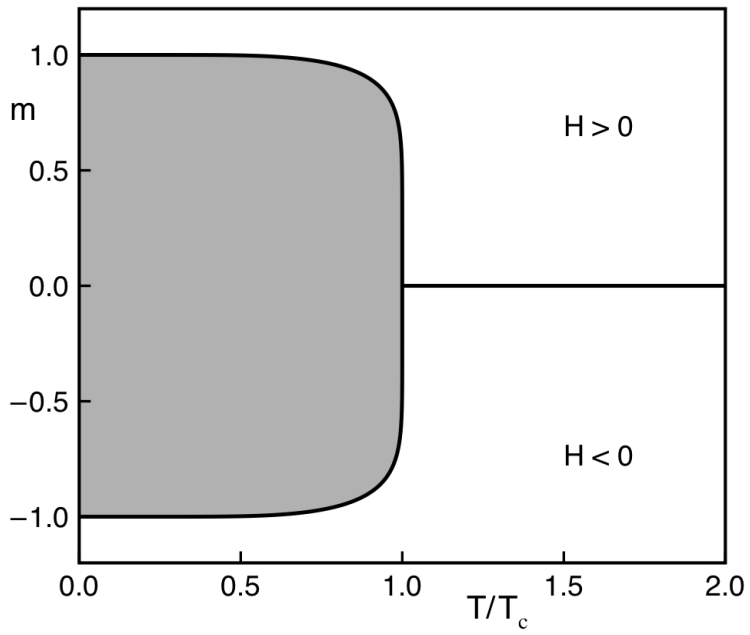

Figure 2: **Ising model phase diagram:** From Ref. [17], this shows the phase diagram for the Ising model. The order parameter is the magnetization m, which undergoes a phase transition at T_c. Below T_c all of the spins in the model are aligned in its lowest free energy state. Above T_c the free energy is dominated by the entropy, and the total magnetization falls to zero.

1.3 The Ising Model

The Ising model is comprised of a simple Hamiltonian, where ferromagnetic spins, σ, can assume the discrete values of either $+1$ or -1 and are coupled with neighboring spins via an exchange interaction, J, via the Hamiltonian

$$-\beta H = J \sum_{<ij>} \sigma_i \sigma_j, \tag{3}$$

where the sum $< ij >$ is over the neighboring spins and $\beta = \frac{1}{k_b T}$ [31]. If the Ising spins are considered to be non-interacting, then the sole term in the Hamiltonian is a Zeeman term for the energy in a magnetic field,

$$-\beta H = \mu B \sum_i \sigma_i. \tag{4}$$

The right-hand sides of Eqs. (3) and (4) can be combined into a complete Hamiltonian for the Ising model,

$$H = -J \sum_{<ij>} \sigma_i \sigma_j - h \sum_i \sigma_i, \tag{5}$$

where βJ and $\beta \mu B$ have been absorbed into the terms J and h respectively. For a system of size N, the partition function is calculated by summing each site over the two possible spin configurations,

$$Z = \sum_{\{\sigma_1 = \pm 1\}} \sum_{\{\sigma_2 = \pm 1\}} \cdots \sum_{\{\sigma_N = \pm 1\}} \exp\left(-J \sum_{<ij>} \sigma_i \sigma_j - h \sum_i \sigma_i \right). \tag{6}$$

This is the expression with which all measurements of the system can be derived. The first derivatives of the logarithm of the partition function (one-point functions) provide the average values of a measured quantity, and the second derivatives (two-point functions) are measurements of the correlations of the system, such as the magnetic susceptibility and

specific heat. This quantities will be derived in detail for the partition functions on the Hanoi networks.

Despite the simplicity of the Hamiltonian, the Ising model, as it will be shown, produces a rich set of results that can be generalized and applied to more complex models. Several decades ago, the Ising model helped physicists understand the concept of universality and scaling laws. Today, these same principles are used to expand our understanding of the consequences long-range interactions have on a system.

The idea of small-world behavior is not new. Graph theory has been around for centuries, but only recently have physicists and mathematicians possessed the computational power to model large, highly-connected systems. The next section will briefly highlight some of the work considered by many to be the most influential and groundbreaking in today's field of complex network research.

1.4 Modern Complex Network Science

The study of complex networks is a common thread of interest in many different research fields [4]. From cellular signaling pathways at the microscopic level to catastrophic power outages at the macroscopic level, the scientific community has made considerable progress over the past two decades in generalizing and classifying the properties of complex networks [6, 13, 14]. The term "small-world" phenomenon was coined by Stanley Milgram as a way to link people in a social sphere [26]. His results led to what is now commonly known as *six degrees of separation* effect [15].

The Watts-Strogatz model, introduced in 1998, borrowed the term "small world" in their paper that ignited the field of network science [34]. In this paper, the authors studied a one-dimensional graph with periodic boundary conditions and edges connecting nearest and next-nearest neighbors. A tunable probability parameter, p, was introduced, where any given vertex might be reconnected to any other vertex in the graph determined by an equal

probability distribution. In this way, the tunable parameter was interpreted as a way to interpolate between ordered and random graphs. This paper pointed out several key points that led to many innovations and realizations in the field of network science. They were,

- Real-world networks are neither completely random nor completely ordered, but somewhere in between.
- The clustering coefficient, C, was defined as a way to quantify local density.
- The average shortest path length, L, was introduced as a global measure of separation.
- Slight changes in network structure can have dramatic effects in its dynamical behavior.
- Important characteristics of real-world networks can be captured by simple models [35].

Shortly after the Watts-Strogatz model was developed, Barabasi and Albert introduced the idea of scale-free networks [3]. In contrast to the Watts-Strogatz model, the Barabasi-Albert model inserted new vertices into the network, which allowed network growth. They also argued that in real-world networks, newly added vertices preferentially attach themselves to well-connected vertices. After taking these two points into consideration, the distribution of edges in this model follows a scale-free power law,

$$P(k) \sim k^{-\gamma}, \tag{7}$$

where P is the probability that a vertex interacts with k other vertices. The results of this model showed that the edges of networks such as actor collaboration networks and the Internet were scale-free networks with typical γ values of $2 < \gamma < 3$. Despite the differences in the two models, the Barabasi-Albert networks are also considered small-world networks,

because they have clustering coefficients much larger than random networks, and their average shortest distance between two vertices increases logarithmically with the number of vertices.

One more breakthrough worth mentioning in the modeling of complex networks was realized in 2000, where Amaral *et al.* found that several complex networks once thought to be scale-free (*i.e.* power grids) had exponentially decaying tails leading to a single scale in connectivity, k. This led them to classify complex networks into three categories:

- Scale-free networks, where the connectivity distribution decays as a power law.
- Broad-scale networks, where a power law decay in connectivity is followed by a sharp cutoff.
- Single-scale networks, where the connectivity distribution has a fast decaying tail as in Gaussian or exponential distributions [1].

From these observations, two additional constraints were added to the Barabasi-Albert model. The first was the concept that vertices can "age." In other words, after a certain amount of time a given vertex will remain part of the network but will be inactive and not receive additional links. The second constraint considered was that vertices can reach a maximum number of connections and that creating additional connections comes at a cost. The inclusion of aging and a cost function into the Barabasi-Albert model recreated the three types of networks seen in different real-world scenarios.

There are generally two approaches of studying statistical models, like the Ising model, on complex networks [32]. One approach is to take a real-world network constructed from its structural data and simplify it with approximations. The results produced by such a statistical model are useful specifically to the network under investigation, but even slight

approximations can have detrimental effects due to the nonlinear nature of complex networks.

A second approach to studying complex networks is to model hierarchical lattices. Hierarchical lattices begin as simple graphs with a small number of vertices and edges, so that the exact partition function can be calculated. Then, the network is constructed using a generating rule that replaces some of the edges with additional vertices and edges recursively. Because the construction of hierarchical lattices are exactly known through generation rules, there are no approximations that need to be made when studying their statistical properties. In other words, hierarchical models can be studied with an exact renormalization group, which has been the framework by which we classify and understand critical phenomena and scaling. It allows us to sort the wide variety of observed phase transitions in materials into an enumerable set of universality classes [31, 36]. The trade-off for having exact results is that hierarchical lattices lose some of their application to real-world networks. However, the motivation for studying hierarchical lattices is to create generalized statements on the dynamics of complex networks as a whole. Additionally, the same approximations that are made on real-world networks can be made on hierarchical networks to compare the effects of the approximations [32].

1.5 Hanoi Networks

The Hanoi networks (HN) are a group of recursive hierarchical networks that produce an exact renormalization group (RG). Each network contains a one-dimensional backbone and is uniquely defined by the way its small-world bonds are distributed. Altogether, there are five different HNs, four of which can be studied with the RG: HN3, HN5, HNNP, and HN6. (The decimation transformation for HN4 does not produce a closed set of recursion equations [10]. The name HN4 belongs to another graph that will not be discussed in this study and that preceded the discovery of HNNP.) The numbers in the HN names indicate

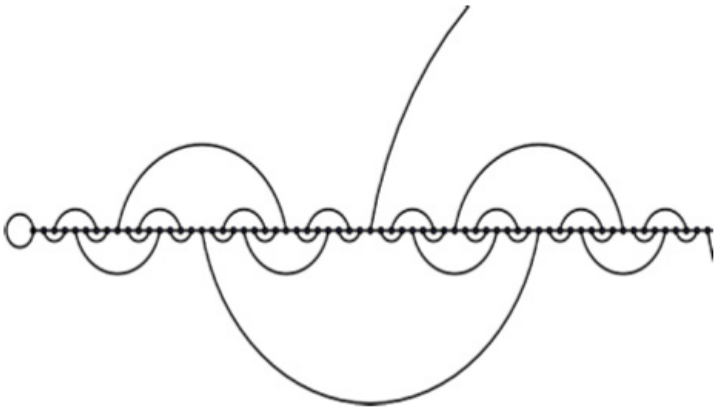

Figure 3: **HN3:** All HNs begin with a one-dimensional Ising chain, and each is defined according to the layout of its small-world bonds. In HN3, every node in the graph connects to its two adjacent backbone neighbors and has exactly one small-world connection.

the average degree distribution of each node in the network as $N \to \infty$, and the non-planar HNNP contains an average degree distribution of 4.

HN3 is a subgraph of HN5, and HNNP is a subgraph of HN6. This complimentary relationship between these two sets of graphs will be used throughout, and a tunable parameter y will be introduced to interpolate between the two graphs. Interpolating between graphs enriches the generalization, because it can be interpreted as adding more weight to small-world bonds to the graph.

1.5.1 HN3

The backbone for each HN is a one-dimensional Ising chain with spins labeled $n = \{0, 1, \ldots, N\}$. The simplest of the Hanoi networks is the HN-3 graph (Figure 3), whose small-world connections are determined by the formula,

$$n = 2^i \left(2j + 1\right), \tag{8}$$

where the i^{th} hierarchy level ($i \geq 0$) of the small-world bonds for $j \geq 0$ belong to node, n. For example, the first hierarchy of bonds are the odd-labeled vertices, where

$$n = 2^0 (2j + 1) = \{1, 3, 5, ...\}. \tag{9}$$

The second level of the hierarchy are all integers that are once evenly-divisible by 2,

$$n = 2^1 (2j + 1) = \{2, 6, 10, ...\}. \tag{10}$$

It is quickly realized that each small-world bond has a backbone length, $L = 2^{i+1} + 1$. The value of j determines whether the small-world neighbor of a node is ahead or behind it along the backbone. Small-world bonds move in the positive direction if the value of $j \,\mathtt{mod}\, 2 = 0$ and in the negative direction if $j \,\mathtt{mod}\, 2 = 1$. For example, the vertex $n = 16$ belongs to the fourth level of the small-world hierarchy. Solving for j gives

$$16 = 2^4 (2j + 1) \rightarrow j = 0, \tag{11}$$

so the small-world bond moves in the positive direction. The vertex $n = 24$, which belongs to the third hierarchical level, has a j value of

$$24 = 2^3 (2j + 1) \rightarrow j = 1, \tag{12}$$

therefore its small-world neighbor is in the negative direction along the lattice.

1.5.2 HN5

HN5 is generated using the same protocol as HN3 except that all nodes belonging to the i^{th} hierarchy are connected to the $\pm 2^i$ neighboring nodes for all $i > 0$. For instance, the set of neighbors for $n = 8$ on HN3 are {7,9,24}, and because $n = 8$ is located in the third hierarchical level (*viz.* 8 is thrice evenly-divisible by 2), it contains six additional small world neighbors, $\text{HN5}_{\text{n=8}} = \{8 \pm 2^3, 8 \pm 2^2, 8 \pm 2^1, 7, 9, 24\}$, for a total of nine neighbors. Figure 4 shows the similarity between HN3 and HN5, where HN3 bonds are shown in black, and HN5 edges are shown in green. Later, a continuous parameter, y, will be multiplied by

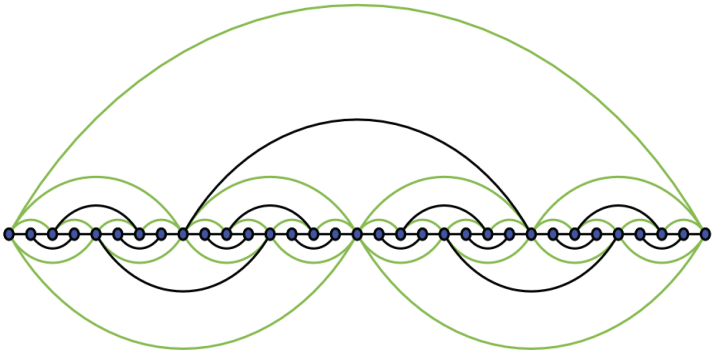

Figure 4: **HN5:** The HN5 graph contains all the elements of the HN3 graph, but with the additional small-world bonds shown in green. As $N \to \infty$, the average degree distribution per node, $< d > \approx 5$.

the HN5 couplings in the Hamiltonian to provide the ability to interpolate between the two networks.

1.5.3 HNNP

The HNNP (NP, meaning non-planar) also contains a one-dimensional backbone of $N_L = 2^L + 1$ nodes. If the combination of $(0 \leq i \leq N_L - 1)$ and $\left(0 \leq j \leq 2^{L-i-2} - 2\right)$ node pairs is considered, nodes $(4j)\,2^i$ and $(4j+1)\,2^i$ are connected to $(4j+3)\,2^i$ and $(4j+4)\,2^i$ respectively [18]. Figure 5 shows an example of HNNP with $N_L = 2^5 + 1 = 32$ nodes. For HNNP in the limit $N \to \infty$, each node in the graph contains an average degree distribution of 4.

1.5.4 HN6

HN6 and HNNP small-world bonds are generated the same way, but HN6 contains additional bonds that are generated according to the HN5 procedure described in Sec. 1.5.2. That is, for each node in the n^{th} hierarchy, small-world bonds are added connecting it to the $\pm 2^i$ neighbors for all $0 < i \leq n$. An example of the differences between HNNP and HN6 are shown in Figure 6, where the blue bonds are those that also make up HNNP and the green

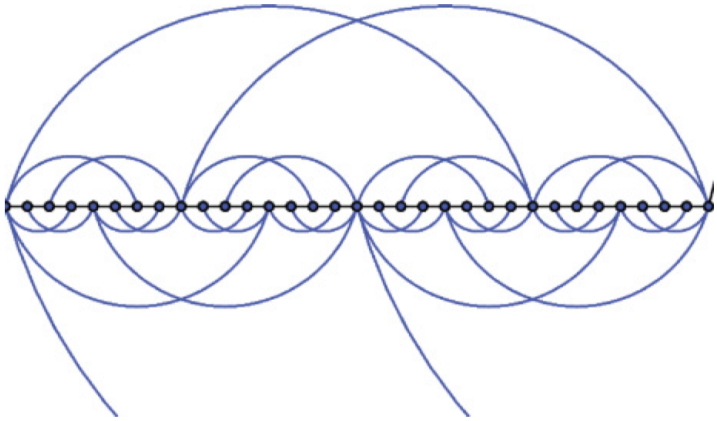

Figure 5: **HNNP:** The HNNP is uniquely defined by its non-planar small-world bonds. Although the name HN4 belongs to a graph that preceded it, HNNP has an average degree distribution of 4, $< d > \approx 4$, as $N \to \infty$.

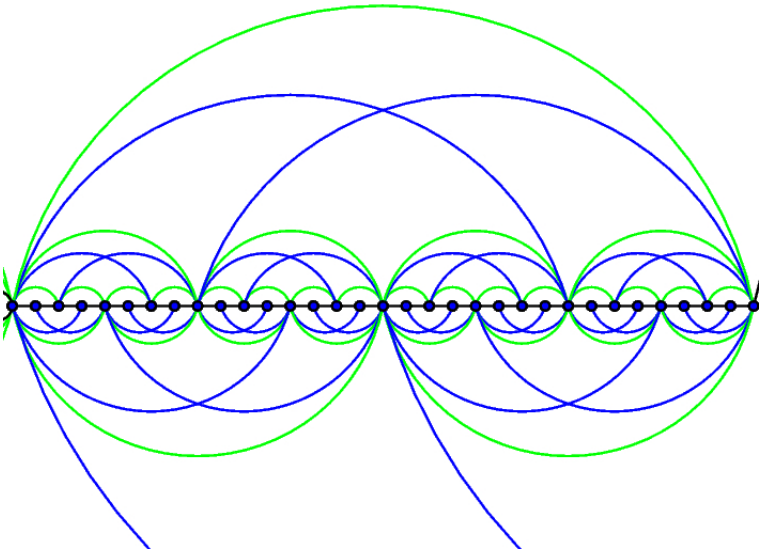

Figure 6: **HN6:** HN6 contains all the elements of HNNP (blue) but with additional small-world bonds (green) that are distributed according to the same protocol that makes HN5 unique from HN3. The terms in the Hamiltonian that account for the green bonds are multiplied by a continuous scaling factor y, which allows for the interpolation between HNNP and HN6.

bonds are the additional HN6 bonds.

To conclude the description of how HNs are generated, it is worth noting that most of the RG results of this work focus on the HN3 and HN5 networks and the interpolation between them. A common theme throughout is that three different phase transitions are proven to exist in recursive hierarchical networks. The interpolation from HN3 to HN5 exhibits all three, whereas the interpolation between HNNP and HN6 only show two. To keep the discussion on a more direct path, HNNP and HN6 will not be discussed in any further detail.

1.5.5 Previous applications of Hanoi networks

The HNs and other similar hierarchical lattices have already been used as a substrates to investigate different types of problems and models. In the bond percolation model, for instance, the one-dimensional version of the Migdal-Kadanoff lattice with a small-world bond showed that at a non-trivial critical point, an explosive cluster growth occurs [12]. At the critical probability point, p_c, the probability that a node belongs to the extensive percolating cluster instantaneously jumps to a finite value. This proved that only small number of small-world bonds are needed to transform a finitely ramified network into an infinitely ramified network. It was also discovered that there are two transition points p_l (lower probability) and p_u (upper probability). Below p_l, the network contains finite-sized clusters with no possible end-to-end path. Above p_u an extensive cluster exists connecting the two ends. For $p_l < p < p_u$, however, there are sub-extensive clusters, which means that a combination of finite clusters may provide an end-to-end path with a certain probability. A similar study on HNNP was performed by Takehisa Hasegawa and Tomoaki Nogawa, where they studied the critical exponents in the three phase regimes [18]. There, they found that a non-percolating phase for HNNP does not exist.

Beyond percolation, the HNs have also been applied to the optimal vertex cover problem

[11], anomalous diffusion [9], and for studying spatial quantum search algorithms [24]. In the vertex cover problem, it was shown that optimal coverages are not related by any simple symmetry. Instead, for each system size, there exists a complex solution space structure, and for $N \to \infty$, the solution landscape is controlled by a large set of similar solutions. The study of anomalous diffusion on HNs revealed that "the golden ratio" appeared in the anomalous exponent for the mean-square displacement of random walks in time. The origin of the golden ratio still remains unknown and is present in the critical temperature of the Ising model for HN5. Finally, the spatial quantum search algorithm, when applied to the HNs, was shown find vertices with degree 4 faster than classical search algorithms.

Applying HNs as a substrate to classical lattice problems has produced a wide variety of rich and complex phenomena, and there remains much to be explored through the exact real-space RG for different models. In essence, this area of study has only scratched the surface for discovering new and interesting phenomena for complex networks. Classifying the effects that long-range bonds have on different models is sure to continue for years to come.

CHAPTER II

THE RENORMALIZATION GROUP AND PHASE DIAGRAMS FOR HANOI NETWORKS

This chapter investigates the phase diagrams that are produced by the Ising model Hamiltonian without an external field parameter. Without the added complexity of an external magnetic field, this provides the simplest introduction for setting up the RG, solving for the recursion equations, and gathering meaningful results about HN behavior.

Sec. 2.1 will discuss the different variables involved in the HN Ising model Hamiltonian and calculate the partition function for the three- and five-spin HN graphlets. This will set the stage for calculating the recursion equations and setting up the RG. In Sec. 2.2, the discussion will go through the recursion equations of the RG in detail and highlight the aspects of critical phenomena that come from them. Finally, Sec. 2.3 will investigate the HN phase diagrams and provide the foundation for understanding the fixed point stability analysis discussed in Chapter 3. There, it will be shown that in general, hierarchical networks can be classified according to three types of behavior near the critical point.

2.1 The Renormalization Group on Hanoi Networks

The RG for hierarchical lattices, which undergoes a decimation transformation, is an easy-to-understand procedure. Starting with an elementary graphlet, like the five-spin graphlet of HN3 in Figure 7, the partition function is calculated, and the internal spins x_{n-1} and x_{n+1} are traced. Then, the partition function is written down for the rescaled, three-spin graphlet shown in Figure 8 using primed variables. Finally, the two partition functions are equated, and solving for the primed variables gives the recursion equations for the RG.

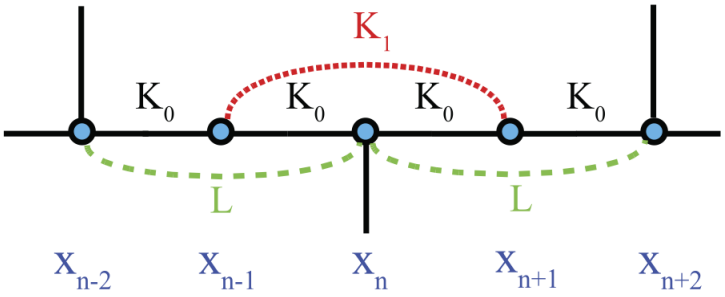

Figure 7: **HN3 five-spin graphlet:** This graphlet shows the short- and long-range coupling constants that make up the HN3 network. K_0 couplings are those along the backbone, K_1 is a small-world bond connecting spins x_{n-1} and x_{n+1}, and the L coupling are small-world bonds that emerge from a previous RG step. They are necessary for creating a closed set of recursion equations.

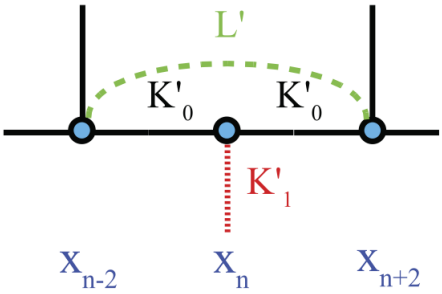

Figure 8: **HN three-spin graphlet:** For the RG, all HNs rescale to identical three-spin graphlets. The primed variables L' and K_0' are solved for in the recursion equations. Since K_1' does not depend on any parameters other than temperature, there is no K_1' recursion equation, and is instead used as a temperature scale throughout this study.

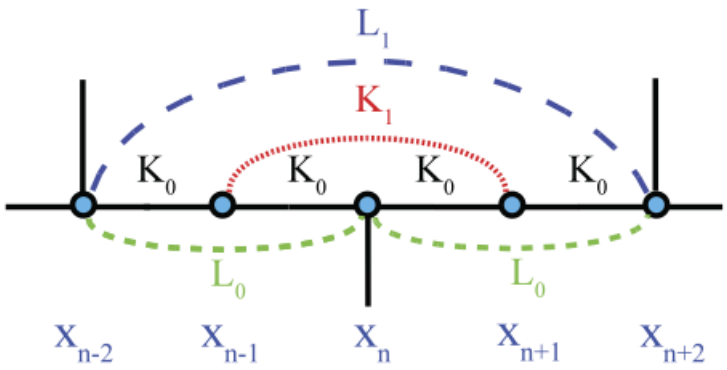

Figure 9: **HN5 five-spin graphlet:** The elementary five-spin graphlet for HN5 contains an extra coupling compared to HN3—the L_1 bond. A tunable parameter y is multiplied by L_1 in the Hamiltonian, which will allow for analysis on interpolative graphs between HN3 and HN5.

The non-trivial fixed points of the recursion equations point to phase transitions, where the system loses its scale length and the correlation length diverges [36].

The principle elements of the RG lie within the properties of the recursion equations and how quickly they flow to a fixed value. The partition functions of the unprimed and primed variables contain all relevant statistical information of the two pictures of the system, and by equating the partition functions, no information is lost after the system is rescaled. Because no approximations are made, the renormalization group for recursive hierarchical networks is exact. This effectively gives the advantage for studying synthetic, recursive networks over real-world networks; it allows for generalized conclusions to be made about networks as a whole with exact solutions.

2.1.1 The HN3 and HN5 Ising Hamiltonian (no external field)

The Ising model Hamiltonian can be separated into hierarchies,

$$-\beta\mathcal{H} = \sum_{n=1}^{k-2} \left(-\beta\mathcal{H}_n\right) + \mathcal{R}\left(K_2, K_3, \ldots\right), \tag{13}$$

where $\mathcal{R}$ contains the couplings of higher-level hierarchies. The variables for the couplings are shown in Figure 9. If K_0 is assigned to the backbone couplings and L_0, L_1, and K_1 are the long-range couplings, each section of the Hamiltonian is

$$\begin{aligned} -\beta\mathcal{H}_n = 4I + K_0(x_{n-2}x_{n-1} + x_{n-1}x_n + x_nx_{n+1} + x_{n+1}x_{n+2}) \\ + K_1(x_{n-1}x_{n+1}) + L_0(x_{n-2}x_n + x_nx_{n+2}) + yL_1(x_{n-2}x_{n+2}), \end{aligned} \tag{14}$$

where I is a constant that fixes the energy scale per spin.

Eq. (14) is the interpolative Hamiltonian between the HN3 and HN5 graphs. The Hamiltonians for HN3 and HN5 only differ by a factor of L_1 (compare Figures 7 and 9), and they both rescale to identical three-spin graphlets (Figure 8) after a spin-decimation step. This allows for there to be a Hamiltonian for HN3, HN5, and the continuous interpolation between them. The interpolating factor y may vary continuously along the interval $0 \leq y \leq 1$, where $y = 0$ is HN3 and $y = 1$ is HN5. (Note: y is allowed to take on values greater than 1, which is reserved for a later discussion. For now, $0 \leq y \leq 1$ will give the results needed to interpolate between HN3 and HN5.)

Writing down the Hamiltonian for the rescaled graphlet (Figure 8) in terms of the corresponding primed variables gives,

$$-\beta\mathcal{H}' = 2I' + K_0'(x_{n-2}x_n + x_nx_{n+2}) + L_0'(x_{n-2}x_{n+2}). \tag{15}$$

Deriving the Hamiltonians is as simple as observing the couplings in the elementary graphlets and connecting them to the relevant spins. Both Hamiltonians are then exponentiated in the next step to give the partition functions.

2.2 The partition functions and recursion equations for HN3 and HN5

The partition function contains all the statistical information about a system in equilibrium and is calculated for the five- and three-spin HN graphlets. To simplify the interpretation

of the phase diagrams and the recursion equations, the HN partition function variables are expressed in terms of activities,

$$C = e^{-4I}, \quad \kappa = e^{-4K_0}, \quad \lambda = e^{-4L_0}, \quad \mu = e^{-2K_1} = e^{-2L_1}. \tag{16}$$

The activities are confined to the interval $[0, 1]$ for the Ising model as opposed to the $[0, \infty)$ interval if the coupling constants were used. Activity values near 0 indicate the strong-coupling, ordered regime often associated with low-temperatures, and activities with values near 1 are associated with high-temperature regimes. The partition functions for the unprimed and primed Hamiltonians are,

$$Z^{(0)} = e^{-\beta \mathcal{H}'_n} = \left(C'\right)^{\frac{1}{2}} \left(\lambda'\right)^{-\frac{1}{4} x_{n-2} x_{n+2}} \left(\kappa'\right)^{-\frac{1}{4} x_{n-2} x_n + x_n x_{n+2}} \tag{17}$$

and

$$Z^{(1)} = e^{-\beta \mathcal{H}_n} = \sum_{\{x_{n-1}=\pm 1\}} \sum_{\{x_{n+1}=\pm 1\}} \left(C^{-1}\right) (\kappa)^{-\frac{1}{4}(x_{n-2}x_{n-1} + x_{n-1}x_n + x_n x_{n+1} + x_{n+1}x_{n+2})} \times (\lambda)^{-\frac{1}{4}(x_{n-2}x_n + x_n x_{n+2})} (\mu)^{-\frac{1}{2}(x_{n-1}x_{n+1}) - \frac{y}{2}(x_{n-2}x_{n+2})}. \tag{18}$$

Carrying out the summations decimates the x_{n-1} and x_{n+1} spins, and the two partition functions are equated. Solving for C', κ', and λ' gives the final version of the recursion equations.

$$\kappa' = \kappa\lambda \frac{2(1+\mu)}{\kappa^2 + 2\mu\kappa + 1} \tag{19}$$

$$\lambda' = \mu^{2y} \frac{(1+\kappa)^2(1+\mu)}{2(\kappa^2 + 2\mu\kappa + 1)} \tag{20}$$

$$C' = C^2 \frac{\kappa\mu}{\sqrt{2}(1+\kappa)(1+\mu)^{\frac{3}{2}}\sqrt{\kappa^2 + 2\mu\kappa + 1}} \tag{21}$$

This completes the initialization of the RG; the recursion equations can be written in a succinct form to emphasize the remapping or rescaling of the system.

$$\begin{aligned} \kappa_{n+1} &= \mathcal{R}_\kappa(\kappa_n, \lambda_n, \mu) \\ \lambda_{n+1} &= \mathcal{R}_\lambda(\kappa_n, \mu) \\ C_{n+1} &= \mathcal{R}_C(\kappa_n, \mu) \end{aligned} \tag{22}$$

Our analysis will be centered mostly around the κ_{n+1} equation and its dependence on the temperature activity parameter, μ.

Once again, HN3 and HN5 only differ by a single factor, which is the μ^{2y} factor in the λ' equation. Setting $y = 0$ gives the recursion equations for HN3, and $y = 1$ are those of HN5.

The conditions used for investigating the trivial and non-trivial fixed points of the recursion equations will be consistent throughout this study. The first condition is that all of the coupling parameters in the Hamiltonian start off on the same footing (*i.e.* all bonds have equal strength). Second, since there is no renormalized quantity for μ, this will effectively act as the temperature scale. The variable $\beta = \frac{1}{k_B T}$ has been combined into the couplings ($\beta J_{K1} \to K_1$), and the activity

$$\mu = e^{-2\beta J_{K_1}} = e^{-2K_1} \tag{23}$$

is $\mu \approx 0$ in the low-temperature regime and is $\mu \approx 1$ as $T \to \infty$. This provides a consistent, independent parameter for plotting the HN phase diagrams.

2.3 Phase Diagrams for HN3 and HN5

All fixed points of the RG occur under the conditions where $\kappa = \kappa' = \kappa^*$ and $\lambda = \lambda' = \lambda^*$. An obvious solution to Eqs. (19, 20) is the trivial low-temperature fixed point, where

$$\kappa^* = 0, \;\; \lambda^* = \frac{\mu^{2y}}{2}(1 + \mu). \tag{24}$$

Interestingly, HN3 (*i.e.* $y = 0$) yields a line of unstable fixed points, and Eq. (24) reduces to

$$\kappa^* = 0, \quad \lambda^* = \frac{1+\mu}{2}. \tag{25}$$

In the low-temperature regime, the initial conditions are $\kappa = \mu^2$ and $\lambda = 1$, since the L_1 does not appear in the HN3 Hamiltonian. By solving Eq. (20) for the variable κ and substituting it into Eq. (19), we eliminate the κ dependence on the right-hand side of Eq. (19).

$$\kappa' = \frac{\lambda\left(1+\mu-2\lambda\mu^{-2y}\right)}{\mu-1} \tag{26}$$

Setting $y = 0$ and applying the initial condition $\lambda = 1$ gives,

$$\kappa' = \frac{(1+\mu-2)}{\mu-1} = 1 \tag{27}$$

From this result, we conclude that even near $\kappa = \mu = 0$, the recursion equations eventually lead to (*viz.* the RG flows toward) $\kappa = 1$, thus HN3 does not have a critical temperature, or rather, its critical temperature is $T = 0$. This is similar to the one-dimensional Ising model. Although, we have just seen that HN3 has a critical temperature at $T = 0$, another example is shown in Figure 10. The initial conditions begin at $\lambda = 1$ for different values of κ, and the lines connect the new values of κ and λ when the system is rescaled with the RG. Regardless of the starting value of κ, the RG flow always migrates to the high-temperature fixed point for HN3. Throughout, we concentrate mostly on κ's dependency on μ. Figure 10 is meant to show that even though there lacks a presence of the L_1 in the initial Hamiltonian, it temporarily emerges as a result of rescaling the system through the RG.

For any value of $y > 0$, we consider the initial conditions to $\kappa = \mu^2$ and $\lambda = \mu^{2y}$. To find the non-trivial fixed point for HN5 ($\kappa' = \kappa = \kappa^*$; $\lambda' = \lambda = \lambda^*$; $y = 1$), Eqs. (19) and

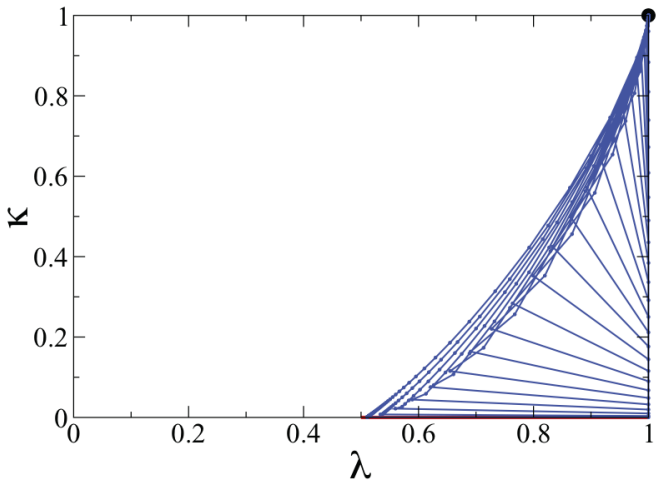

Figure 10: **HN3 phase diagram:** The HN3 phase diagram shows that all initial temperatures lead to the disordered phase. Since there is no L_1 bond in the Hamiltonian for HN3, all initial values for λ are 1. The lines drawn in the phase diagram are connected generations of the recursion equations. All lines flow to the upper-right of the diagram, which is the disordered phase.

(20) are expressed in terms of μ. Eq. (19) becomes

$$1 = \lambda^* \frac{2(1+\mu)}{1+\kappa^{*2}+2\kappa^*\mu}, \tag{28}$$

and substituting Eq. (20) for λ and solving for κ gives

$$\kappa^* = \frac{1}{2}\left(\mu^2 - \mu + \sqrt{(1+\mu)\left(-4+8\mu-3\mu^2+\mu^3\right)}\right). \tag{29}$$

It will be shown that the discriminant of the square root in the fixed-point equations is pivotal for shaping the critical behavior of the system. For simplification, we refer to the discriminants, which are dependent upon y, as $\mathcal{D}_y(\mu)$. Thus, Eq. (29) can be written as,

$$\kappa^* = \frac{1}{2}\left(\mu^2 - \mu + \sqrt{\mathcal{D}_y(\mu)}\right). \tag{30}$$

Also, solving Eq. (19) for κ and substituting the solution into Eq. (20) yields,

$$\lambda^* = \frac{\mu}{4}\left(\mu^2 - \mu + 2 + \sqrt{(1+\mu)\left(-4+8\mu-3\mu^2+\mu^3\right)}\right). \tag{31}$$

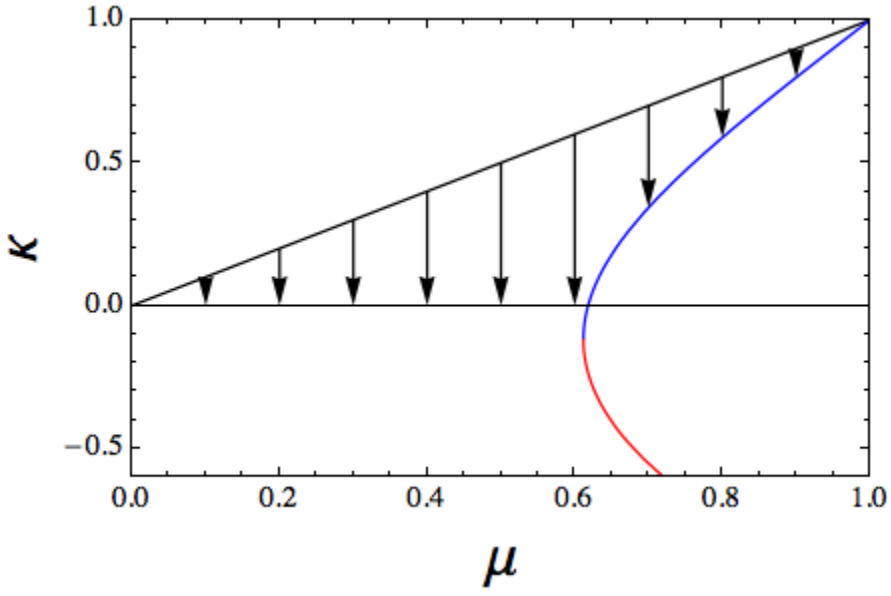

Figure 11: **HN5 phase diagram:** The initial conditions of the HN5 phase diagram shown is along the diagonal $\kappa = \mu$. As the system is rescaled, new values of κ follow the trajectories indicated by the arrows. The black line indicates the initial conditions, the blue line is the stable line of fixed points, and the red line is the line of unstable fixed points.

Eliminating μ from Eqs. (29) and (31) provides the closed form of the equations,

$$\lambda^* = \frac{1}{4}\left(\kappa^* - 1 + \sqrt{5 + 2\kappa^* + 5\kappa^{*2} + 4\kappa^{*3}}\right). \tag{32}$$

Eq. (32) demonstrates that μ can be eliminated for the purpose of studying the κ-λ dependency of the fixed-point recursion equations. For consistency, the focus of our study of phase diagrams and general behavior of the network will instead be centered around the way κ (*i.e.* the backbone couplings) changes with μ (*i.e.* the effective temperature) like the form in Eq. (29).

Let us turn our attention to Eq. (29) for the moment to interpret its meaning. The first distinguishing property is that instead of a single RG fixed point, there is a μ dependency on κ^* that creates a line of stable fixed points.

The physical meaning is made clearer through comparison of the two-dimensional Ising model. For the square 2-D lattice under the initial conditions $\kappa = \mu^2$, there is an interval

$\mu = [0, \mu_c)$, where the recursion equations flow toward the trivial, low-temperature fixed point. At $\mu = (\mu_c, 1]$, the recursion equations flow toward the trivial, high-temperature fixed point. At a single critical temperature T_c (μ_c), the Ising system loses its sense of scale and the RG flow sits at the non-trivial fixed point. This is the single point of the phase transition.

A line of stable fixed points means that given different initial conditions, the RG flow for HN5 will flow to different non-trivial fixed points. The line of fixed points and the behavior of the correlation length near T_c is the characteristic that led [20] to label this type of behavior as an inverted-Berezinskii-Kosterlitz-Thouless (BKT) phase transition similar to what is seen in the XY model, where Ising spins are placed on a two-dimensional lattice with an angular rotational degree of freedom [31].

The phase diagram in Figure 11 contains the initial conditions $\kappa = \mu$, which is along the diagonal indicated in black. The stable line of fixed points for HN5 is the blue line, and the unstable line is indicated in red. The square root in Eq. (29) shapes the line, and it is worth noting that the branch point singularity (*i.e.* $\mathcal{D}_y(\mu) = 0$) is positioned at a μ-value below the $\kappa = 0$,

$$\mu(\mathcal{D}_y(\mu) = 0) < \mu(\kappa = 0). \tag{33}$$

Later in the discussion we will see that the location of the branch point singularity dictates whether the system will undergo one of three types of phase transition. One of these transitions occurs (as in the case of HN5) when the branch point lies below the x-axis. The other two type of phase transitions occur when it lies above the x-axis and when it lies directly on the x-axis.

Now consider what the line of fixed points in HN5 entails. Rather than there being a single point at which a phase transition occurs, there is a series of temperatures where the RG condenses onto the line of fixed points. Each point on the line is neither a fully ordered

nor disordered state, instead the system exists in what we have called a "patchy" phase, which is a quasi-ordered state containing sub-extensive clusters [8]. Another intriguing observation about the system is that even as $\mu \to 1$ ($T \to \infty$), the RG flow always moves to a more ordered state.

The location for T_c for a system that exhibits this type of phase behavior is defined as the μ-intercept of the recursion equations, because this is where the RG flows shows the most dramatic change in behavior.

For HN5, T_c is calculated by setting the left-hand side of Eq. (29) to zero and solving for μ. The result is:

$$\begin{aligned} \mu_c &= \frac{\sqrt{5}-1}{2} \\ T_c &= -\frac{2}{\ln \mu_c} = 4.15617\ldots \end{aligned} \tag{34}$$

The algebraic expression for $\mu_c = \frac{1}{\phi}$, where ϕ is the Golden Ratio. It is not known whether this anecdotal result contains any significance and is not investigated any further.

This concludes the discussion of the specifics of HN3 and HN5. The next section will highlight the phase behavior of the interpolation between these two graphs. Specifically, we will focus on the square root behavior of the fixed point equations and track the branch point singularity as a function of y.

CHAPTER III

FIXED POINT STABILITY ANALYSIS

3.1 Interpolating Between HN3 and HN5

Eq. (20) is substituted into Eq. (19) giving an expression for κ' that depends on both μ and y.

$$\kappa' = \mu^{2y} \frac{\kappa \left(1+\kappa\right)^2 \left(1+\mu\right)^2}{\left(1+\kappa^2+2\kappa\mu\right)^2} \tag{35}$$

At the fixed point $\kappa' = \kappa = \kappa^*$, the non-trivial solution is,

$$\begin{aligned} 1 &= \mu^{2y} \frac{\left(1+\kappa^*\right)^2 \left(1+\mu\right)^2}{\left(1+\kappa^{*2}+2\kappa^*\mu\right)^2} \\ \kappa^* &= \frac{1}{2}\left(-2\mu+\mu^y+\mu^{1+y} \pm \sqrt{\mathcal{D}_y(\mu)}\right), \end{aligned} \tag{36}$$

where $\mathcal{D}_y(\mu) = 4\left(-1+\mu^y+\mu^{1+y}\right) + \left(-2\mu+\mu^y+\mu^{1+y}\right)^2$. This line of stable fixed points is obviously dependent upon μ and y, and the root term dominates the characterization of the phase behavior. The positive square root solution, also referred to as the upper branch, forms the line of stable fixed points. The lower branch containing the negative square root solution is unstable. We will characterize the phase behavior of the interpolation between HN3 and HN5 by tracking the position of the branch point (*i.e.* $\mathcal{D}_y(\mu) = 0$) as y is changed.

If the expression for κ^* in Eq. (36) is substituted back into Eq. (31), then we also have a similar expression for $\lambda(\mu)$,

$$\lambda^* = \frac{1}{4}\mu^y\left(2-2\mu+\mu^y+\mu^{1+y}+\sqrt{\mathcal{D}_y(\mu)}\right). \tag{37}$$

Analysis on the fixed-point stability of the recursion equations provides insight into the correlation length near the critical temperature. It is here where we will discover three types of phase behavior that are present in hierarchical networks with the interpolation from HN3 to HN5 exhibiting all three. (The interpolation from HNNP to HN6 and the Migdal-Kadanoff diamond lattice with a small-world bond see only two of the three phases.)

3.2 The branch point as a function of y

We begin by returning to Eqs. (29), (31), and (32) from Chapter 2 and plotting the phase diagrams for a few selected values of y.

Figure 12 combines four phase diagrams to show how the upper branch of stable fixed points and the square root singularity sunset into the μ-axis as y is increased. Similar to the phase diagrams in Chapter 2, the initial conditions are once again $\kappa = \mu$, which lies along the diagonal of the phase diagram. The arrows indicate the flow of the RG, and it is obvious that for small values of y (close to HN3: Figure 12, upper-left), there lacks an ordered phase, but the beginnings of the stable line of fixed points begins to emerge. The ordered phase becomes more prominent at $y = 0.2$ (Figure 12, upper-right), and the "patchy" behavior is more evident, where above T_c the RG never reaches a completely unstable state.

The branch point singularity intersects with the μ-axis at an analytically-solvable value of $y = \frac{\log 3/2}{\log 2}$. This is easily determined by setting the discriminant in Eqs. (36) and (37) to zero and finding the roots of the results. Conveniently, there is a Mathematica command for this, but another way to look at it is as if the critical point couplings were expressed as,

$$\begin{bmatrix} \kappa^*(\mu_c) \\ \lambda^*(\mu_c) \end{bmatrix} = \begin{bmatrix} -\mu_c + \frac{\mu_c^y}{2}(1+\mu_c) \\ \frac{\mu_c^y}{2}(1-\mu_c) + \frac{\mu_c^y}{4}(1+\mu_c) \end{bmatrix}, \tag{38}$$

then the solution to the simultaneous equations for $\kappa^* = 0$ is

$$y = \frac{\log 3/2}{\log 2} \quad \text{at} \quad \mu_c = \frac{1}{2}. \tag{39}$$

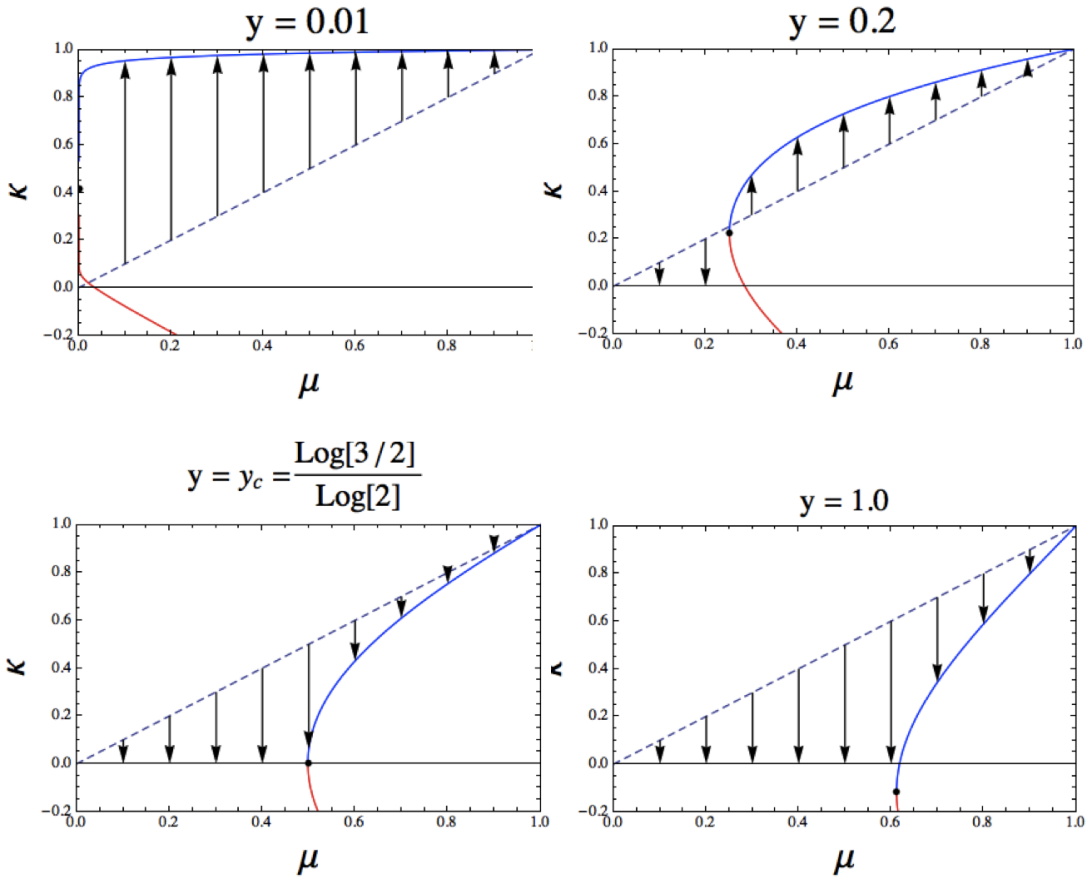

Figure 12: **Phase diagrams for interpolation between HN3 and HN5:** As y is increased, a stable line of fixed points becomes present in the phase diagrams. The arrows in these plots originate from the diagonal, which represents the initial conditions $\kappa = \mu$, and point in the direction of the RG flow. It is obvious from the figures that a square root term dominates the phase behavior with the branch point sunsetting into the μ-axis. The μ-intercept for the branch point is analytically $y = \frac{\log 3/2}{\log 2}$, and it continues to move below $\kappa = 0$ as $y \to 1$.

Beyond this point, the branch point dips below the μ axis (Figure 12, lower-right).

Figure 12 gives a rough sketch of the behavior of the line of fixed points that emerge from the recursion equations; however, there is no particular reason why y can't become greater than 1. In fact, the y value is just an indicator of the ratio of the relative strengths of the backbone and long-range couplings. $y = 2$ for instance would indicate that the L_1 bonds in the Hamiltonian are twice as strong as those in the backbone. As y continues to increase, the backbone bonds are overshadowed by the long-range connections.

As for the branch point, Figure 13 shows that it asymptotically approaches $\mu = 1$. It appears that the branch point migrates logarithmically, but upon examining the Figure 13 inset, we see that there is a slight elbow between $0 < y < 0.1$. This sigmoidal shape is more prominent when we take the logarithm of y and plot the corresponding μ for the zero discriminant in the recursion equations as in Figure 14. In this figure, the left axis is the HN3 case and the vertical line at $\log(y) = 0$ is HN5.

Next, we track where the branch point lies on the κ-axis as y is increased. The black line in Figure 15 shows the rate at which the branch point approaches, then passes the μ-axis. As was shown earlier, the vertical red dashed line indicates $y_c = \frac{\log 3/2}{\log 2}$ where $\kappa = 0$. The blue line is the derivative of the black line to show the rate of change; the red point at the trough indicates the value of y where the branch point decreases or "sunsets" into the $\kappa = 0$ line.

Figures 13, 14, and 15 display exactly how the branch point changes as the strength of the long-range couplings of L_1 increase. As $y \to \infty$, the system eventually reaches a state where all RG flow moves to the low-temperature ordered state.

3.3 Fixed point stability and correlation length

Carrying out the steps described in Ref. [30], the scaling of the divergence of the correlation length can be determined near the transition point. At μ_c, the recursion equations at the

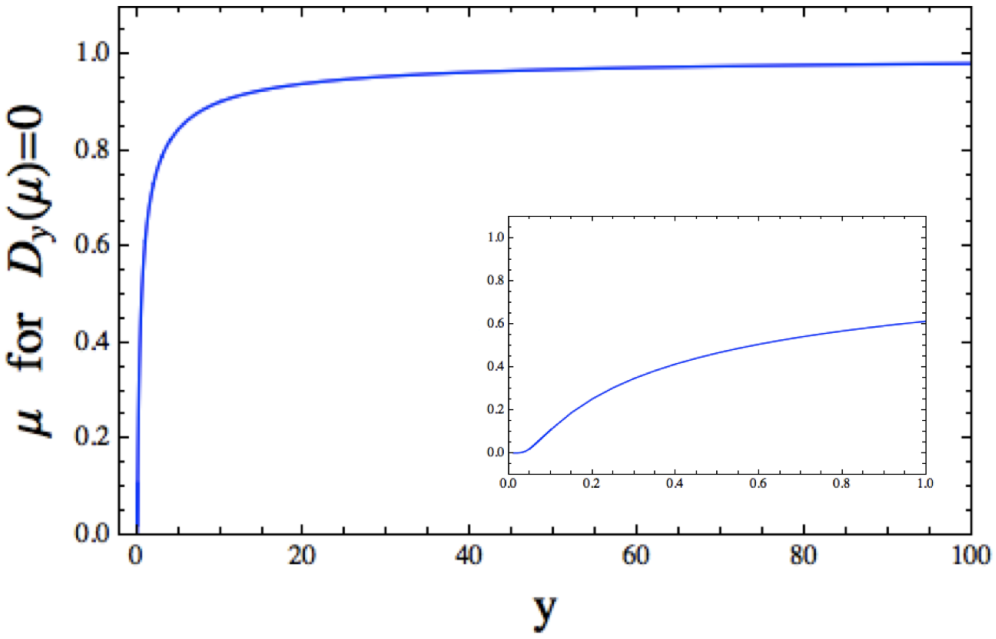

Figure 13: **Movement of the branch point along the μ-axis:** This shows the horizontal movement of the branch point along the μ-axis from Fig. 12 for $0 < y < 100$ (inset: $0 < y < 1$).

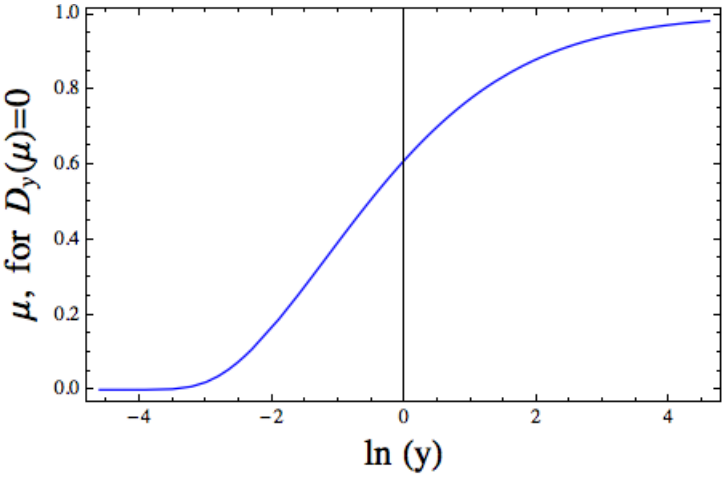

Figure 14: **Log scale of movement of the branch point along the μ-axis:** Similar to Figure 13, this plot shows the horizontal movement of the branch point as y moves along eight orders of magnitude in e.

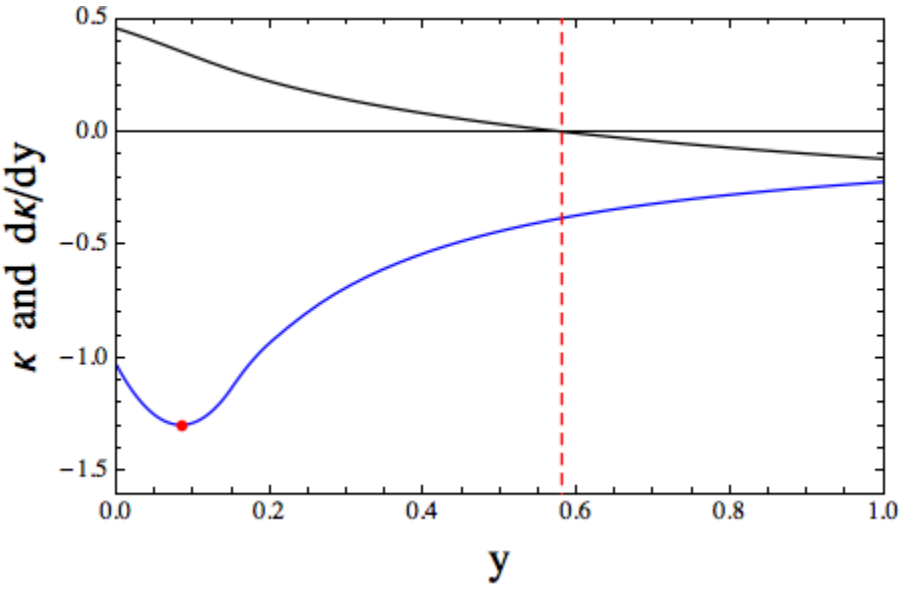

Figure 15: **Movement of the branch point along the κ-axis:** Shown is the position of the branch point along the κ-axis. The black line indicates the branch point position, and the blue line is the velocity of the branch point, $\frac{d\kappa}{dy}$. It is not know whether the minimum value holds any particular significance. The red dashed line shows the point where the branch point intersection with the $\kappa = 0$ line at $y_c = \frac{\log 3/2}{\log 2}$.

fixed points follow

$$\begin{aligned}\kappa^* &= \mathcal{R}_\kappa\left(\kappa^*, \lambda^*, \mu_c\right) \\ \lambda^* &= \mathcal{R}_\lambda\left(\kappa^*, \lambda^*, \mu_c\right),\end{aligned} \tag{40}$$

which can be condensed into,

$$\mathbf{K}^* = \vec{\mathcal{R}}(\mathbf{K}^*). \tag{41}$$

At a small step ϵ_n away from κ^* and a small step δ_n away from λ^*, we examine the RG flow by substituting,

$$\mathbf{K} = \mathbf{K}^* + \mathbf{k} \tag{42}$$

into the recursion equations. (ϵ_n and δ_n are combined into a vector, $\mathbf{k}$.) The substitution produces

$$\mathbf{K}' = \vec{\mathcal{R}}\left(\mathbf{K}^* + \mathbf{k}\right) = \mathbf{K}^* + \mathbf{k}', \tag{43}$$

and solving for $\mathbf{k}'$, which is the vector containing the elements ϵ_{n+1} and δ_{n+1}, and linearizing the results gives us the set of equations,

$$\mathbf{k}' \approx \left.\frac{d\vec{\mathcal{R}}}{d\mathbf{K}}\right|_{\mathbf{K}=\mathbf{K}^*} \mathbf{k}. \tag{44}$$

Expanding the largest eigenvalue of this matrix reveals how the correlation length diverges near the chosen fixed points at μ_c.

For HN5, Eq. (44) can be expressed in matrix form,

$$\delta\mathcal{R}(\kappa^*, \lambda^*) = \begin{bmatrix} A\ \epsilon_n & B\ \delta_n \\ C\ \epsilon_n & 0 \end{bmatrix}, \tag{45}$$

where the coefficients A, B, and C are the expressions accompanying the ϵ_n and δ_n terms. The eigenvalues of this matrix, plotted in Figure 16, are $|\alpha_\pm| < 1$ for $\mu > \mu_c$.

$$\begin{aligned}\alpha_\pm = \ & -\big(\,2 - \mu - 2\mu^2 + \mu^3 - \sqrt{\mathcal{D}_{y=1}(\mu)} + \mu\sqrt{\mathcal{D}_{y=1}(\mu)} \pm \sqrt{2}\sqrt{\big(\,-\big(\,-1 + \mu^2\,\big)} \\ & \big(\,12\mu - 11\mu^2 - 8\mu^3 - 5\mu^4 - 4\mu^5 - 2\sqrt{\mathcal{D}_{y=1}(\mu)} - \mu\sqrt{\mathcal{D}_{y=1}(\mu)} + 7\mu^2\sqrt{\mathcal{D}_{y=1}(\mu)} \\ & + 4\mu^3\sqrt{\mathcal{D}_{y=1}(\mu)}\,\big)\,\big)\,\big) \,/\, (4(-1+\mu)\mu(1+\mu))\end{aligned} \tag{46}$$

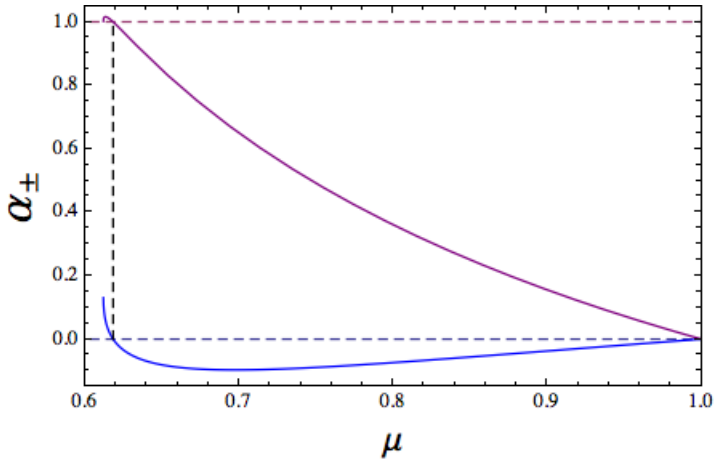

Figure 16: **HN5 eigenvalues from fixed-point stability analysis:** The eigenvalues for HN5 are plotted for $0.6 < \mu < 1.0$. The dominant eigenvalue α_+ is plotted in purple, while α_- is blue.

This means that as the RG is evolved in proximity to the fixed point, the values for ϵ and δ converge to the line of fixed points instead of diverging to infinity, and the fixed points are stable. If a closer look at the the eigenvalues near μ_c is taken, like in Figure 17, it is easier to see to that the positive eigenvalue is unstable for $\mu < \mu_c$, where the $\kappa^* = 0$ solution dominates.

The dominant eigenvalue is $\alpha_+ \approx 1$ near μ_c. To see how it behaves, the eigenvalue is shifted along the μ-axis so that α_+ is presented as a function of $\mu - \mu_c$. Fitting this to a polynomial equation gives the form,

$$\alpha_+ \approx 1 - a_0(\mu - \mu_c) + a_1(\mu - \mu_c)^2 - a_2(\mu - \mu_c)^3 + \cdots , \tag{47}$$

where a_0, a_1, a_2, $\cdots$ are constants. α_+ carries the signature of an exponential decay, which allows us to write,

$$\epsilon_n \sim (\alpha_+)^n \epsilon_0 \sim e^{-\frac{n}{n^*}}, \tag{48}$$

where n^* is a defined cutoff scale.

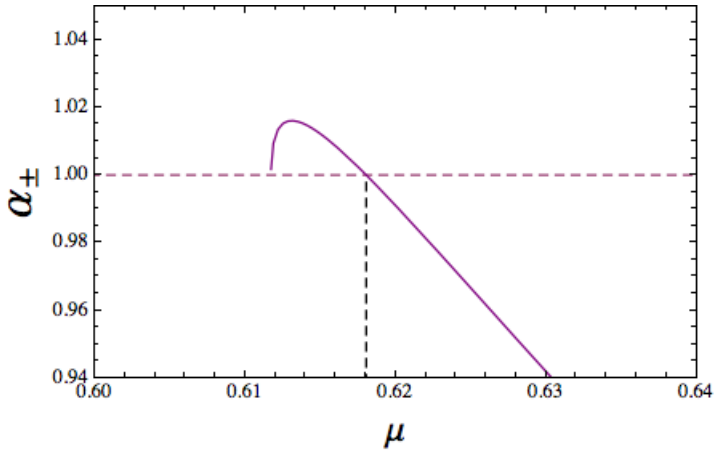

Figure 17: **HN5 eigenvalue near μ_c:** Upon closer inspection near μ_c, the eigenvalue α_+ is unstable ($\alpha_+ > 1$) below μ_c. It is here where the $\kappa^* = 0$ solution takes over and dominates the RG flow to the low-temperature stable fixed point.

A series expansion of α_+ in the neighborhood of $\mu_c = \frac{2}{1+\sqrt{5}}$ from above ($\mu_+ > \mu_c$) gives,

$$\alpha_+ \sim 1 - 2\sqrt{5}(\mu - \mu_c) + \mathcal{O}(\mu - \mu_c)^2. \tag{49}$$

Approaching μ_c from below requires calculating the eigenvalues for the $\kappa^* = 0$ and $\lambda^* = \frac{\mu^2}{2}(1+\mu)$ equations. The dominant eigenvalue for this is

$$\alpha_+ = \mu^2(1+\mu_c)^2. \tag{50}$$

Expanding this in the neighborhood of μ_c (that is, $\mu_- < \mu_c$) gives a very similar result to Eq. (49),

$$\alpha_+ \sim 1 - 2\sqrt{5}(\mu_c - \mu) + \mathcal{O}(\mu_c - \mu)^2. \tag{51}$$

Combining this result with Eq. (49), we write

$$\alpha_+ \sim 1 - 2\sqrt{5}\,|\mu - \mu_c| + \mathcal{O}\,|\mu - \mu_c|^2 \tag{52}$$

Now, for larger systems $n > n^*$, the divergence of the correlation length near μ_c goes as the rescaling of the RG,

$$\xi(\mu) \sim 2^{n^*} = e^{-\frac{\log 2}{\log \alpha_+}}, \tag{53}$$

and we conclude that

$$\xi(\mu) \sim e^{-\frac{\log 2}{2\sqrt{5}|\mu-\mu_c|}} \sim e^{-\frac{const}{|\mu-\mu_c|}}. \tag{54}$$

This is neither power law nor BKT behavior, but rather a third type of phase transition. If we carry through these steps for $y < y_c$, a slightly different result is produced giving the BKT transition, $\xi \sim e^{-\frac{const.}{\sqrt{|\mu_c-\mu|}}}$. At even smaller y values, say $y = 0.05$ the correlation length takes the form of power law scaling, $\xi \sim |\mu_c - \mu|^{-\nu(\mu)}$. In the next section, it will be shown that with increasing y, the HN3-HN5 interpolation networks go through all three types of phase transitions, which will be shown to be a generic result for hierarchical networks.

3.4 A generalized theory for parameter-dependent renormalization

The recursion equations presented thus far in this chapter contain a square root expression, $\sqrt{\mathcal{D}(\mu)}$. Upon closer inspection, the RG flow and the type of phase transition depends on where the branch point of $\sqrt{\mathcal{D}(\mu)}$, and its corresponding value for κ lies in the κ—μ plane as well as the shape of the square root [7].

We argue that this is a general characteristic of parameter-dependent networks like the HNs and the Migdal-Kadanoff lattice. That is, for networks whose RG is expressed by

$$\vec{\kappa}_\infty = \mathcal{R}\left(\vec{\kappa}_\infty; \mu\right), \tag{55}$$

there is some branch point at (μ_B, κ_B). In the neighborhood of μ_B, a generic expression for the RG can be constructed,

$$\mathcal{R}\left(\kappa; \mu\right) \sim a\left(\mu\right)\kappa + b\left(\mu\right)\kappa^2 + c\left(\mu\right)\kappa^3. \tag{56}$$

Normally, one might expect a constant to appear in this type of setting; however, there must be a strong-coupling solution $\kappa^0_\infty = 0$, and a constant would prevent this. For this same reason, there must at least be a cubic-ordered term.

Near μ_B we can assume $(\mu-\mu_B)^3 < (\mu-\mu_B)^2 \ll 1$ and only consider the first-order term $(\mu-\mu_B)$. This leaves us with the following analytical coefficients for $\mu \to \mu_B$:

$$\begin{aligned} a(\mu) &\sim a_0 + a_1(\mu-\mu_B) \\ b(\mu) &\sim b_0 \\ c(\mu) &\sim c_0. \end{aligned} \tag{57}$$

Next, Eqs. (56) and (57) are combined and the BP is located at (μ_B, κ_B). Solving for the fixed point $\kappa' = \kappa = \kappa^*$ and replacing the expressions in Eq. (57) gives,

$$\begin{aligned} \kappa^* &= 0 \\ \kappa^* &= \frac{-b_0 \pm \sqrt{b_0^2 + 4(1-a_0-\mu a_1+\mu_B a_1)c_0}}{2c_0} \end{aligned} \tag{58}$$

This gives the square root in terms of the generic analytic coefficients. If a_1 is eliminated in the limit $\mu \to \mu_B$, solving for a_0 for the case when the discriminant is zero yields,

$$a_0 = \frac{b_0^2 + 4c_0}{4c_0}. \tag{59}$$

The branch point at κ_B is therefore located at

$$\begin{aligned} a_0 &= 1 + c_0\kappa_B^2 \\ b_0 &= -2c_0\kappa_B \\ c_0 &= -1 \end{aligned} \tag{60}$$

c_0 is set to -1, since the branch point needs to be on the low-temperature side of the parabola. Next, we reintroduce a_1 into Eq. (58), and recognize that orienting the branch point correctly demands that $a_1/c_0 < 0$. Thus, we can set $a_1 = -c_0A^2$ with $A > 0$.

Putting it all together, we are left with a minimal model for the parameter-dependent RG,

$$\kappa_{n+1} - \kappa_n \sim \frac{\Delta\kappa}{\Delta n} \sim \left[-\kappa_B^2 + A^2(\mu-\mu_B)\right]\kappa_n + 2\kappa_B\kappa_n^2 - \kappa_n^3. \tag{61}$$

The non-trivial fixed point equation produces a branch point at (μ_B, κ_B):

$$\kappa_\infty^\pm = \kappa_B \pm A\sqrt{\mu - \mu_B}. \tag{62}$$

This equation can generically describe all parameter-dependent renormalization groups near the critical point μ_c. The values of κ_B and μ_B characterize the location of the branch point in the μ—κ plane (see Figure 12), and A determines the shape that the line of stable fixed points takes. It is worth emphasizing that because higher-order terms were not taken into consideration, this minimal model does not apply to μ values further away from μ_c.

Local expansion around the branch point is carried out in the same manner as in the previous section. First, we solve for the fixed point in Eq. (61) for the case $\kappa_{n+1} = \kappa_n = \kappa^*$.

$$\begin{gathered}\left[-\kappa_B^2 + A^2\left(\mu - \mu_B\right)\right]\kappa^* + 2\kappa_B\kappa_n^{*2} - \kappa_n^{*3} = 0 \\ \kappa^* = 0; \quad \kappa^* = \kappa_B \pm \sqrt{A^2\left(\mu - \mu_B\right)}\end{gathered} \tag{63}$$

Applying Eq. (44), substituting $\kappa + \epsilon$ where appropriate, and expanding to first order gives

$$\begin{aligned}\lambda^0 &= 1 - \kappa_B^2 + A^2\left(\mu - \mu_B\right) \\ \lambda^\pm &= 1 \mp 2A\kappa_B\sqrt{\mu - \mu_B} - 2A^2\left(\mu - \mu_B\right).\end{aligned} \tag{64}$$

These eigenvalues are plotted in Figure 18 for $\kappa_B = \frac{1}{2}$ and $A = 1$ and show that below μ_B the λ^0 dominates, which corresponds to the κ_∞^0 solution. At $\mu = \mu_B$, the $\lambda^\pm$ eigenvalues emerge simultaneously with marginal stability, and λ^- remains unstable ($\lambda^- > 1$) until it drops below κ_∞^0 at $\mu - \mu_B = 1/4 = 0.25$. At this point, setting $\kappa_B \to -\kappa_B$ simply swaps $\lambda^\pm \to \lambda^\mp$, and a marginally stable intersection occurs at $\mu_c > \mu_B$ with the intersection of $\lambda^0(\mu_c) = \lambda^+(\mu_c) = 1$.

When the same techniques from the previous section for studying the correlation length are applied to our generic RG model, we get the same results for the three different types of phase transitions for different values of κ_B and A.

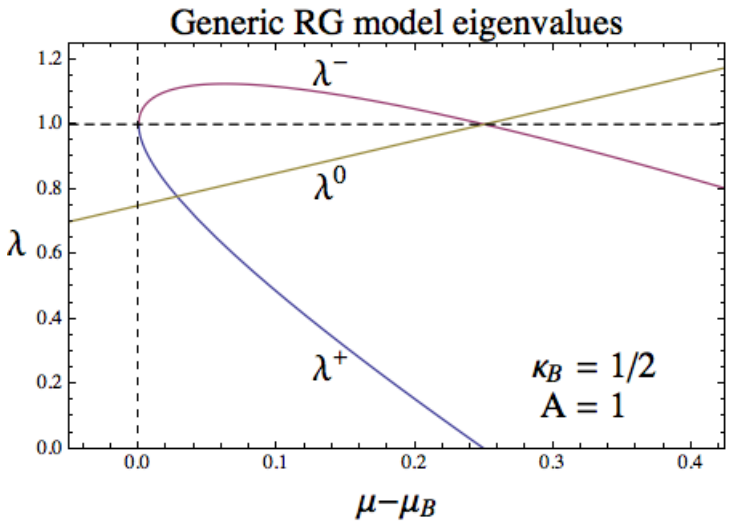

Figure 18: **Generic model eigenvalues:** Substituting the values $\kappa_B = 1/2$ and $A = 1$ gives the following eigenvalues that correspond to the three solutions to the fixed point equation.

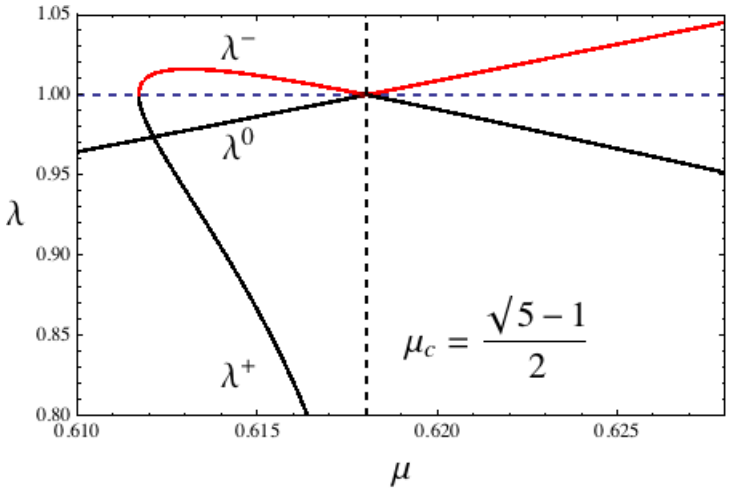

Figure 19: **HN5 eigenvalues for fixed-point equations:** Solving for the solutions for the fixed point equations for HN5 gives three solutions. The low-temperature fixed-point solution has an eigenvalue of λ_0, and the line of fixed points gives two solutions due to the square root. This figure can be compared with Figure 18 to show that the generic model for the RG agrees with the results of HN5. At μ_c, shown with a vertical dashed line, an instability occurs as a result of the intersection of the $\kappa^* = 0$ solution and the line of fixed points.

Figure 19 is shown as an example of how well this generic model fits with the results of HN5. It is clear to see that μ_c derived from the recursion equations is not the branch point, which may not be obvious from the lower right plot in Figure 12.

This concludes our examination of the RG behavior without an external magnetic field present. In the next chapter, we will introduce three additional variables to the Ising Hamiltonian and derive expressions for calculating one- and two-point operator functions as well as calculate critical exponents and the most fundamental quantities for characterizing criticality, y_t and y_h.

CHAPTER IV

DERIVATION OF HANOI NETWORK THERMODYNAMIC DENSITIES FROM THE RG

4.1 Hanoi Network Hamiltonian with an External Magnetic Field

Up to this point, the external magnetic field has been omitted from the Hamiltonian for simplicity. Despite the omission, a remarkable result became evident when studying the phase behavior near our defined temperature activity μ_c. The interpolation between the HN3 and HN5 graphs creates three different types of divergence of the correlation length: a power law divergence dependent upon temperature, $\xi \sim |\mu_c - \mu|^{-\nu(\mu)}$; an inverted BKT divergence, $\xi \sim e^{\frac{\text{const.}}{\sqrt{|\mu_c-\mu|}}}$; and an exponential divergence slightly different from the inverted BKT transition, $\xi \sim e^{\frac{\text{const.}}{|\mu_c-\mu_c|}}$.

To calculate the magnetic moment of the Ising model on HNs as well as the magnetic susceptibility, we begin with a slightly different Hamiltonian and use the same procedure discussed in Chapter 2,

$$\begin{aligned} -\beta\mathcal{H}_n = {} & 4I + K_0\left(x_{n-2}x_{n-1} + x_{n-1}x_n + x_nx_{n+1} + x_{n+1}x_{n+2}\right) \\ & + K_1 x_{n-1}x_{n+1} + L_0\left(x_{n-2}x_n + x_nx_{n+2}\right) + y\,L_1 x_{n-2}x_{n+1} \\ & + \frac{H_K}{2}\left(x_{n-2} + 2x_{n-1} + 2x_n + 2x_{n+1} + x_{n+2}\right) + \frac{H_L}{2}\left(x_{n-2} + 2x_n + x_{n+2}\right) \\ & + \frac{T}{2}\left(x_{n-2}x_{n-1}x_n + x_nx_{n+1}x_{n+2}\right), \end{aligned} \tag{65}$$

where B_K and B_L are the external magnetic field elements applied to the K and L bonds. (**Note:** Because there are triangles formed in the five-spin graph, Ref. [37] states that the Hamiltonian requires a three-point operator.) The five-spin partition function expressed in

terms of its activities is then,

$$\begin{aligned} Z^{(1)} = e^{-\beta\mathcal{H}_n} = \; & C^{-1}\kappa^{-\frac{1}{4}(x_{n-2}x_{n-1}+x_{n-1}x_n+x_nx_{n+1}+x_{n+1}x_{n+2})} \\ & \mu^{-\frac{1}{2}(x_{n-1}x_{n+1}+yx_{n-2}x_{n+2})}\lambda^{-\frac{1}{4}(x_{n-2}x_n+x_nx_{n+1})} \\ & \theta^{-\frac{1}{4}(x_{n-2}+2x_{n-1}+2x_n+2x_{n+1}+x_{n+2})}\vartheta^{-\frac{1}{4}(x_{n-2}+2x_n+x_{n+2})} \\ & \tau^{-\frac{1}{2}(x_{n-2}x_{n-1}x_n+x_nx_{n+1}x_{n+2})}. \end{aligned} \tag{66}$$

Once again, there is a y parameter that allows for the interpolation between HN3 and HN5 to occur. There are two activities to describe the magnetic field in addition to those defined in Chapter 2,

$$\theta = e^{-2B_K} \;\text{ and }\; \vartheta = e^{-2B_L}. \tag{67}$$

In addition to the temperature control parameter μ, there is also the control parameter η to represent the magnetic field for this Hamiltonian,

$$\eta = e^{-2H}. \tag{68}$$

Once again, it is evident that μ and η restrict the results to values between 0 and 1. As for the temperature parameter, μ, the couplings K_1 and L_1 do not renormalize, so

$$\mu^2 = e^{-2K_1} \;\text{ and }\; \mu^{2y} = e^{-2L_1}. \tag{69}$$

After tracing over the odd-labeled spins in Eq. (66), we must solve for the primed activities,

$$\begin{aligned} \sum_{x_{n-1}=\pm1}\sum_{x_{n+1}=\pm1} e^{-\beta\mathcal{H}_n} = \; & \left(C'\right)^{-\frac{1}{2}}\left(\kappa'\right)^{-\frac{1}{4}(x_{n-2}x_n+x_nx_{n+2})}\left(\lambda'\right)^{-\frac{1}{4}(x_{n-2}x_{n+2})} \\ & \left(\theta'\right)^{-\frac{1}{4}(x_{n-2}+2x_n+x_{n+2})}\left(\vartheta'\right)^{-\frac{1}{4}(x_{n-2}+x_{n+2})} \\ & \left(\tau'\right)^{-\frac{1}{4}(x_{n-2}x_nx_{n+1})}. \end{aligned} \tag{70}$$

Of particular interest is the behavior of the Ising model as $H \to 0$ in the thermodynamic limit $N \to \infty$. Therefore, the initial conditions to be invoked for the RG are,

$$C_0 = 1, \;\; \kappa_0 = \mu^2, \;\; \lambda_0 = \mu^{2y}, \;\text{ and }\; \theta = \vartheta = \eta = 1. \tag{71}$$

After a considerable amount of algebra and simplification, the RG recursion equations are,

$$\begin{aligned}
\kappa' =& \frac{\kappa\lambda\left(1+\theta^2+2\theta\mu\right)}{\sqrt{\left(\theta^2+\kappa^2+2\theta\kappa\mu\right)\left(1+\theta^2\kappa^2+2\theta\kappa\mu\right)}} \\
\lambda' =& \frac{\mu^{2y}\left(\theta^2+\kappa+\theta\mu+\theta\kappa\mu\right)\left(1+\theta^2\kappa+\theta\mu+\theta\kappa\mu\right)}{\left(1+\theta^2+2\theta\mu\right)\sqrt{\left(\theta^2+\kappa^2+2\theta\kappa\mu\right)\left(1+\theta^2\kappa^2+2\theta\kappa\mu\right)}} \\
\theta' =& \theta\,\vartheta\left(\frac{\theta^2+\kappa^2+2\theta\kappa\mu}{1+\theta\kappa(\theta\kappa+2\mu)}\right)^{1/4}\sqrt{\frac{\kappa+\theta(\theta+\mu+\kappa\mu)}{1+\theta(\mu+\kappa(\theta+\mu))}} \\
\vartheta' =& \left(\frac{\theta^2+\kappa^2+2\theta\kappa\mu}{1+\theta\kappa(\theta\kappa+2\mu)}\right)^{1/4}\sqrt{\frac{1+\theta(\mu+\kappa(\theta+\mu))}{\kappa+\theta(\theta+\mu+\kappa\mu)}} \\
\tau' =& \left(\frac{\theta^2+\kappa^2+2\theta\kappa\mu}{1+\theta\kappa(\theta\kappa+2\mu)}\right)^{1/4}\sqrt{\frac{1+\theta(\mu+\kappa(\theta+\mu))}{\kappa+\theta(\theta+\mu+\kappa\mu)}}
\end{aligned} \tag{72}$$

The recursion equation for the free energy activity C requires a bit more attention to detail when solving for C' with Mathematica. If the activity C and C' are inserted directly into the partition function at the onset of the script, Mathematic encounters a complex infinity error. To resolve this, the variables I and I' are preserved and appear in the partition function as e^{-I} and $e^{-I/2}$ respectively. (The division by 2 in the exponent is there as a normalization factor.) The result of solving for the I' variable gives,

$$\begin{aligned}
I' = 2\mathrm{I} - \frac{1}{4}\log\Bigg[&\frac{1}{\theta^8\kappa^4\mu^4}\left(1+\theta^2+2\theta\mu\right)^2\left(\theta^2+\kappa^2+2\theta\kappa\mu\right)(1+\theta\kappa(\theta\kappa+2\mu))(\kappa+\theta(\theta+\mu+\kappa\mu))^2 \\
&(1+\theta(\mu+\kappa(\theta+\mu)))^2\Bigg]
\end{aligned} \tag{73}$$

Since $C = e^{-4I}$, the previous equation is multiplied by -4 and exponentiated giving,

$$\begin{aligned}
C' = &\frac{C^2}{\theta^8\kappa^4\mu^4}\left(1+\theta^2+2\theta\mu\right)^2\left(\theta^2+\kappa^2+2\theta\kappa\mu\right)(1+\theta\kappa(\theta\kappa+2\mu)) \\
&(\kappa+\theta(\theta+\mu+\kappa\mu))^2(1+\theta(\mu+\kappa(\theta+\mu)))^2
\end{aligned} \tag{74}$$

4.2 The Derivation of One-Point Functions

By definition, the magnetization's relationship to the partition function is,

$$\langle m_i \rangle = \frac{1}{\beta} \frac{\partial \log Z}{\partial H_i}, \tag{75}$$

which can easily be expressed in term of activities for simplification. There is a mixing of variables in the rescaling of the system in the RG, so we must construct a Jacobian matrix derived from the recursion equations. Before deriving the Jacobian though, it helps to express the series of derivatives as a first rank tensor and separate the couplings, $\vec{K}^{(i)}$, and the parameters, $\vec{p}$, upon which the partition function depends,

$$\overleftrightarrow{V}\left(\vec{K}^{(i)};\vec{p}\right) = \frac{\partial \vec{K}^{(i+1)}}{\partial \vec{K}^{(i)}} = \frac{\partial \vec{\mathcal{R}}}{\partial \vec{K}}\left(\vec{K}^{(i)};\vec{p}\right) = \frac{\partial\left(C^{(i+1)},\kappa^{(i+1)},\lambda^{(i+1)},\theta^{(i+1)},\vartheta^{(i+1)}\right)}{\partial\left(C^{(i)},\kappa^{(i)},\lambda^{(i)},\theta^{(i)},\vartheta^{(i)}\right)}. \tag{76}$$

This provides a distinction between the parameters that are renormalized and those that are simply remapped to themselves in the RG. These are combined and rewritten in the form,

$$\vec{A}^{(i)} = \left(\vec{K}^{(i)};\vec{p}\right), \tag{77}$$

to give an even simpler representation for the tensor equations to come. The derivative of a first rank tensor, of course, requires a Jacobian matrix,

$$\overleftrightarrow{W}^{(i)} = \frac{\partial \vec{A}^{(i)}}{\partial \vec{A}^{(i-1)}} = \frac{\partial \mathcal{R}}{\partial \vec{A}}\left(\vec{A}^{(i-1)}\right) = \begin{bmatrix} \overleftrightarrow{V}\left(\vec{K}^{(i-1)};\vec{p}\right) & \frac{\partial \vec{\mathcal{R}}}{\partial \vec{p}}\left(\vec{K}^{(i-1)};\vec{p}\right) \\ \frac{\partial \vec{p}}{\partial \vec{K}^{(i-1)}}\,(=0) & \frac{\partial \vec{p}}{\partial \vec{p}}\left(=\overleftrightarrow{I}\right) \end{bmatrix}, \tag{78}$$

which is initialized to

$$W^{(1)}_{\alpha\beta} = \frac{\partial \mathcal{R}_\beta}{\partial A_\alpha}\left(\vec{A}^{(0)}\right), \tag{79}$$

so after i steps of the RG, we must evaluate $A^{(i)}$ at its realization, W^{i+1}. (The arrows above W have been removed for aesthetic purposes.) For the Hamiltonian currently under investigation, there are five parameters that are renormalized ($\vec{K}^{(i)} = [C^{(i)},\kappa^{(i)},\lambda^{(i)},\theta^{(i)},\vartheta^{(i)}]$) and two that are not ($\vec{p} = [\mu,\eta]$). Therefore, we are left with a 7×7 matrix. This can be

generalized for other cases, where for any n number of renormalized parameters and m the W Jacobian matrix must have dimensions of $(n+m)\times(n+m)$.

Now we examine the rescaling of the partition function and the role that the W matrix plays in measuring thermodynamic observables. The partition function of an unrenormalized network of size $N=2^k$ is denoted as $Z^{(k)}$, which is evaluated as the three-spin graphlet, $Z^{(1)}$, after rescaling.

$$Z^{(k)}\left[\vec{K}^{(0)}\left(\vec{p}\right);\vec{p}\right]=Z^{(1)}\left[\vec{K}^{(k-1)}\left(\vec{p}\right);\vec{p}\right] \tag{80}$$

From here, the one-point functions can now be derived from the derivatives of the partition functions.

$$\begin{aligned}\frac{d}{dA_\alpha^{(0)}}\log Z^{(k)}\left(\vec{A^{(0)}}\right)&=\frac{d}{dA_\alpha^{(0)}}\log Z^{(1)}\left(\vec{A^{(k-1)}}\right)\\&=\frac{dA_\beta^{(k-1)}}{dA_\alpha^{(0)}}\partial_\beta\log Z^{(1)}\left(\vec{A^{(k-1)}}\right)\end{aligned} \tag{81}$$

To put this equation into words, a network of size $N=2^k+1$ has a partition function $Z^{(k)}$. The derivative evaluated at the initial conditions $(\vec{A^{(0)}})$ is the same as the derivative of the rescaled partition function $Z^{(1)}$ evaluated after being rescaled $k-1$ times, where $\vec{A^{(k-1)}}$ represents the rescaled values of the couplings.

An example of the generalized form of Eq. (81) will show how the chain rule is applied to networks that are rescaled. Suppose $k=3$, and Eq. (81) requires that we evaluate,

$$\begin{aligned}\frac{d}{dA_\alpha^{(0)}}\log Z^{(3)}\left(\vec{A^{(0)}}\right)&=\frac{d}{dA_\alpha^{(0)}}\log Z^{(1)}\left(\vec{A^{(2)}}\right)\\&=\frac{dA_\beta^{(2)}}{dA_\alpha^{(0)}}\frac{d}{dA_\beta^{(2)}}\log Z^{(1)}\left(\vec{A^{(2)}}\right)\end{aligned} \tag{82}$$

The derivative, $\frac{dA_\beta^{(2)}}{dA_\alpha^{(0)}}$ is achieved through rescaling and applying the chain rule.

$$\frac{d}{dA_\alpha^{(0)}}\log Z^{(1)}\left(\vec{A^{(2)}}\right)=\frac{dA_\beta^{(1)}}{dA_\gamma^{(0)}}\frac{dA_\alpha^{(2)}}{dA_\beta^{(1)}}\frac{d}{dA_\alpha^{(2)}}\log Z^{(1)}\left(\vec{A^{(2)}}\right) \tag{83}$$

This is just the same as the W matrix—the Jacobian calculated earlier, so for any number of k rescalings, the chain rule produces

$$\frac{d}{dA_\alpha^{(0)}} \log Z^{(k)} \left(\vec{A^{(0)}} \right) = W_{\alpha,\gamma}^{(1)} W_{\gamma,\delta}^{(2)} \cdots W_{\delta,\beta}^{(k-1)} \partial_\beta \log Z^{(1)} \left(\vec{A^{(k-1)}} \right). \tag{84}$$

And simplifying even further, we can write,

$$W_{\alpha,\gamma}^{(1)} W_{\gamma,\delta}^{(2)} \cdots W_{\xi,\omega}^{(k-1)} = \Upsilon_{\alpha,\beta}^{(k-1)}, \tag{85}$$

where for $l > 0$,

$$\Upsilon_{\alpha,\beta}^{(l)} = \Upsilon_{\alpha,\gamma}^{(l-1)} W_{\gamma,\beta}^{(l)}. \tag{86}$$

In its reduced, generalized form, the expression for the one-point operators becomes,

$$\partial_\beta \log Z^{(k)} \left(\vec{A}^{(0)} \right) = \Upsilon_{\alpha,\beta}^{(k-1)} \partial_\beta \log Z^{(1)} \left(\vec{A}^{(0)} \right), \tag{87}$$

where $\Upsilon_{\alpha,\beta}^{(0)}$ is initialized to the identity matrix, $\mathbf{I}$. From this result, expressions for one-point observables like the internal energy and the magnetization can be derived. The internal energy per spin is

$$\begin{aligned} \langle e \rangle &= -\frac{1}{N} \frac{d}{d\beta} \log Z^{(k)} \left(\vec{A}_0 \right) \Big|_{\eta=1} \\ &= -\frac{1}{N} \frac{d\mu}{d\beta} \frac{\vec{A}_\alpha^{(0)}}{d\mu} \Upsilon_{\alpha,\beta}^{(k-1)} \partial_\beta \log Z^{(1)} \left(\vec{A}^{(k-1)} \right) \Big|_{\eta=1} \end{aligned} \tag{88}$$

Remembering that $\mu = e^{-2\beta}$ and that the vector $\vec{A}$ contains the coupling activities and the dependent parameters, $\vec{A} = [C, \kappa, \lambda, \cdots ; \mu, \eta]$, the derivatives in Eq. (88) evaluate to

$$\frac{d\mu}{d\beta} \frac{\vec{A}_\alpha^{(0)}}{d\mu} = -2\mu \left[\frac{dC}{d\mu}, \frac{d\kappa}{d\mu}, \frac{d\lambda}{d\mu}, \cdots ; \frac{d\mu}{d\mu}, \frac{d\eta}{d\mu} \right] = -2\mu \left[0, 0, 0, \cdots ; 1, 0 \right]. \tag{89}$$

Similarly, the magnetization per spin is,

$$\begin{aligned} \langle m \rangle &= -\frac{1}{N\beta} \frac{d}{dH} \log Z^{(1)} \left(\vec{A}_0 \right) \Big|_{\eta=1} \\ &= -\frac{1}{N\beta} \frac{d\eta}{dH} \frac{\vec{A}_\alpha^{(0)}}{d\eta} \Upsilon_{\alpha,\beta}^{(k-1)} \partial_\beta \log Z^{(1)} \left(\vec{A}^{(k-1)} \right) \Big|_{\eta=1}. \end{aligned} \tag{90}$$

In this case, the derivatives are

$$\frac{d\eta}{dH}\frac{d\vec{A}_{\alpha}^{(0)}}{d\eta} = -2\eta\left[\frac{dC}{d\eta}, \frac{d\kappa}{d\eta}, \frac{d\lambda}{d\eta}, \cdots; \frac{d\mu}{d\eta}\frac{d\eta}{d\eta}\right] = -2\eta\left[0, 0, 0, \cdots; 0, 1\right] \tag{91}$$

Now that the equations for the one-point thermodynamic observables have been established, we will move on to deriving expressions for two-point functions before analyzing how the observables behave on HNs.

4.3 Derivation of Two-Point Functions

The two-point operator expressions are move involved and require careful attention to an additional rank in the tensors. Adding another derivative to the results from the previous section gives

$$\begin{aligned}\frac{d^2}{dA_b^{(0)}dA_a^{(0)}}\log Z^{(k)}\left(\vec{A}^{(0)}\right) &= \frac{d^2}{dA_b^{(0)}dA_a^{(0)}}\log Z^{(1)}\left(\vec{A}^{(k-1)}\right) \\ &= \frac{d}{dA_b^{(0)}}\left[\Upsilon_{a,\alpha}^{(k-1)}\partial_\alpha \log Z^{(1)}\left(\vec{A}^{(k-1)}\right)\right].\end{aligned} \tag{92}$$

Applying the chain rule expands the previous equation into two terms,

$$\begin{aligned}\frac{d}{dA_b^{(0)}}\left[\Upsilon_{a,\alpha}^{(k-1)}\partial_\alpha \log Z^{(1)}\left(\vec{A}^{(k-1)}\right)\right] &= \left(\frac{d}{dA_b^{(0)}}\Upsilon_{a,\alpha}^{(k-1)}\right)\partial_\alpha \log Z^{(1)}\vec{A}^{(k-1)} \\ &\quad + \Upsilon_{a,\alpha}^{(k-1)}\left(\frac{d}{dA_b^{(0)}}\partial_\alpha \log Z^{(1)}\vec{A}^{(k-1)}\right)\end{aligned} \tag{93}$$

The parenthetical expression in the last term is easily evaluated using the steps in the previous section.

$$\begin{aligned}\frac{d}{dA_b^{(0)}}\partial_\alpha \log Z^{(1)}\vec{A}^{(k-1)} &= \Upsilon_{b,\beta}^{(k-1)}\partial_\beta\partial_\alpha \log Z^{(1)}\left(\vec{A}^{(k-1)}\right) \\ &= \partial_\alpha\partial_\beta \log Z^{(1)}\left(\vec{A}^{(k-1)}\right)\Upsilon_{\beta,b}^{(k-1)}\end{aligned} \tag{94}$$

Thus, the last term in Eq. (93) is

$$\Upsilon_{a,\alpha}^{(k-1)}\left(\frac{d}{dA_b^{(0)}}\partial_\alpha \log Z^{(1)}\vec{A}^{(k-1)}\right) = \Upsilon_{b,\alpha}^{(k-1)}\left\{\partial_\alpha\partial_\beta \log Z^{(1)}\left(\vec{A}^{(k-1)}\right)\right\}\Upsilon_{\beta,a}^{(k-1)} \tag{95}$$

The derivative of Υ requires another application of the chain rule, since it represents the product of multiple W matrices.

$$\frac{d}{dA_b^{(0)}}\Upsilon_{a,\alpha}^{(l)} = \left\{\frac{d}{dA_b^{(0)}}\Upsilon_{a,\beta}^{(l-1)}\right\} W_{\beta,\alpha}^{(l)} + \Upsilon_{\alpha,\beta}^{(l-1)}\left\{\frac{d}{dA_b^{(0)}}W_{\beta,\alpha}^{(l)}\right\} \tag{96}$$

Similar to the construction of the W Jacobian matrix in Eq. (78), a new term, Ω, will be used to represent the Hessian matrix or the mixing of the second derivatives of the partition function (which is also the first derivative of the W matrix).

$$\Omega_{\nu,\beta,\alpha}^{(l)} \equiv \frac{\partial^2 \mathcal{R}_\beta}{\partial A_\nu \partial A_\alpha}\left(\vec{A}^{(l-1)}\right) \tag{97}$$

With this, the derivative of the W matrix can be expressed as,

$$\frac{d}{dA_b^{(0)}}\left\{W_{\beta,\alpha}^{(l)}\right\} = \left\{\frac{dA_\nu^{(l-1)}}{dA_b^{(0)}}\right\}\left\{\frac{\partial^2 \mathcal{R}_\beta}{\partial A_\nu \partial A_\alpha}\left(\vec{A}^{(l-1)}\right)\right\} = \Upsilon_{\beta,\nu}^{(l-1)}\Omega_{\nu,\beta,\alpha}^{(l)}. \tag{98}$$

Next, we define the derivative of Υ for all $l \geq 0$,

$$\Lambda_{b,a,\beta}^{(l)} \equiv \frac{d}{dA_b^{(0)}}\Upsilon_{a,\beta}^{(l)}. \tag{99}$$

Here, Λ is initially zero ($\Lambda^{(0)} \equiv 0$), and for $l > 0$,

$$\Lambda_{b,a,\beta}^{(l)} = \Lambda_{b,a,\alpha}^{(l-1)} W_{\alpha,\beta}^{(l)} + \Upsilon_{\nu,\beta,\alpha}^{(l-1)}\Omega_{\nu,\beta,\alpha}^{(l)}\widetilde{\Upsilon}_{\alpha,a}^{(l-1)} \tag{100}$$

Eq. (92), with its new defined terms, now becomes,

$$\begin{aligned}\frac{d^2}{dA_b^{(0)}dA_a^{(0)}}\log Z^{(k)}\left(\vec{A}^{(0)}\right) = \Lambda_{b,a,\alpha}^{(k-1)}\left\{\partial_\alpha \log Z^{(1)}\left(\vec{A}_{k-1}\right)\right\} + \\ \Upsilon_{b,\alpha}^{(k-1)}\left\{\partial_\alpha\partial_\beta \log Z^{(1)}\left(\vec{A}^{(k-1)}\right)\right\}\widetilde{\Upsilon}_{\beta,a}^{(k-1)}\end{aligned} \tag{101}$$

This is the final expression used to calculate the two-point functions such as the magnetic susceptibility and the specific heat. To provide an example of how these are calculated

explicitly, the specific heat evaluated at $H = 0$ ($\eta = 1$) is,

$$\begin{aligned} c\left(\beta\right) &= -\frac{1}{N}\frac{d^2}{d\beta^2}\log Z^{(k)}\left(\vec{A}^{(0)}\right) \\ &= -\frac{1}{N}\frac{d}{d\beta}\left[\frac{d\mu}{d\beta}\frac{dA_\alpha^{(0)}}{d\mu}\frac{d}{dA_\alpha^{(0)}}\log Z^{(k)}\left(\vec{A}^{(0)}\right)\right] \\ &= -\frac{1}{N}\left(\frac{d^2\mu}{d\beta^2}\frac{dA_\alpha^{(0)}}{d\mu} + \left(\frac{d\mu}{d\beta}\right)^2\frac{d^2A_\alpha^{(0)}}{d\mu^2}\right)\left\{\frac{d}{dA_\alpha^{(0)}}\log Z^{(k)}\left(\vec{A}^{(0)}\right)\right\} \\ &\quad -\frac{1}{N}\left(\frac{d\mu}{d\beta}\right)^2\frac{dA_\alpha^{(0)}}{d\mu}\frac{dA_\beta^{(0)}}{d\mu}\left\{\frac{d^2}{dA_\alpha^{(0)}dA_\beta^{(0)}}\log Z^{(k)}\left(\vec{A}^{(0)}\right)\right\} \end{aligned} \tag{102}$$

Applying the result of Eq. (101), the specific heat takes the form that is used to generate numerical values in the Mathematica scripts.

$$\begin{aligned} c\left(\beta\right) = &-\frac{1}{N}\left(\frac{d^2\mu}{d\beta^2}\frac{dA_\alpha^{(0)}}{d\mu} + \left(\frac{d\mu}{d\beta}\right)^2\frac{d^2A_\alpha^{(0)}}{d\mu^2}\right)\left\{\Upsilon_{\alpha,\beta}^{(k-1)}\left[\partial_\beta\log Z^{(1)}\left(\vec{A}^{(k-1)}\right)\right]\right\} \\ &-\frac{1}{N}\left(\frac{d\mu}{d\beta}\right)^2\frac{dA_\alpha^{(0)}}{d\mu}\frac{dA_\beta^{(0)}}{d\mu}\left\{\Lambda_{\alpha,\beta,\gamma}^{(k-1)}\left[\partial_\gamma\log Z^{(1)}\left(\vec{A}^{(k-1)}\right)\right]\right\} \\ &-\frac{1}{N}\left(\frac{d\mu}{d\beta}\right)^2\frac{dA_\alpha^{(0)}}{d\mu}\frac{dA_\beta^{(0)}}{d\mu}\left\{\Upsilon_{\alpha,\gamma}^{(k-1)}\left[\partial_\gamma\partial_\delta\log Z^{(1)}\left(\vec{A}^{(k-1)}\right)\right]\widetilde{\Upsilon}_{\delta,\beta}^{(k-1)}\right\} \end{aligned} \tag{103}$$

This concludes the derivations for the one- and two-point operators for hierarchical networks. Although this approach is similar to that of Hinczewski and Berker in Ref. [19], there is one distinct advantage for using the approach just described: the ability to study finite-sized networks. The steps for calculating thermodynamic observables using the technique of Hinczewski and Berker are described in detail in Appendix A. Rather than beginning with the elementary partition function and rescaling the network to size $N = 2^k + 1$, the Hinczewski and Berker method examines networks at the thermodynamic limit, $N \to \infty$, by taking the limit of the partition function derivatives for $J \to 0$ and $J \to \infty$, where J is the backbone coupling parameter. In other words, this method studies the behavior of thermodynamic observables in relation to the fixed points of the RG.

4.4 The temperature and magnetic exponents

We are now equipped with the necessary framework to study to calculate the values of the critical characterization quantities y_t and y_h. These quantities lead to the critical exponents for the power-law singularity in systems where the volume N goes as $L \propto N^{1/d}$, where d is the dimension. HNs and other small-world networks are considered to be "infinite dimensional" where $L \propto \log N$, and standard scaling theories cannot be applied.

Using the recursion equations from Eq. (72), the corresponding $\overleftrightarrow{W}$ Jacobian matrix is constructed for the interpolative HN3-HN5 system containing the y parameter.

When investigating the eigenvalues that make up the recursion equations for the external magnetic field parameters, the $\overleftrightarrow{W}$ matrix can be decoupled from the coupling parameter section. Taking the quadrant containing the derivatives with respect to θ, ϑ, and τ, the magnetic field is initialized to $H = 0$ ($\eta = 1$), and the resulting eigenvalues for this matrix are:

$$\begin{aligned} \lambda^{(0)} &= 0 \\ \lambda^{(1)} &= \frac{(-1+\kappa)(-1+\mu)}{(1+\kappa)(1+\mu)} \\ \lambda^{(2)} &= \frac{2+2\kappa\mu}{1+\kappa^2+2\kappa\mu} \end{aligned} \tag{104}$$

The eigenvalue $\lambda^{(2)}$ corresponds to the λ_h eigenvalue, which yields an RG flow of $\eta_{n+1} \sim \eta_n^{y_h}$. Notice that $y_h \leq 2$, and in particular, $y_h = 2$ for the fixed point $\kappa_+(\mu_c) = 0$. Expanding this into a series to first order produces $y_h \sim 2 - C\kappa_\infty^+(\mu_c)$ with the constant $C > 0$ near the critical point μ_c. The conclusion of Ref. [29] states that for the case where the reduced critical temperature t is not singular, then $y_h = \log \lambda_+$. Therefore, the magnetic exponent needed to satisfy $\lambda_h \leq 2$ is

$$y_h = \log_2 \lambda_h(\mu_c) \leq 2. \tag{105}$$

If we take the entire matrix into account and apply the same strategy, we reach a similar

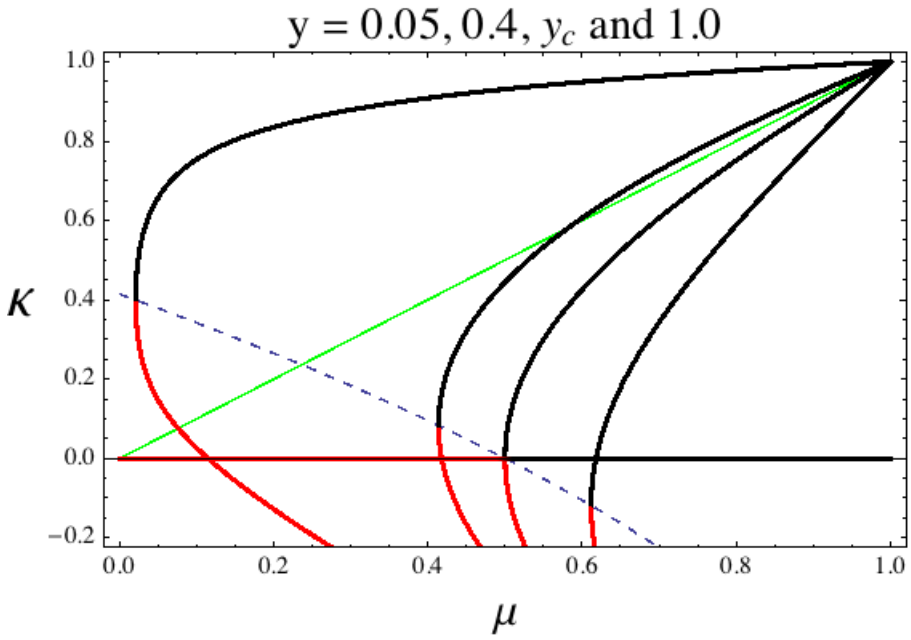

Figure 20: **Phase diagrams for different y values:** This figure is shows the phase diagrams for the different values of y that are plotted in Figures 23, 24, 26, 27, and 28. The values of y were chosen to give examples of the three different types of phase transitions found in HNs. They are $y = 0.05$, 0.4, y_c, and 1.0

result for y_t.

$$y_t = \log_2 \lambda_+ (\mu_c) \tag{106}$$

The scaling theory developed in Ref. [29] explains the relationship that the magnetic exponent y_h has with the order parameter m for the BKT transition. For $y_t \to 0$,

$$m \sim \xi^{-1} \sim \exp\left\{ -\frac{const.\,(1 - y_h)}{(\mu_c - \mu)^{-x_t}} \right\}, \tag{107}$$

and the exponent x_t appears to hold a universal value of $x_t = \frac{1}{2}$.

Of course, for the case where hierarchical networks follow a power law singularity ($y_t > 0$), we can extract the β magnetization exponent with,

$$m \sim (\mu_c - \mu)^{\beta}, \quad \beta = \frac{1 - y_h}{y_t}. \tag{108}$$

For the remaining sections of this chapter, results for the interpolation between HN3 and HN5 will be shown for the y values in Figure 20. These values were chosen as representative of the three types of phase transitions discussed earlier. $y = 0.05$ is squarely in the regime of a power law singularity, $y = 0.4$ is comfortably in the BKT transition, y_c is the value where the branch point meets the $\kappa = 0$ line, and $y = 1.0$ produces a transition of $\xi \sim e^{-\frac{const.}{|\mu_c - \mu|}}$.

4.5 Breaking the Z_2 Symmetry of the Ising Model

It is expected that magnetization plots should align with the results from the discussions in Chapters 2 and 3. That is to say, the phase transitions should occur at the same temperatures indicated by the fixed point of the RG recursion equations. Before examining the magnetization scaling in detail, it must be recognized that because the derivations in the previous section are for finite systems, an external magnetic field must be present to break the Z_2 symmetry. η cannot simply be set equal to one ($H = 0$). What's more, smaller networks require a stronger external field to break the symmetry. This raises the questions: How is the magnetic field determined, and is there a systematic way to determine it? Previous studies, such as the one conducted by Hinczewski and Berker [19], had no need to negotiate this issue, since all of their studies inherently investigated the thermodynamic limit. Nogawa, Hasegawa, and Nemoto were able to achieve a scheme for studying finite system sizes via a scaling theory. Their work provided an exploration into the critical behavior of the magnetization and susceptibility on what is referred to as the hierarchical small world network, also called the one-dimensional Migdal-Kadanoff small world network [29, 28]. Our technique for measuring thermodynamic observables on HNs may be considered a variation on the theme they published—a different approach for producing the same expected results.

To determine the strength of the magnetic field needed to break the Z_2 symmetry, a Mathematica script for numerically calculating the magnetization per spin is run for a large

system size ($N = 2^{1024}$) at a low temperature $\mu = 0.01$ ($T \approx 0.43$) with varying values of H. If the magnetic field is strong enough to break the symmetry, the magnetization per spin should be close to 1. The script produces the following results:

HN5 ($y = 1$), $N = 2^{1024}$, $\mu = 0.01$	Magnetic Field, H	Magnetization per spin, $< m >$
	10^{-309}	≈ 0.177857
	10^{-308}	≈ 0.946565
	10^{-307}	≈ 0.999999

From this, we see that the magnetic field, when increased to $H = 10^{-307}$, is sufficient enough to produce a magnetization value close to 1 for small μ. Unfortunately, the numerical accuracy of Mathematica cannot distinguish a difference in results for values between $10^{-308} < H < 10^{-307}$. Carrying out this procedure for system sizes ranging from 2^{16} to 2^{1024} produces the plot in Figure 21 with which the magnetic field needed to break the Z_2 for HN5 can be estimated. For networks larger than 2^{1024}, Mathematica throws a division by zero exception error due to numerical inaccuracy. From Figure **??**, we see that as $N \to \infty$, the field needed to break the Z_2 symmetry approaches zero.

4.6 Magnetization of Hanoi Networks according to the RG

With the theoretical framework in place and the means for determining the external magnetic field value, the order parameter for the Ising model, or magnetization, will be examined for the interpolation between HN3 and HN5 for the y values indicated in Figure 20. Intuitively, we expect to the same type of behavior as was seen with the correlation length. Starting with a small value for y, there should be a clear discontinuity in the order parameter, which would indicate power law scaling. As $y \to y_c = \frac{\log 3/2}{\log 2} \approx 0.585$, we expect the BKT transition to emerge and eventually work toward a smooth transition of $m \sim e^{-\frac{const.}{|\mu_c - \mu|}}$.

The panels in Figure 23 show the magnetization for $y = 0.05$, 0.4, y_c, and 1 for systems of size $N = 2^8, 2^{16}, 2^{32},$ and 2^{64}. The values for μ_c that are non-analytical ($y = 0.05$ and 0.4)

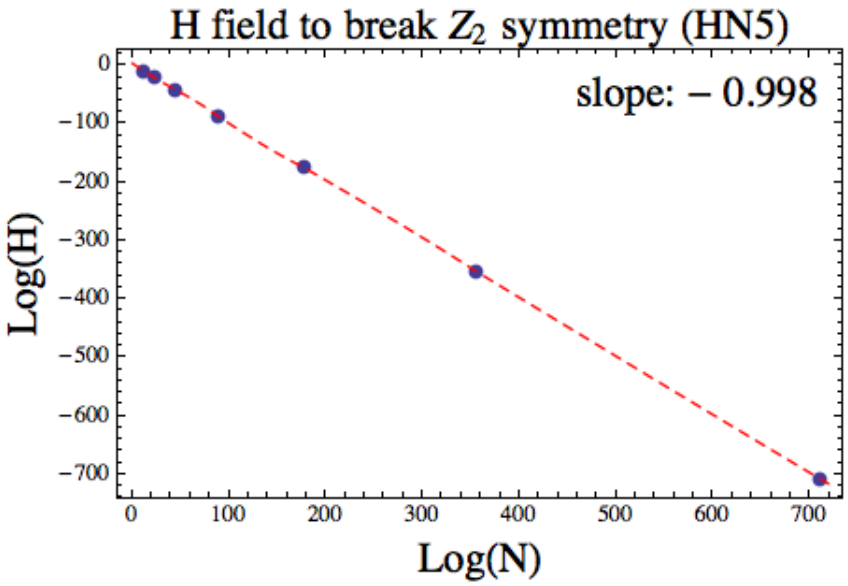

Figure 21: **External magnetic field needed to break the Z_2 symmetry of the Ising model:**Critical temperatures were identified for varying external magnetic fields by locating the sharpest drop in magnetization. The value at which this sudden drop occurs is indicated on the y-axis. The magnetic field required to break the Z_2 symmetry for HN5 scales as $N \sim H$.

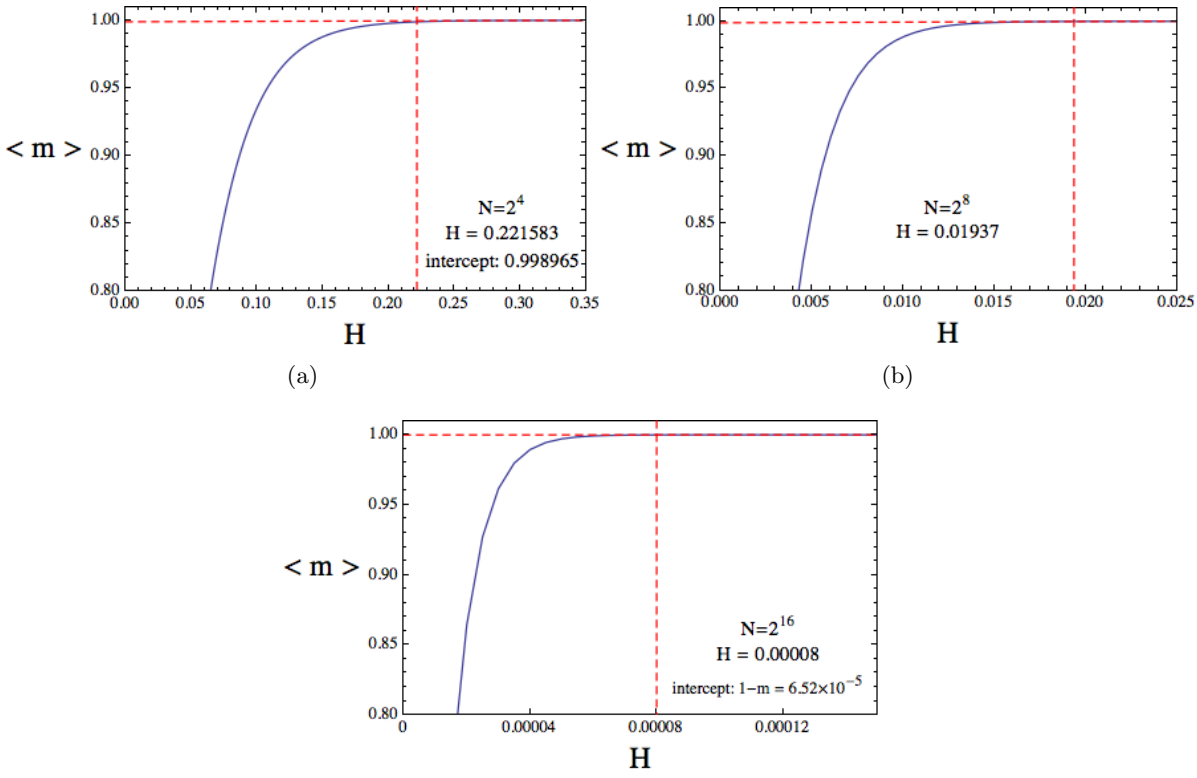

Figure 22: **Breaking the Z_2 symmetry for small system sizes:** For each of the plots shown, the RG was initialized to a low temperature, $\mu = 0.01$, and the external field was allowed to vary. As the field weakens, it no longer has the strength to break the Z_2 symmetry, and the magnetization drops to zero. To determine the minimal H field needed to break the symmetry, a line was extrapolated, and the vertical red dashed line indicates the lowest possible H field needed to study the model.

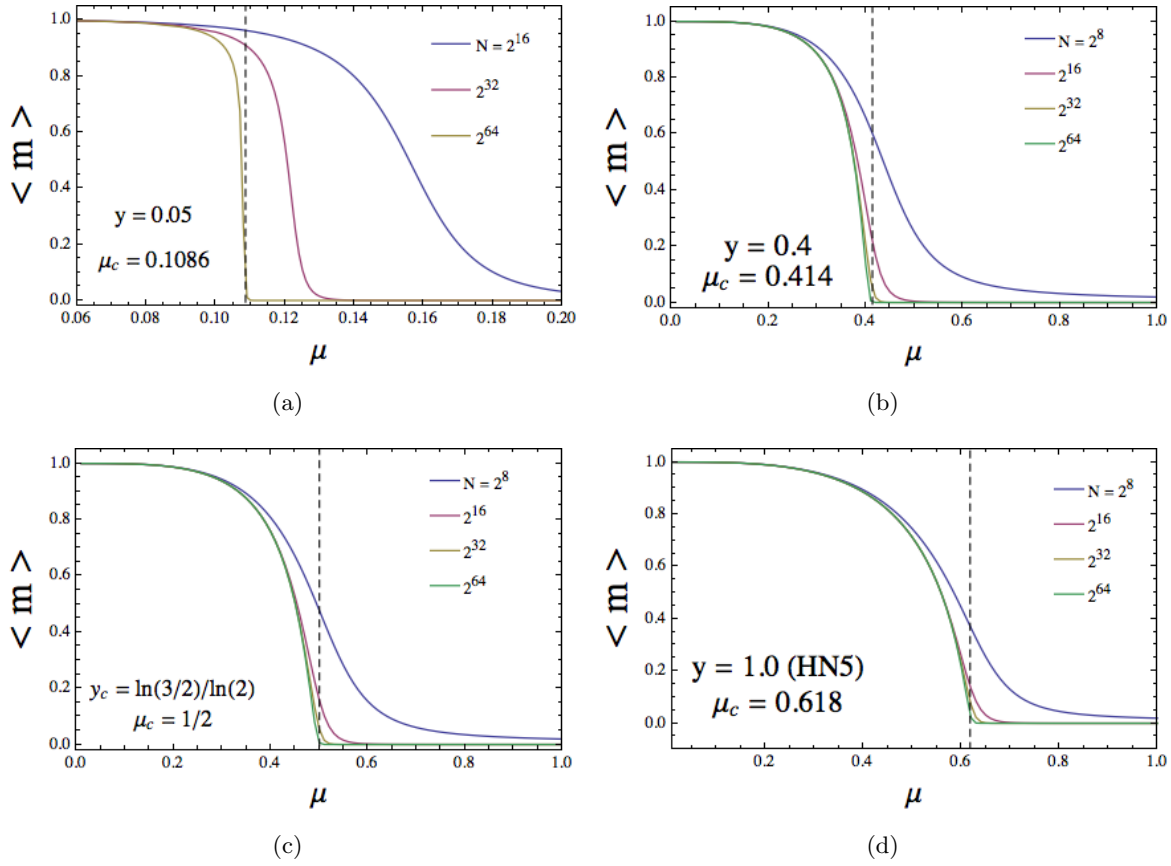

Figure 23: **Magnetization for the interpolation between HN3 and HN5:** The magnetization is plotted for system sizes $N = 2^8, 2^{16}, 2^{32}$ and 2^{64} for $y = 0.05, 0.4, y_c$ and 1. The vertical dashed lines indicate the μ_c for each corresponding y value.

were obtained using a "shooting" method for finding the fixed point of the RG recursion equations. As a first check to see that these are accurate depictions of the magnetization, the location of μ_c in the plots was verified with the μ_c calculated from the recursion equations.

What is immediately obvious from these plots is the speed of convergence to toward μ_c each time N is squared. The magnetization plots for smaller values of y are spread wider and quickly converge to μ_c, where there the phase transition can be described by a power law with a magnetization exponent of $\beta > 0$. As y increases, this convergence toward μ_c becomes much slower with increased system sizes.

Figure 24 gives a closer look at the magnetization near μ_c for the same values of y used in Figure 23. Panel (a) is at $y = 0.05$, near HN3, and appears to be a second-order phase transition in which the β exponent is $0 < \beta < 1$. We can provide a better estimate and prove that it is a first-order phase transition by plotting

$$\begin{aligned} m &\sim |\mu_c - \mu|^{\beta} \\ \log m &\sim \beta \log |\mu_c - \mu| \,. \end{aligned} \tag{109}$$

Figure 25 shows that approaching the critical temperature from below for a system size of $N = 2^{1024}$, β has a value between $0.15 < \beta < 0.20$. As y is increased, the transition point becomes smooth indicating higher-order phase transitions, where there is no longer a single β exponent, but rather $m \sim e^{-\frac{A}{\sqrt{\mu_c - \mu}}}$. The smooth infinite-order phase transition can be seen clearly where even the system size of 2^{1024} in panel (d) is still continuous.

4.7 Magnetic susceptibility and specific heat of Hanoi Networks according to the RG

The two-point functions describe the fluctuations in the system. The magnetic susceptibility is simply the second moment of the magnetization, which is obtained by taking the second

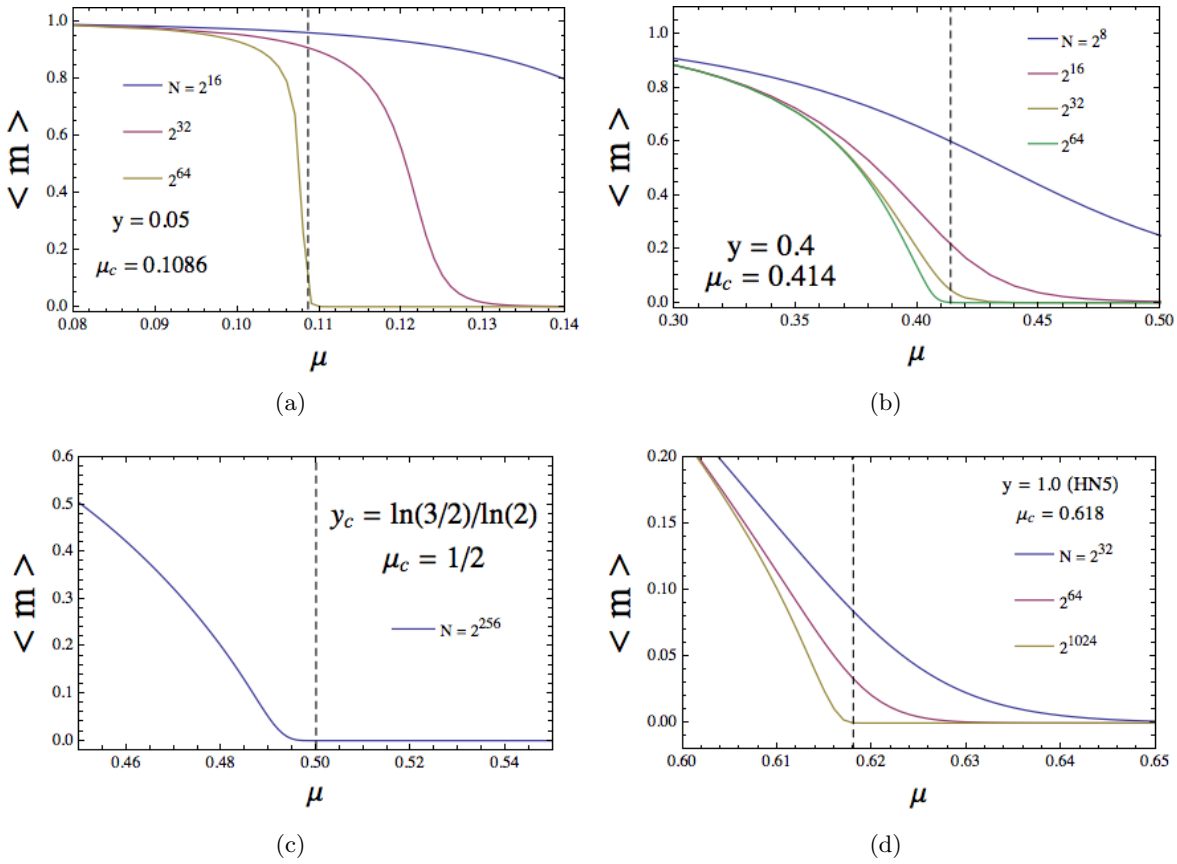

Figure 24: **Magnetization near μ_c for HN3 to HN5:** For the y values in Figure 23, the magnetization is plotted in the vicinity of μ_c. Vertical dashed lines indicate the critical temperature for the corresponding value of y. The magnetization was calculated for all possible temperatures $0 < \mu < 1$. (Panel (a) has been cropped for space.) For each value of y, the RG calculations were carried out for system sizes $N = 2^8$, 2^{16}, 2^{32}, and 2^{64}.

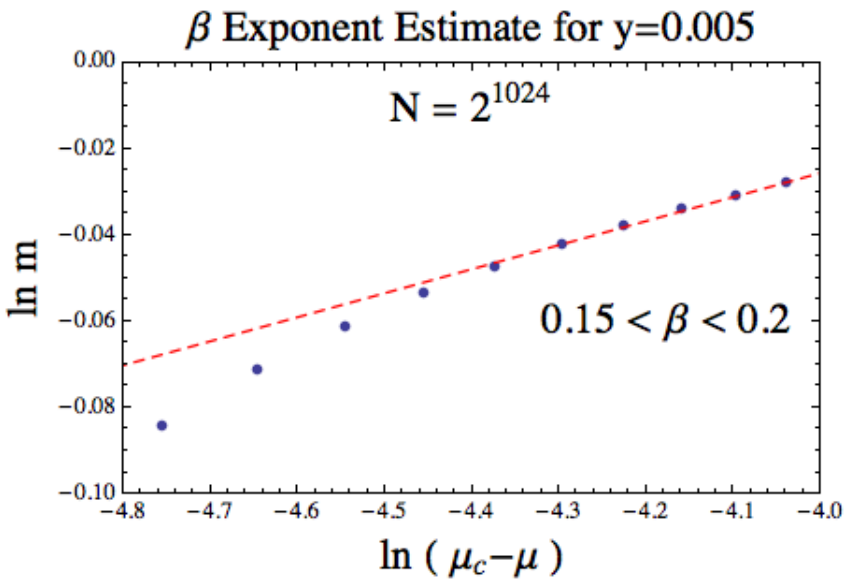

Figure 25: **An estimate for the exponent β at $y = 0.05$:** The magnetization was derived from the RG for $y = 0.05$ for a system size of $N = 2^{1024}$ near μ_c. The slope of the extrapolated line indicates that the value for the exponent $\beta \approx 0.197$.

derivative of the free energy. If the average magnetic moment of the system is described by

$$\langle M \rangle = \frac{1}{\beta} \frac{\partial \log Z}{\partial H} = -\frac{\partial F}{\partial H}, \tag{110}$$

then the fluctuations follow

$$\chi = \frac{1}{\beta} \frac{\partial^2 F}{\partial H^2} = \frac{1}{\beta} \frac{\beta \langle M \rangle}{\partial H} = \langle M^2 \rangle - \langle M \rangle^2 . \tag{111}$$

The procedure for calculating this seemingly simple quantity via the RG for the HN Ising model Hamiltonian is derived in detail in the previous chapter, and here, we provide the results for the y values from Figure 20.

Figure 26 shows the total magnetic susceptibility for the HN3-HN5 interpolation in the different phase transition regimes. We have chosen to plot the logarithm of the susceptibility to view the susceptibility for all system sizes better. Additionally, T is plotted on the abscissa for the purpose of accentuating the susceptibility peaks. As the system size increases, the case for $y = 0.05$ in panel (a) is similar to that of the one-dimensional Ising

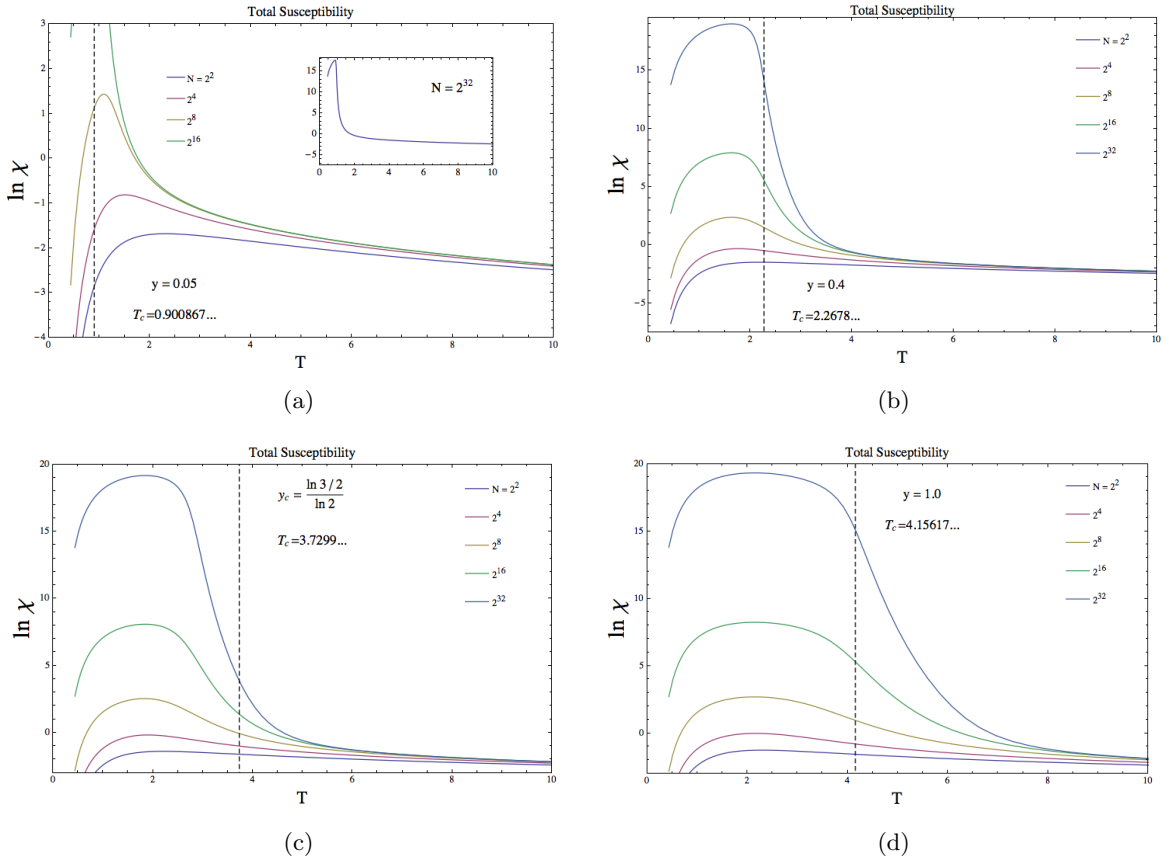

Figure 26: **Total magnetic susceptibility near μ_c for HN3 to HN5:** The total magnetic susceptibility of the system is shown for each y value at different system sizes. From this, it can be easily seen that small y values correspond to the typical behavior found in first-order phase transitions, and as the BKT regime is met, the curvature of the peaks decreases.

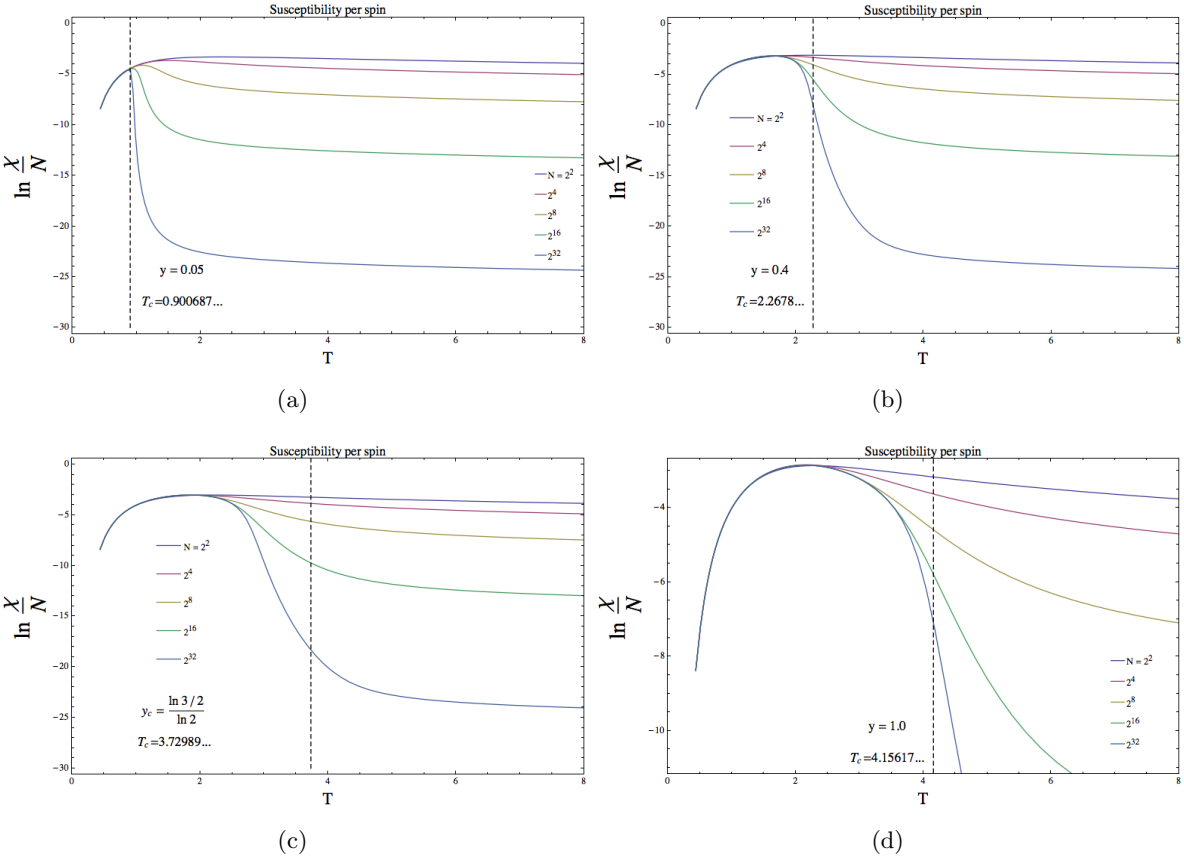

Figure 27: **Magnetic susceptibility per spin near μ_c for HN3 to HN5:** The magnetic susceptibility per spin shows that below T_c, the scaling behaves as $\frac{\chi}{N} \sim N^{\Psi}$ with $\Psi = 1$. In the BKT transition, the splaying of the plots occurs below T_c, which indicates that Ψ takes a different form than for the case of power law scaling.

model, where the peak rises and migrates toward μ_c (T_c). As y is increased and brought into the BKT regime and beyond, the curvature of these peaks decreases, and the convergence toward μ_c is slower each time N is squared.

A more common and perhaps a more insightful measurement is the susceptibility per spin, which is given by the formula

$$\frac{\chi}{N} = \frac{\beta}{N}\left(\langle M^2\rangle - \langle M\rangle^2\right) = \beta N\left(\langle m^2\rangle - \langle m\rangle^2\right). \tag{112}$$

Once again, in Figure 27 we have plotted the logarithm of $\frac{\chi}{N}$ versus the temperature instead

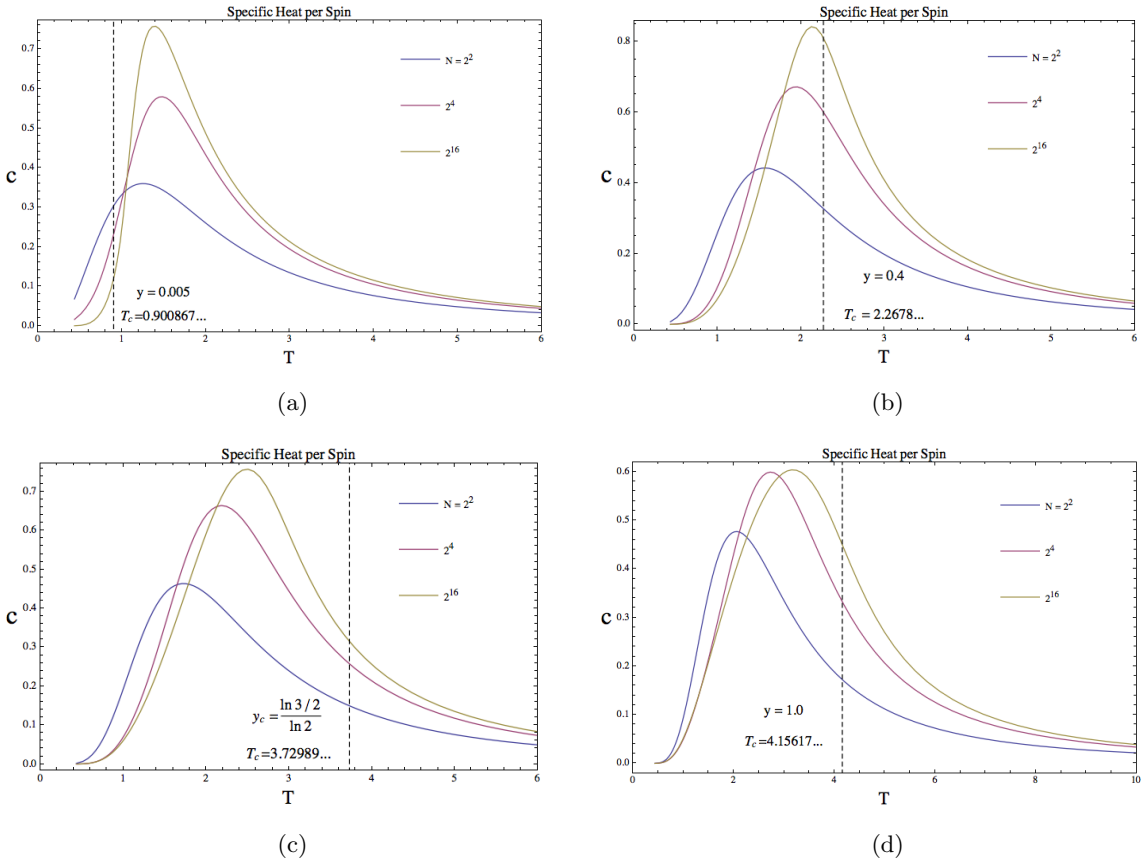

Figure 28: **Specific heat per spin near μ_c for HN3 to HN5:** The specific heat per spin is shown for system sizes $N = 2^2$, 2^4, and 2^{16}. Although larger system sizes are not displayed in this figure, their plots overlap with the $N = 2^{16}$ plot exactly.

of μ to show how the change in shape occurs at the peaks in the plots. For $y = 0.05$, it is clear that if the susceptibility follows $\chi \sim N^{\Psi}$, then below T_c, $\Psi = 1$ and the plot lines collapse. Above T_c, the plot lines splay and Ψ takes on a different value.

This is not quite the case for the BKT regime. Panels (b), (c), and (d) all show that the exponent $\Psi = 1$, but changes well below the T_c. Therefore, for the BKT regime, the exponent Ψ is in the form of a function that is dependent upon both y and μ.

The other two-point operator we will discuss is the specific heat, which is shown in

Figure 28. The specific heat is given by the equation

$$C_V = k\beta^2 \left(\langle E^2 \rangle - \langle E \rangle^2 \right), \tag{113}$$

which describes the thermal fluctuations in the system at a given temperature. Because we are interested in how this quantity scales with the size of the system, we have chosen to plot the specific heat per spin, where the previous equation is simply divided by N.

The system sizes for this series of plots may appear small relative to the preceding figures; however, the numerical results from the RG for $N > 2^16$ produce the exact same results. Thus, the plots for $N = 2^2$ and 2^4 are cases where finite-size effect occur.

This concludes our discussion of the thermodynamic observables that are seen from the HN3-HN5 interpolation. Upon further analysis and after performing more numerical calculations, we can begin to start understanding the variable-dependent critical exponents that dictate the behavior of the BKT transition.

CHAPTER V

APPLYING MONTE CARLO METHODS TO HANOI NETWORKS

The preceding chapters focused exclusively on the technology developed for studying HNs using the RG. With the RG, we are able to achieve results for system sizes near the thermodynamic limit; however, Monte Carlo approaches have the potential for providing insight into much smaller system sizes and can be easily adjusted to fit various models without having to wade through a sea of complex algebraic expressions. While computational time limits Monte Carlo simulations to system sizes $N \approx 2^{17}$ in their current state, they can be used as simple prototypes to verify statistical models on complex networks. Furthermore, Monte Carlo simulations are not required to have a Hamiltonian symmetry needed to close the recursion equations in the RG. This chapter will explain the development of Monte Carlo simulations using the Metropolis and the Wolff algorithms in the chosen language C++.

5.1 The Hanoi Network Data Structure

The Ising model provides the luxury of having only two possible binary states of ± 1, and because the HNs are simply a one-dimensional backbone with long-range edges, the Ising spins can be implemented as a one-dimensional array with values ± 1 for our initial conditions. The simulation can be initialized in a high- or low-temperature state. The low-temperature state is simply the ground state of the Ising model, where all spins are given the same value either $+1$ or -1. ($+1$ was chosen for convenience and code readability.) The high-temperature disordered state can be set by iterating through the array and generating a

floating point random number between 0 and 1. If the random number generator (RNG) returns a value less than 0.5, the array element is assigned a value of -1 and is assigned +1 for returned RNG values greater than 0.5.

As a side note, an alternative data structure was examined, where the HN was stored in an $N \times (M+1)$ two-dimensional array—N being the number of Ising spins and M being the number of bonds of the most connected spin. The first column held the Ising spin values, while the remaining M columns held the nearest-neighbor indices. This turned out to be inefficient due to the overhead of dereferencing pointers and array elements from the data structure and was ultimately abandoned. Instead, we chose to apply a technique that exploits the recursive nature of HNs and its long-range bond structure based on powers of 2.

In both the Metropolis and Wolff algorithms, the first step is to choose a random Ising spin from the one-dimensional array and locate its backbone and long-range neighbors. To maintain a geometric equivalence to the networks constructed by the RG, periodic boundary conditions were not used, and the neighbors of backbone edges that extended beyond the lattice were ignored. For all other spins, the backbone neighbors of spin `n` are located in array `a` at a[`n` $\pm$ `1`].

The long-range neighbors can be found using the formula in Section 1.5.1, $n = 2^i\,(2j+1)$. As before, $i \geq 0$ and denotes the hierarchy level and j denotes the consecutive sites within the hierarchy. This formula constructs the HN3, and recalling that HN5 contains additional long-range neighbors at ± 2, they too must be taken into account. In fact, a scheme can be constructed that allows us interpolate between HN3 and HN5 if we consider the interpolation parameter y to be the probability that the extra HN5 bonds are present. When connecting the spins $n = \pm 2^i$, a random number along the interval $[0, 1]$ is generated and compared with the assigned value of y.

For a spin of index n, its highest hierarchical level is found by counting the number of

times n is evenly divisible by zero. Machine division by 2 is simply a bit shift, which makes this data structure far more efficient than the 2D array. Once the highest hierarchical level, i_{max}, is found, the long-distance neighbors, l, for index n are

$$l = n \pm 2^i \; for \; i_{max} \leq i < 1. \tag{114}$$

This same strategy can be applied to the HNNP-HN6 network models by connecting the $(4j)\,2^i$ and $(4j+1)\,2^i$ nodes to the $(4j+3)\,2^i$ and $(4j+4)\,2^i$ nodes respectively [18].

5.2 The Metropolis and Wolff Algorithms

The Metropolis algorithm, the oldest of the two algorithms, starts with the basic assumption that observables for canonical ensemble distributions are given by their thermal average [22],

$$\langle \mathcal{O} \rangle = \frac{1}{\mathcal{Z}} \sum_s \mathcal{O}\,(s)\, e^{-\mathcal{H}(s)/kT} = \frac{\sum_s \mathcal{O}\,(s)\, e^{-\mathcal{H}(s)/kT}}{\sum_s e^{-\mathcal{H}(s)/kT}} \tag{115}$$

We can sample from different energy states from the Boltzmann distribution with probability $\mathcal{P}(s)$, and include this in the equation above as

$$\frac{\sum_s \left[\mathcal{O}\,(s)\, e^{-\mathcal{H}(s)/kT}/\mathcal{P}(s)\right] \mathcal{P}(s)}{\sum_s \left[e^{-\mathcal{H}(s)/kT}/\mathcal{P}(s)\right] \mathcal{P}(s)} \tag{116}$$

If $\mathcal{P}(s)$ is the Boltzmann distribution, then the factors cancel and we are left with

$$\langle \mathcal{O} \rangle = \frac{1}{M} \sum_i \mathcal{O}(s_i) \tag{117}$$

and the states can be selected from the Boltzmann distribution.

At thermal equilibrium the system moves to a new state according to the probability $\mathcal{P}_{eq}(s) = Z^{-1} e^{-\mathcal{H}(s)/kT}$. To preserve the condition of detailed balance, moving from state $s \rightarrow s'$ requires that

$$\mathcal{P}(s)\mathcal{P}(s \rightarrow s') = \mathcal{P}(s')\mathcal{P}(s' \rightarrow s). \tag{118}$$

Here, $\mathcal{P}(s)$ and $\mathcal{P}(s')$ are the probabilities that the system can be found in states s and s' respectively. $\mathcal{P}(s \rightarrow s')$ and $\mathcal{P}(s' \rightarrow s)$ are the transition probabilities that the state will move from $s \rightarrow s'$ and from $s' \rightarrow s$ respectively [27].

Rearranging Eq. 118 and applying the Boltzmann distribution gives

$$\frac{\mathcal{P}(s \to s')}{\mathcal{P}(s' \to s)} = \frac{A(s \to s')}{A(s' \to s)} = e^{-\beta(E_{s'} - E_s)}, \tag{119}$$

where we have introduced A as the acceptance probability. The optimal algorithm for this case is one where the acceptance ratio is

$$A(s \to s') = \begin{cases} e^{-\beta(E_{s'} - E_s)}, & \text{if } E_{s'} - E_s > 0 \\ 1, & \text{otherwise.} \end{cases} \tag{120}$$

Specifically for the Ising model, the Metropolis algorithm executes the following steps after the lattice is initialized.

Metropolis algorithm for the Ising model:

1. Choose a random spin.
2. Calculate ΔE that would occur from flipping the spin.
3. Generate a random number $0 < r < 1$.
4. If $\Delta E < 0$, flip the spin. Else if $r < e^{-\beta \Delta E}$, flip the spin. Else, goto 1.

To measure the magnetization per spin, we sum the values of the lattice upon initialization and divide by N. Each time a spin s is flipped the magnetization changes as

$$m'\left(s_{\mp} \to s_{\pm}\right) = m \pm \frac{2s}{N}. \tag{121}$$

Of course, magnetization measurements must be taken in intervals where consecutive measurements are from two uncorrelated states. The magnetization autocorrelation function falls exponentially as $\chi_{auto}(t) \sim e^{-t/\tau}$, where t is one Monte Carlo step and τ is the characteristic time used to determine the number of Monte Carlo steps needed to transition to an uncorrelated state. Near T_c, the divergence of the correlation length and critical fluctuations form domains that are difficult for the Metropolis algorithm to flip, because it must do so one spin at a time and spins within the domain are rejected with a high probability.

The Wolff algorithm and other cluster-flipping algorithms address this issue by picking a random spin and forming a cluster from other spins in its domain. These spins are added with a probability $\mathcal{P}_{add} = 1 - e^{-2\beta J}$, and we simply set $J = 1$. Then, the entire cluster is flipped. More formally, the Wolff algorithm executes the following steps:

Wolff algorithm for the Ising model:

1. Choose a random spin, and push its index `n` to stack `s` and to the cluster stack `c`.
2. While `s` is not empty:
   (a) Pop `n` from `s` and locate its neighbors `nn`.
   (b) For each neighbor `nn`:
      - `array[ n ]` = `array[ nn ]` ? (`r` ← `rand()` between 0 and 1) : `null`.
   (c) `r` $< 1 - e^{-2\beta J}$? (push `nn` to `s` and `c`) : `null`
3. Flip the cluster.

To account for the interpolation between HN3 and HN5, the variable y is set globally. Then, when considering the HN5 bonds for the Wolff cluster, the probability that it is added to the cluster is simply, $\mathcal{P}_{add} = 1 - e^{-2\beta J}$

After applying both algorithms to the Hanoi networks in C++, it was evident that the Metropolis algorithm would not be sufficient for studying HNs. At and around the expected critical temperature, the most connected spins in the network had an unreasonably high probability of being rejected, because $\Delta E = E_{s'} - E_s$ was so large. This created characteristic times that were on the order of $\tau \sim 10^8$ near T_c, and the Metropolis algorithm was abandoned altogether. All of the results discussed below were obtained using the Wolff algorithm, which proved to be robust enough to explore the configuration space of the HNs.

5.3 Comparison between Monte Carlo and RG results

Before running the Monte Carlo simulations and recording the results, equilibrium tests were performed for determining whether the lattice should be initialized to $< m >= +1$ or if spins should be randomly assigned with $< m > \approx 0$. To test how quickly each initial condition took to reach equilibrium, the temperature for HN5 was set to $T = 2.0$, where we expect the magnetization per spin to be close to 1.0. Figure 29 shows that after $\approx 12,000$ Monte Carlo steps for a lattice size of 2^{11}, the high-temperature initial condition equilibrated to the same state as the low-temperature initial condition. As the size of the lattice was increased to 2^{13}, however, the initial condition with randomly assigned spins never reached its correct equilibrium state for $T = 2.0$. (See Figure 30.)

Moving on from the initialization of the Monte Carlo simulations, the order parameter used to compare the numerical results with the RG is the magnetization per spin, $< m >= \frac{<M>}{N}$. As stated before, Monte Carlo simulations cannot reach large enough system sizes to pull much meaning out of the general scaling behavior of HNs. Numerical simulations, however, can provide us with an integrity check to ensure that the RG results are well-defined and behave properly.

Figure 31 shows a comparison of the order parameter, $< m >$, between the numerical simulation and the RG for HN5. The solid lines represent RG results for different values of the magnetic field, and the crosses are results from the numerical simulation. It is clear to see that they don't agree. All three RG measurements overshoot the Monte Carlo simulation up to a crossing point temperature, where they then undershoot the simulation. It is surmised that this happens, because the magnetic field needed to break the Z_2 symmetry is not well-defined for the RG. A possible solution would be to replace the external magnetic field with a temperature dependent function in the RG Hamiltonian, $H(T)$.

Neither the specific heat nor the magnetic susceptibility are dependent on an external

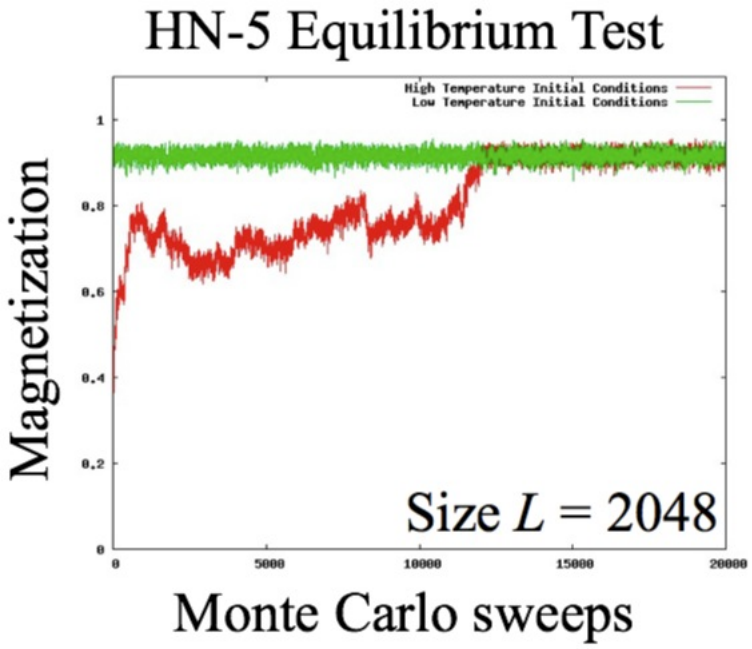

Figure 29: **Equilibration of Monte Carlo simulations ($L = 2048$):** Two Monte Carlo simulations were held at a fixed low temperature, $T < T_c$, with different initial conditions. The green plot indicates the magnetization of a lattice where all spins were initially oriented in the same direction. The red plot is the lattice where spins are initially assigned random values ± 1. For $L = 2048$, the Wolff algorithm eventually brings both initial conditions to the same state after $\sim 10^4$ Monte Carlo lattice sweeps.

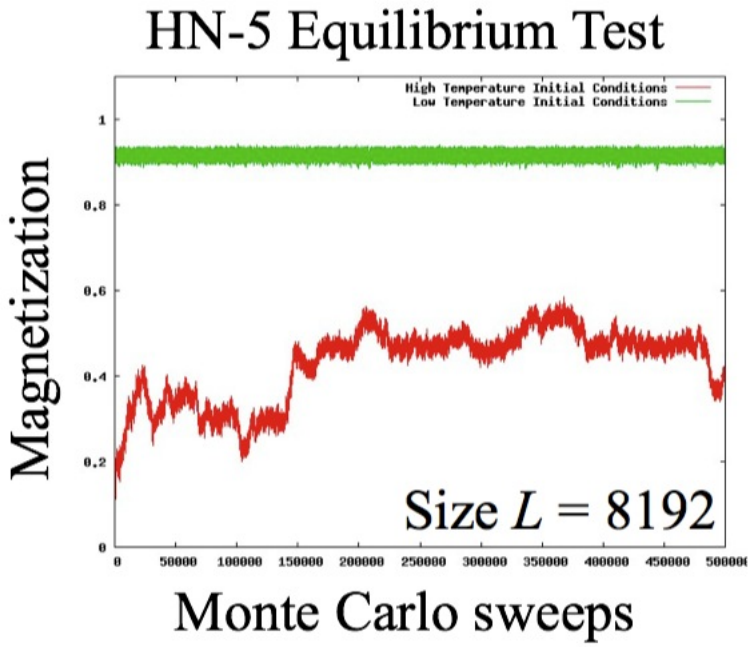

Figure 30: **Equilibration of Monte Carlo simulations ($L = 8192$):** Initializing the lattices the same as in Figure 29, the high-temperature lattice shown in red never reaches its proper low-temperature state for $L = 8192$ even after 10^5 Monte Carlo lattice sweeps.

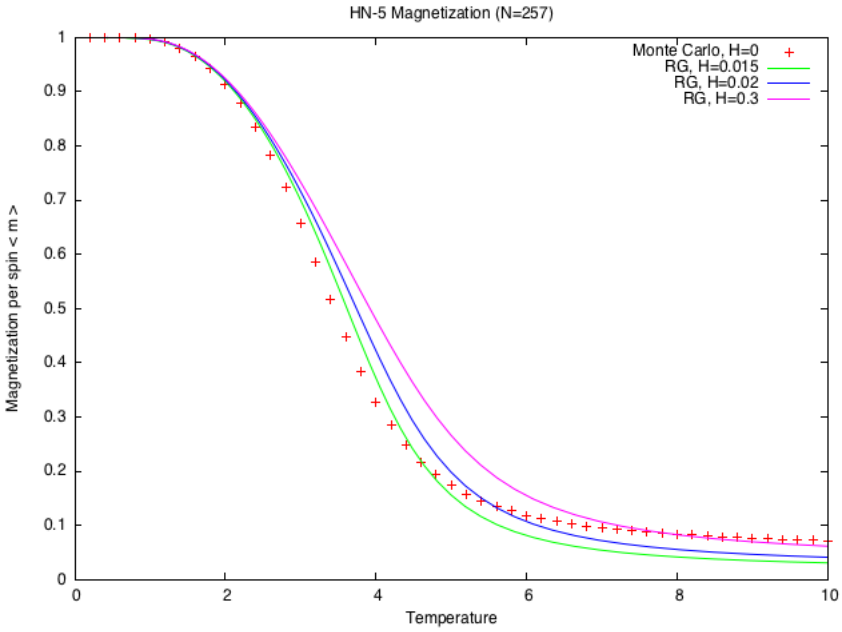

Figure 31: **Comparison of Monte Carlo and RG results for the HN5 magnetization:** A Monte Carlo simulation was carried out for HN5 for $N = 2^8+1$ between $0 < T < 10$, and its magnetization results are indicated with red crosses. As a comparison, the RG was carried out for various external magnetic field strengths needed to break the Z_2 symmetry. The RG calculations do not agree exactly with the Monte Carlo simulation, which is likely be attributed to the field introduced the break the symmetry in the RG equations.

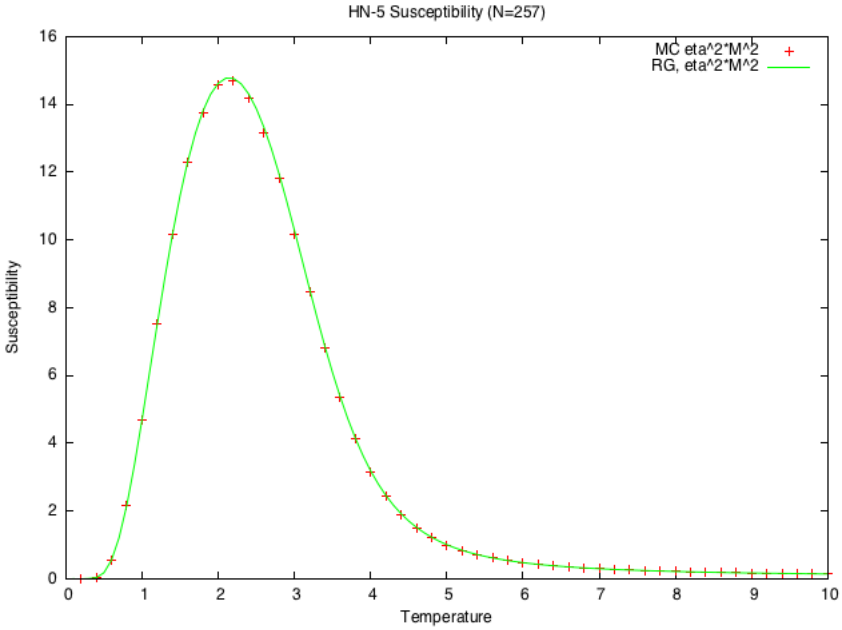

Figure 32: **Magnetic susceptibility comparison between Monte Carlo and the RG on HN5:** For the same Monte Carlo experiment in Figure 31, the fluctuations of the magnetization agree exactly with the results derived from the RG.

magnetic field, and we see much more satisfactory results in the Monte Carlo comparison with the RG. The magnetic susceptibility tells us physically how the system reacts to an external magnetic field. To understand the physical meaning of the units, recall that the magnetic susceptibility is simply a ratio of $\frac{\mathbf{M}}{\mathbf{H}}$. A large susceptibility value indicates that the entire system can respond to or feel the effect of an extremely small magnetic field ($H << 1$).

Another way to view the magnetic susceptibility is to examine the formula

$$\chi = \frac{1}{kT}\left[\left\langle M^2\right\rangle - \left\langle M\right\rangle^2\right]. \tag{122}$$

From this we see that the susceptibility is simply the fluctuations of the magnetization $M = \sum_i \sigma_i$. Plotted as a function of temperature, the susceptibility of our small system size $N = 256$ peaks around $T \approx 2.5$ in Figure 32, and the Monte Carlo results agree with the RG susceptibility.

The specific heat measures the energy fluctuations within the system.

$$C_V = \frac{1}{kT^2}\left[\left\langle \mathcal{H}^2\right\rangle - \left\langle \mathcal{H}\right\rangle^2\right] \tag{123}$$

These thermal fluctuations are what allow the system to move between energy states. Figure 33 once again shows that the results from the Monte Carlo simulation match the specific heat measurement from the RG.

5.4 Other Monte Carlo results and measurements

One specific measurement that can be obtained from Monte Carlo simulations and not with the RG (currently) is the fourth-order cumulant [5, 23], which is the kurtosis of the order parameter.

$$g = \frac{1}{2}\left[3 - \frac{\left\langle m^4\right\rangle}{\left\langle m^2\right\rangle^2}\right] \tag{124}$$

Traditionally, this cumulant, also referred to as the Binder parameter or Binder ratio, is used in numerical simulations to locate T_c. Since we can derive T_c for various values of the

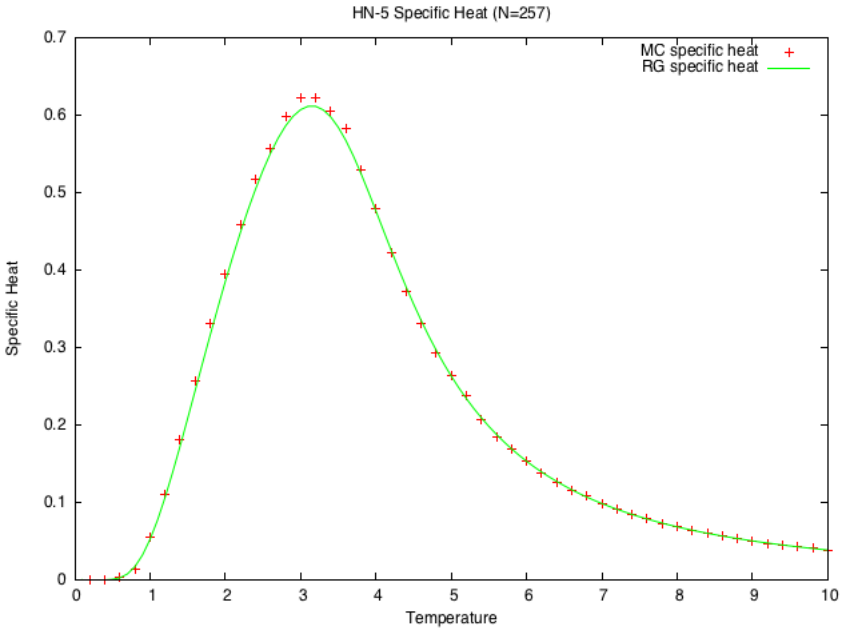

Figure 33: **Specific heat comparison between Monte Carlo and the RG on HN5:** Using the same Monte Carlo results from Figure 31, the specific heat was measured and compared with the RG predictions. Although there is a strong agreement in the majority of temperature values, near the peak, the Monte Carlo results overshoot the RG values. This is likely attributed to an overestimate in energy fluctuations introduced by the Wolff algorithm.

interpolation parameter y in the HNs, this doesn't provide any additional insight that we do not already get from the RG. Example plots of the Binder parameter are shown for the interpolation between HNNP and HN6 in Figure 34. Unfortunately, the Binder parameter crossing points in these graphs are not in agreement with the RG results because of an incorrect interpretation and translation of the y parameter to the Monte Carlo simulation. This is an example of how the Monte Carlo simulations can be coupled with the RG as an integrity check.

Finally, Monte Carlo simulations provide the means to study the largest cluster in the system. We can track individual spins in the system and locate the largest cluster in the system using a similar technique as was used in the Wolff algorithm. The following algorithm was used to identify the largest cluster in the system during simulations.

1. Initialize largest cluster `large` ← zero.
2. Create list `list` containing the integer indices 0 to N
3. While `list` is not empty:
   (a) Pick any element `n` from `list` and find the corresponding Ising spin value in array `a[ n ]`. Remove `n` from `list`, and push `n` to temporary cluster list `temp`.
   (b) Find nearest neighbors `nn` for spin `n`.
   (c) For each `nn`:
   - (`a[ n ] = a[ nn ]`) ? (push `nn` to `temp`. Remove `nn` from `list`) : (`null`).
4. (`temp` > `large`) ? (`large` ← `temp`) : (Goto 3.).

This series of steps will return a list containing the indices of the largest cluster. For this algorithm, it is recommended that the `<list>` data structure from the C++ standard library be used, since removing elements from the middle of the list is computationally faster

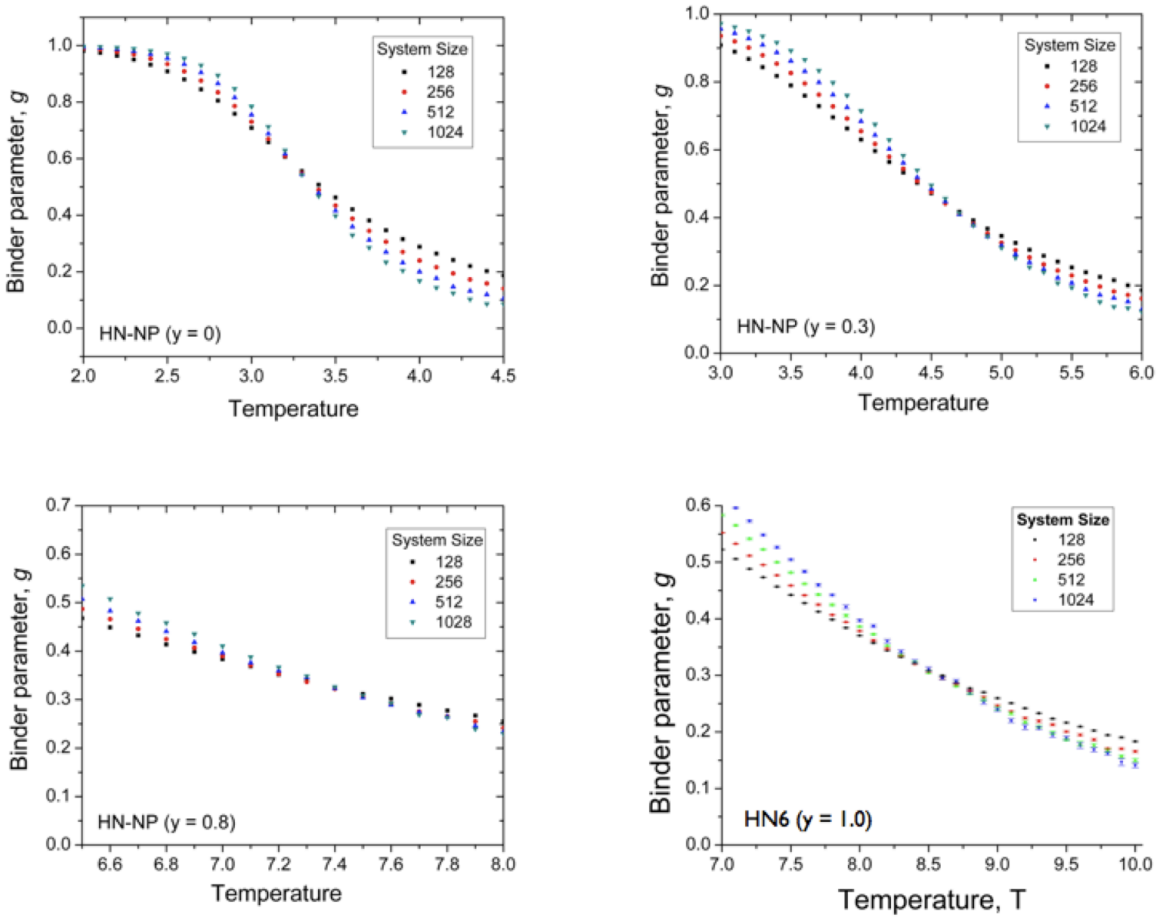

Figure 34: **HNNP-HN6 Binder parameter measurements:** The Binder parameter, which is the kurtosis of the magnetic moment distribution, was calculated for the interpolation between the non-planar HNNP graph and its complimentary graph HN6. The cross-over point for different system sizes occurs at T_c. The results shown here do not agree with the analytical value of T_c derived from the RG, but are simply shown as an example of the behavior of the Binder parameter. The discrepancy is due to a misinterpretation of the y parameter that occurred in the Monte Carlo simulation source code.

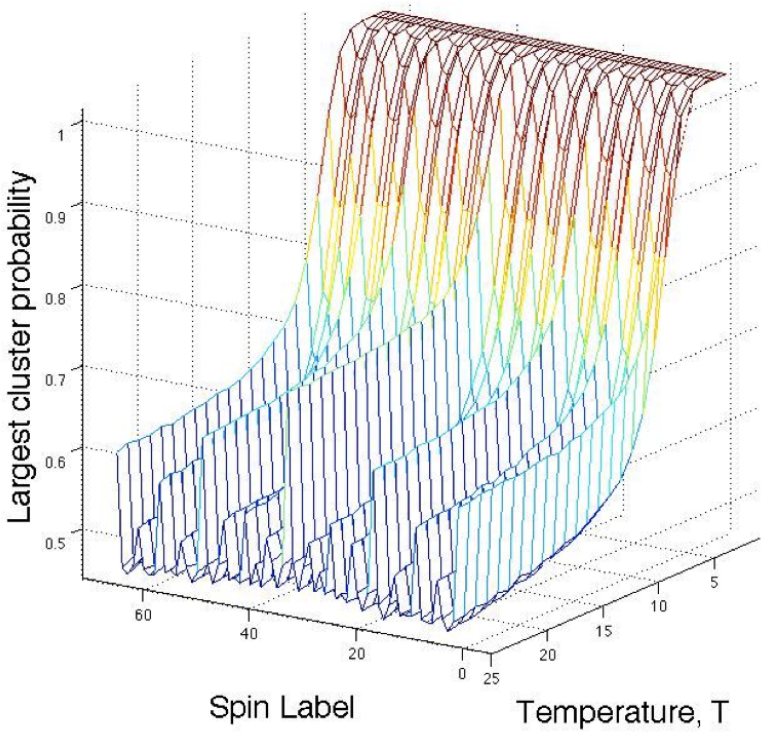

Figure 35: **Distribution of the largest cluster members for HN5:** For a system size $N = 64$, the largest cluster was calculated for temperatures $0 < T < 25$. From this, we see that in the high-temperature regime, the hierarchical nature decomposes, and the probability that highly-connected spins are part of the largest cluster is much higher than lesser-connected spins.

[21] than say a `<vector>`, `<queue>`, or `<deque>`. An example of how the largest cluster can be tracked is shown in Figure 35. At low temperatures, the largest cluster is made up of all spins in the system. As the temperature is increased to $T = 25.0$, the highly-connected spins are far more likely to be part of the largest cluster than the spins with fewer connections.

Although the Monte Carlo simulations aren't able to provide us with the rich results given by the RG, they do offer an insight into smaller system sizes that would be difficult to extract from the RG. The technology developed from this research provides the starting framework for a software package in which statistical physical models can be studied for

HNs and other complex networks. Future development will involve a redesign that utilizes the C++ Boost Graph Library to create a developer- and user-friendly platform.

CHAPTER VI

CONCLUSIONS AND FUTURE WORK

After wading through a considerable amount of technical detail and derivations, it is important to reevaluate the motivation behind studying HNs and summarize the results in a succinct and clear picture as well as discuss the avenues for future research. It is more useful to think of the preceding pages not as a study in Hanoi networks, but as a generalized study of the nature of phase transitions on complex networks, which is the primary objective. The complexity and change in thermodynamic properties that arise when long-range bonds are considered in statistical models is not fully understood, and our study of an exact RG along with the Monte Carlo algorithms provides an arsenal of tools to begin peeling back the layers of complexity.

The most compelling result that was found was that of the three different types of phase transitions that occur on hierarchical networks. Their phase behavior can either exhibit a power law singularity $\xi \sim |T - T_c|^{-\nu}$, a BKT-like transition $\xi \sim e^{-\frac{const.}{\sqrt{|T-T_c|}}}$, or another form of an infinite order transition with an even slower divergence of the correlation length $\xi \sim e^{-\frac{const.}{|T-T_c|}}$. These three types of phase transitions remained a theme throughout. The magnetization plots show that for the interpolation between HN3 and HN5 at $y = 0.05$, there is a first-order phase transition following the scaling law $m \sim |T - T_c|^{\beta}$, where $0 < \beta < 1$. As y is increased the magnetization near T_c becomes smooth indicating higher-order phase transitions and eventually ones that follow an exponential scaling $m \sim e^{-\frac{const.}{|T-T_c|}}$ at HN5. This magnetic susceptibility and specific heat plots follow this same pattern, but what's more important is that this behavior is not exclusively a by-product of HN3-HN5. It has

also been seen to hold true with HNNP-HN6 and with the one- and two-dimensional Migdal-Kadanoff diamond hierarchical lattices. This ultimately led us to form a generic model for the RG for parameter-dependent hierarchical networks.

To play devil's advocate for a brief moment, we ask, "What experiments need to be conducted to verify and study the HN results in a lab setting?" The goal in basic physics research is to combine theoretical models with experiments. In truth, the HNs are not present in nature, but the research presented here does offer a physical interpretation to experiments in which critical exponents are measured and appear to behave as temperature-dependent functions instead of single values. In other words, for experiments exhibiting non-universal behavior, we provided the theoretical foundation for determining whether the system under experiment is hierarchically structured.

This thesis focuses solely on the two-state Ising Hamiltonian, but our immediate future work will concentrate on the q-state Potts model, where the spins in the Ising Hamiltonian are replaced with Kronecker deltas of the form $\delta_{Kr}(\alpha,\beta) = \frac{1}{q}\left[1+(q-1)\,\mathbf{e}^{\alpha}\cdot\mathbf{e}^{\beta}\right]$ from Ref. [37]. Studying this Hamiltonian for the $q=2$ case will yield the same results presented in this work, but the goal is to explore all the symmetries the Hamiltonian can take (all possible values of q) and their behavior as the interpolation parameter y is allowed to vary.

It would be remiss to not discuss the clever work of Tomoaki Nogawa, Takehisa Hasegawa, and Koji Nemoto in their formulation of a generic scaling theory for hierarchical networks. Their work in Ref. [29] considers the scaling formula

$$g\left(\xi(t)^{-1},h,N^{-1}\right) = bg\left(\xi(t)^{-1}b,hb^{y_h},N^{-1}b\right) \tag{125}$$

and from it, derives the complete behavior of the critical exponents for the one-dimensional Migdal-Kadanoff lattice for the q-state Potts model. Our future work looks to incorporate this scaling theory into an in-depth analysis of the scaling exponents for the HNs. From it, we anticipate that the β exponent for the magnetization can be decomposed for interpolated

values between HN3 and HN5.

The study of complex networks must be handled delicately, and physicists must be meticulous in both the measurements they take and the theoretical models they formulate. With no intention of discrediting any of the remarkable work he was accomplished, Alberto Barabasi's work in Ref. [2] is an example of how easy it is to misinterpret the results from complex networks. In this paper, he incorrectly fit the time it takes for a single person to write consecutive emails to a power law $\mathcal{P}(\tau) \sim \tau^{-\alpha}$ with an exponent of $\alpha \simeq 1$. His result has been called into question by Ref. [33] (unpublished) and may be an artifact of the data set. This is a simple example of how interpretations of noisy or unconventional data sets can lead to misleading or wrong results and emboldens the claim that exact RG models should be studied.

Finally, as stated in Chapter 1, there are two different approaches to studying complex networks. One approach takes data given by real world networks and builds models based on assumptions, while the other prefers exact results from artificial hierarchical networks. These are two distinct islands of complex network research that must, and will, eventually be bridged, and it is likely that this bridge will take the form of Monte Carlo simulations. We have established the technology with which to perform numerical simulations on HNs and have successfully implemented the Wolff algorithm, where the results align exactly with the magnetic susceptibility and specific heat. Because the RG results are exact, they can be used as a benchmark to explore other Monte Carlo sampling methods and expose the deficiencies in various algorithms.

APPENDIX I

THE MCKAY-HINCZEWSKI-BERKER APPROACH TO CALCULATING THERMODYNAMIC DENSITIES ON HIERARCHICAL LATTICES

The method calculating thermodynamic observables using the RG was first introduced by McKay and Berker [25] and visited more recently by Hinczewski and Berker [20]. The formalism of the calculation starts by writing the Hamiltonian for the Ising model for the original graphlet

$$-\beta H = G + J \sum_{<ij>} \sigma_i \sigma_j + H_B \sum_{<ij>} (\sigma_i + \sigma_j) + H_S \sum_i \sigma_i \tag{126}$$

and the rescaled graphlet

$$-\beta H' = G' + J' \sum_{<ij>} \sigma_i \sigma_j + H'_B \sum_{<ij>} (\sigma_i + \sigma_j) + H'_S \sum_i \sigma_i \tag{127}$$

The recursion equations are derived by equating the two partition functions and solving for the primed variables.

$$\begin{aligned} G' &= f_G(G, J, H_B, H_S) \\ J' &= f_J(G, J, H_B, H_S) \\ H'_B &= f_{H_B}(G, J, H_B, H_S) \\ H'_S &= f_{H_S}(G, J, H_B, H_S) \end{aligned} \tag{128}$$

Then, using the standard definition of finding the average energy, magnetization, and magnetic susceptibility from the partition function [30],

$$U = \frac{1}{N} \sum_{<ij>} \langle \sigma_i \sigma_j \rangle \tag{129}$$

$$M = \frac{1}{N}\frac{\partial}{\partial H}\log Z \tag{130}$$

and

$$\chi = \lim_{H\to 0}\left(\frac{\partial M}{\partial H}\right) \tag{131}$$

we construct a density-response vector, $\mathbf{V}$, containing all the associated observables.

$$\mathbf{V} = (1,\, U,\, M_B,\, M_S,\, \chi_{BB},\, \chi_{BS},\, \chi_{SS}) \tag{132}$$

The subscript, B, in the preceding equation refers to the magnetization and susceptibility of the bonds, and the S subscript is that of the spins. A recursion relation for the density-response vector is then constructed connecting the first and second derivatives of the rescaled and original variables via a Jacobian recursion matrix, $\mathbf{W}$,

$$\mathbf{V}_\alpha = b^{-d}\sum_\beta \mathbf{V}'_\beta \mathbf{W}_{\beta\alpha} \tag{133}$$

where b^{-d} is the scaling factor and $\mathbf{W}$ contains the derivatives of the recursion equations,

$$\mathbf{W} = \begin{pmatrix} b^d & \frac{\partial G'}{\partial J} & 0 & 0 & \frac{\partial^2 G'}{\partial H_B^2} & \mu\frac{\partial^2 G'}{\partial H_B \partial H_S} & \mu^2\frac{\partial^2 G'}{\partial H_S^2} \\ 0 & \frac{\partial J'}{\partial J} & 0 & 0 & \frac{\partial^2 J'}{\partial H_B^2} & \mu\frac{\partial^2 J'}{\partial H_B \partial H_S} & \mu^2\frac{\partial^2 J'}{\partial H_S^2} \\ 0 & 0 & \frac{\partial H_B'}{\partial H_B} & \frac{\partial H_B'}{\partial H_S} & 0 & 0 & 0 \\ 0 & 0 & 0 & \frac{\partial H_S'}{\partial H_S} & 0 & 0 & 0 \\ 0 & 0 & 0 & 0 & \left(\frac{\partial H_B'}{\partial H_B}\right)^2 & \mu\frac{\partial H_B'}{\partial H_B}\frac{\partial H_B'}{\partial H_S} & \mu^2\left(\frac{\partial H_B'}{\partial H_S}\right)^2 \\ 0 & 0 & 0 & 0 & 0 & \frac{\partial H_B'}{\partial H_B}\frac{\partial H_S'}{\partial H_S} & \mu\frac{\partial H_B'}{\partial H_S}\frac{\partial H_S'}{\partial H_S} \\ 0 & 0 & 0 & 0 & 0 & 0 & \left(\frac{\partial H_S'}{\partial H_S}\right)^2 \end{pmatrix}. \tag{134}$$

In this matrix, $\mu = \sqrt{\frac{N_{nn}}{N_n}}$ is the square root of the ratio of the number of nearest neighbor bonds, N_{nn}, to the number of sites, N_n. Using the initial conditions where H_B, H_S, and G are zero, the $\mathbf{W}$ matrix depends only on the nearest-neighbor coupling constant J. When carrying out Ising model calculations, J is usually set equal to a constant while the

temperature is allowed to vary. The inverse of this–where J is allowed to vary–can also be applied producing the same results in phase behavior. In this case $J \to 0$ corresponds to loose coupling, which is associated with the high-temperature regime, and $J \to \infty$ is tight coupling associated with the low-temperature regime. There is also a non-trivial critical value, J_C, which is related to the critical temperature, T_C, by

$$J_C = \frac{1}{T_C}. \tag{135}$$

For n number of recursion steps Eq. 133 becomes

$$\mathbf{V} = b^{-nd}\mathbf{V}^{(n)} \cdot \mathbf{W}^{(n)} \cdot \mathbf{W}^{(n-1)} \cdot \ldots \cdot \mathbf{W}^{(1)} \tag{136}$$

After evolving Eq. 136 many times and a fixed point is reached, $\mathbf{V} \approx \mathbf{V}'$ and the thermodynamic densities at the trivial fixed points are the solution to the left eigenvector problem

$$\mathbf{V}^* = b^{-d}\mathbf{V}^* \cdot \mathbf{W} \tag{137}$$

The left eigenvector for the Migdal-Kadanoff lattice will now be calculated to illustrate how this is carried out. The $\mathbf{W}$ recursion matrix for the diamond lattice is,

$$\mathbf{W} = \begin{pmatrix} 4 & 2u & 0 & 0 & 4v & \sqrt{6}v & \frac{3}{2}v \\ 0 & 2u & 0 & 0 & -4u^2 & -\sqrt{6}u^2 & -\frac{3}{2}u^2 \\ 0 & 2+2u & \frac{3}{2}u & 0 & 0 & 0 & 0 \\ 0 & 0 & 0 & 1 & 0 & 0 & 0 \\ 0 & 0 & 0 & 0 & (2+2u)^2 & \sqrt{6}u(1+u) & \frac{3}{2}u^2 \\ 0 & 0 & 0 & 0 & 0 & 2+2u & \sqrt{\frac{3}{2}}u \\ 0 & 0 & 0 & 0 & 0 & 0 & 1 \end{pmatrix} \tag{138}$$

where $u = \tanh(2J)$ and $v = 1 + \mathrm{sech}(2J)^2$. By transposing the matrix, the left eigenvalue problem is converted to the more common right eigenvector problem.

$$\left(\mathbf{W^T} - b^d\mathbf{I}\right)\mathbf{V^T} = 0 \tag{139}$$

$$\left(\mathbf{W^T} - 4\mathbf{I}\right)\mathbf{V^T} = 0 \tag{140}$$

If the limit as $J \to \infty$ is taken Eq. 139 is then,

$$\begin{pmatrix} 0 & 0 & 0 & 0 & 0 & 0 & 0 \\ 2 & -2 & 0 & 0 & 0 & 0 & 0 \\ 0 & 0 & 0 & 0 & 0 & 0 & 0 \\ 0 & 0 & -\frac{3}{2} & 3 & 0 & 0 & 0 \\ 4 & -4 & 0 & 0 & 12 & 0 & 0 \\ \sqrt{6} & -\sqrt{6} & 0 & 0 & 2\sqrt{6} & 0 & 0 \\ \frac{3}{2} & -\frac{3}{2} & 0 & 0 & \frac{3}{2} & \sqrt{\frac{3}{2}} & -3 \end{pmatrix} \begin{pmatrix} 1 \\ U \\ M_B \\ M_S \\ \chi_{BB} \\ \chi_{BS} \\ \chi_{SS} \end{pmatrix} = 0 \tag{141}$$

After a row reduction operation, Eq. 141 is then,

$$\begin{pmatrix} 1 & -1 & 0 & 0 & 0 & 0 & 0 \\ 0 & 0 & 1 & -2 & 0 & 0 & 0 \\ 0 & 0 & 0 & 0 & 1 & 0 & 0 \\ 0 & 0 & 0 & 0 & 0 & 1 & -\sqrt{6} \\ 0 & 0 & 0 & 0 & 0 & 0 & 0 \\ 0 & 0 & 0 & 0 & 0 & 0 & 0 \\ 0 & 0 & 0 & 0 & 0 & 0 & 0 \end{pmatrix} \begin{pmatrix} 1 \\ U \\ M_B \\ M_S \\ \chi_{BB} \\ \chi_{BS} \\ \chi_{SS} \end{pmatrix} = 0 \tag{142}$$

And from this it can be easily seen that,

$$\mathbf{V} = \begin{pmatrix} 1, & U = 1, & M_B = \pm 2, & M_S = \pm 1; & \chi_{BB} = 0, & \chi_{BS} = 0, & \chi_{SS} = 0 \end{pmatrix} \tag{143}$$

Applying the same technique in the limit $J \to 0$, the eigenvector is,

$$\mathbf{V} = \begin{pmatrix} 1, & U = 0, & M_B = 0, & M_S = 0; & \chi_{BB} = \infty, & \chi_{BS} = \sqrt{6}, & \chi_{SS} = 1 \end{pmatrix} \tag{144}$$

As a consequence of the mixing of derivatives and the infinity in χ_{BB}, all susceptibilities are infinite above the critical temperature for the Migdal-Kadanoff lattice. This, however,

is not the case for the Hanoi networks, which make them a more physically realistic class of hierarchical networks than the Migdal-Kadanoff lattice. The Hanoi networks can have as many as four types of bonds involved in the RG equations, which makes the **W** more complex, but the same practice is put into place when solving the left eigenvector problem as the Migdal-Kadanoff lattice.

$$\mathbf{W}_{Hanoi} = \begin{pmatrix} b^d & \frac{\partial G'}{\partial J} & \frac{\partial G'}{\partial L} & 0 & 0 & 0 & 0 \\ 0 & \frac{\partial J'}{\partial J} & \frac{\partial J'}{\partial L} & 0 & 0 & 0 & 0 \\ 0 & \frac{\partial L'}{\partial J} & \frac{\partial L'}{\partial L} & 0 & 0 & 0 & 0 \\ 0 & 0 & 0 & \frac{\partial H_B^{'}}{\partial H_B} & \frac{\partial H_B^{'}}{\partial H_S} & \frac{\partial H_B^{'}}{\partial H_L} & \frac{\partial H_B^{'}}{\partial T} \\ 0 & 0 & 0 & \frac{\partial H_S^{'}}{\partial H_B} & \frac{\partial H_S^{'}}{\partial H_S} & \frac{\partial H_S^{'}}{\partial H_L} & \frac{\partial H_S^{'}}{\partial T} \\ 0 & 0 & 0 & \frac{\partial H_L^{'}}{\partial H_B} & \frac{\partial H_L^{'}}{\partial H_S} & \frac{\partial H_L^{'}}{\partial H_L} & \frac{\partial H_L^{'}}{\partial T} \\ 0 & 0 & 0 & \frac{\partial T^{'}}{\partial H_B} & \frac{\partial T^{'}}{\partial H_S} & \frac{\partial T^{'}}{\partial H_L} & \frac{\partial T^{'}}{\partial T} \end{pmatrix} \tag{145}$$

To conserve space, the reader is referred to Ref. [20] for the matrix containing the first and second derivatives of the recursion equations.

For Hanoi networks $b^d = 2$, and the ratio of N_{nn} to N_{nn} for each parameter is 1. Finally the K_1 bonds come in untouched during each RG step. Although they contribute to the primed variables, they are not present in the **W** matrix. As before the transpose of this matrix is taken, and we solve for the left eigenvector.

$$\left(\mathbf{W^T} - 2\mathbf{I}\right)\mathbf{V^T} = 0$$

Using HNNP as an example, we take the limit as $J \to \infty$ and reduce the rows giving the

result.

$$\begin{pmatrix}
1 & 0 & -1 & 0 & 0 & 0 & 0 & 0 & 0 & 0 & 0 & 0 & 0 & 0 & 0 & 0 \\
0 & 1 & -2 & 0 & 0 & 0 & 0 & 0 & 0 & 0 & 0 & 0 & 0 & 0 & 0 & 0 \\
0 & 0 & 0 & 1 & 0 & 0 & -4 & 0 & 0 & 0 & 0 & 0 & 0 & 0 & 0 & 0 \\
0 & 0 & 0 & 0 & 1 & 0 & -2 & 0 & 0 & 0 & 0 & 0 & 0 & 0 & 0 & 0 \\
0 & 0 & 0 & 0 & 0 & 1 & -2 & 0 & 0 & 0 & 0 & 0 & 0 & 0 & 0 & 0 \\
0 & 0 & 0 & 0 & 0 & 0 & 0 & 1 & 0 & 0 & 0 & 0 & 0 & 0 & 0 & 0 \\
0 & 0 & 0 & 0 & 0 & 0 & 0 & 0 & 1 & 0 & 0 & 0 & 0 & 0 & 0 & 0 \\
0 & 0 & 0 & 0 & 0 & 0 & 0 & 0 & 0 & 1 & 0 & 0 & 0 & 0 & 0 & 0 \\
0 & 0 & 0 & 0 & 0 & 0 & 0 & 0 & 0 & 0 & 1 & 0 & 0 & 0 & 0 & 0 \\
0 & 0 & 0 & 0 & 0 & 0 & 0 & 0 & 0 & 0 & 0 & 1 & 0 & 0 & 0 & 0 \\
0 & 0 & 0 & 0 & 0 & 0 & 0 & 0 & 0 & 0 & 0 & 0 & 1 & 0 & 0 & 0 \\
0 & 0 & 0 & 0 & 0 & 0 & 0 & 0 & 0 & 0 & 0 & 0 & 0 & 1 & 0 & 0 \\
0 & 0 & 0 & 0 & 0 & 0 & 0 & 0 & 0 & 0 & 0 & 0 & 0 & 0 & 1 & 0 \\
0 & 0 & 0 & 0 & 0 & 0 & 0 & 0 & 0 & 0 & 0 & 0 & 0 & 0 & 0 & 1 \\
0 & 0 & 0 & 0 & 0 & 0 & 0 & 0 & 0 & 0 & 0 & 0 & 0 & 0 & 0 & 0 \\
0 & 0 & 0 & 0 & 0 & 0 & 0 & 0 & 0 & 0 & 0 & 0 & 0 & 0 & 0 & 0
\end{pmatrix}$$

which corresponds to the eigenvector of the ordered state:

$$\begin{aligned}
\mathbf{V} \quad = \quad & (1, U_J = 2, U_L = 1, M_B = \pm 4, M_S = \pm 2, M_L = \pm 2, T = \pm 1, \\
& \chi_{BB} = 0, \chi_{BS} = 0, \chi_{BL} = 0, \chi_{SB} = 0, \chi_{SS} = 0, \chi_{SL} = 0, \chi_{LB} = 0, \chi_{LS} = 0, \chi_{LL} = 0)
\end{aligned}$$

The disordered eigenvector is

$$\begin{aligned}
\mathbf{V} \quad = \quad & (1, U_J = 0, U_L = 0, M_B = 0, M_S = 0, M_L = 0, T = 0, \\
& \chi_{BB} = 8, \chi_{BS} = 4, \chi_{BL} = 4, \chi_{SB} = 4, \chi_{SS} = 2, \chi_{SL} = 2, \chi_{LB} = 4, \chi_{LS} = 2, \chi_{LL} = 4)
\end{aligned}$$

Once the eigenvectors have been determined for the cases $J \to \infty$ and $J \to 0$, a temperature, T, is chosen and $J = 1/T$ is inserted into the recursion equations. The equations are then

evolved i number of times until a fixed point is reached, and each calculated value of J_i is stored into a vector. Starting with the fixed point eigenvector $\mathbf{V}_{J\to 0}$, the i^{th} value of J_i is plugged into the $\mathbf{W}$ matrix, and a new thermodynamic density vector is calculated from the recursion relation in Eq. 133.

$$\mathbf{V}^{(i-1)} = b^{-d}\mathbf{V}^{(i)}\mathbf{W}^{(i)} \tag{146}$$

This process is continued i times, and the value of $\mathbf{V}^{(0)}$ will containing the original (unscaled) values of the thermodynamic densities for each temperature, T, chosen.

A pseudocode for calculating the thermodynamic densities follows:

Write down partition function for original graphlet;

Write down partition function for rescaled graphlet;

Sum over odd spins;

Solve for primed variables creating the recursion equations;

Calculate 1^{st} and 2^{nd} derivatives for $\mathbf{W}$ matix elements;

Fill in elements of $\mathbf{W}$ matrix and take limits, $G \to 0$, $H_S \to 0$, $H_B \to 0$;

$\lim_{J\to\infty} \left[(Transpose\,\mathbf{W}) - \left(b^d \times Identity\,Matrix\right)\right]$;

RowReduce %;

Eigenvector %;

V = (Determined from Eigenvector result);

Set beginning temperature, T;

While (Temperature < Final Temperature) {

Mathematica RecurrenceTable[

$$G[n+1] = f_G\left(G[n],\, J[n],\, H_B[n],\, H_S[n]\right)$$

$$J[n+1] = f_J\left(G[n],\, J[n],\, H_B[n],\, H_S[n]\right)$$

$$H_B[n+1] = f_{H_B}\left(G[n],\, J[n],\, H_B[n],\, H_S[n]\right)$$

$$H_S[n+1] = f_{H_S}\left(G[n],\, J[n],\, H_B[n],\, H_S[n]\right)$$

];

For (i = 0; i < n; i++) { $\mathbf{V} = b^{-d}\mathbf{V} \cdot \mathbf{W}(J[i])$; }

Print $\mathbf{V}$;

Temperature++;

}

The result of implementing this pseudocode in Mathematica is a vector, $\mathbf{V}$, that contains the values of the thermodynamic observables, and the script is iterated over a temperature range.

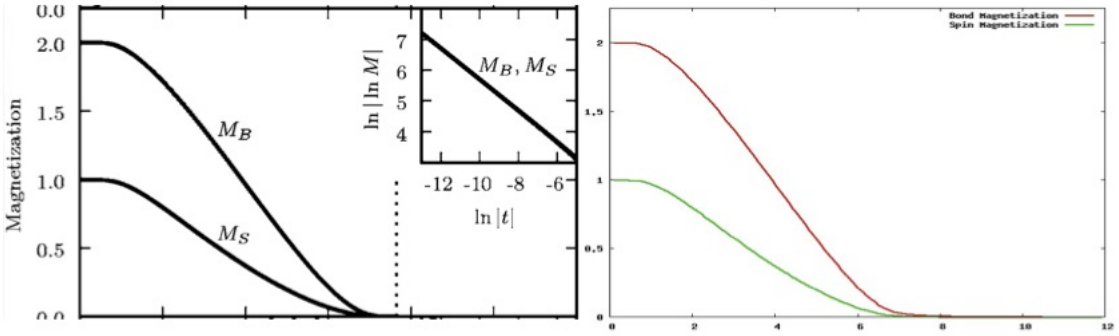

Figure 36: **Reproduction of magnetization results from Ref. [19]:** The left panel shows the magnetization for the long-range diamond hierarchical lattice from Ref. [19]. The steps described in this appendix section were carried out and confirmed the results from their paper.

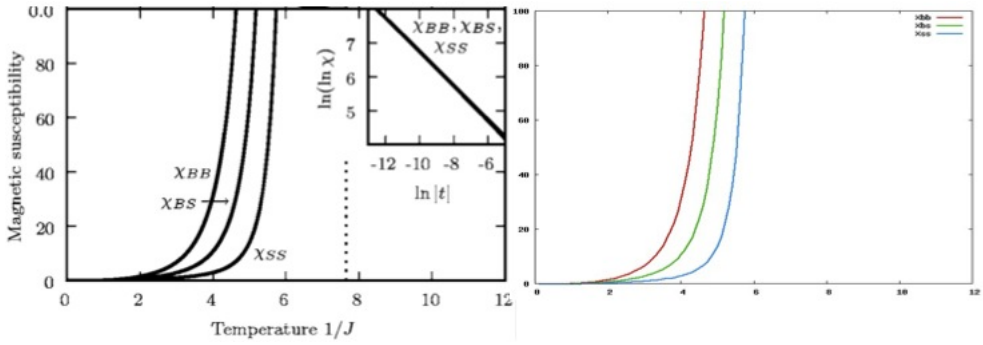

Figure 37: **Reproduction of susceptibility results from Ref. [19]:**

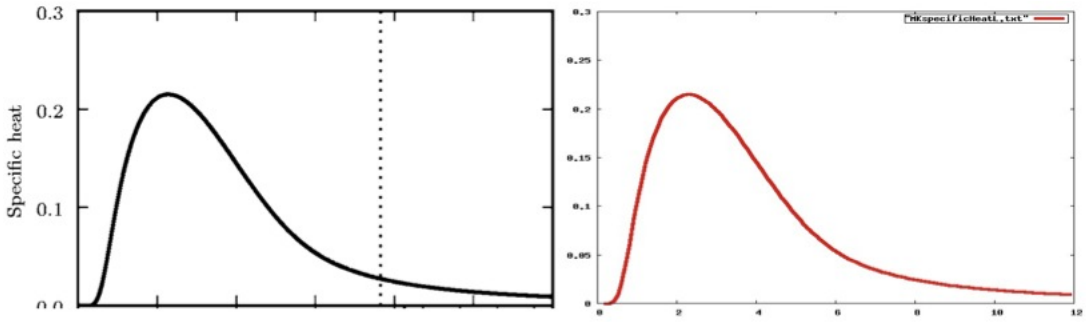

Figure 38: **Reproduction of specific heat results from Ref. [19].**

APPENDIX II

USEFUL MATHEMATICA COMMANDS

This section provides the reader a point from which to start analyzing the RG equations using Mathematica. For readability, commands are indicated with the prompt symbol, >.

B.1 Solving for HN3/HN5 fixed points:

$$> \textbf{Together}\,[\,\textbf{FullSimplify}\,[\,\textbf{Solve}\,[\,\{\kappa==\kappa*\lambda*\frac{2*(1+\mu)}{\kappa^2+2*\mu*\kappa+1},\ \lambda==\mu^{2*y}*\frac{(1+\kappa)^2(1+\mu)}{2*(1+2*\mu*\kappa+\kappa^2)}\,\}\,,\{\kappa,\lambda\}\,]\,,\ \textbf{Assumptions}\to\mu>0\ \&\&\ y>0\ \&\&\ \lambda>0\ \&\&\ \kappa>0\,]\,]$$

B.2 Eliminating μ to derive closed-form expression:

$$> \textbf{Solve}\left[\lambda==\mu^{2*y}*\frac{(1+\kappa)^2(1+\mu)}{2*(1+2*\mu*\kappa+\kappa^2)},\kappa\right]$$

$$> \textbf{Solve}\left[\kappa==\kappa*\lambda*\frac{2*(1+\mu)}{\kappa^2+2*\mu*\kappa+1},\kappa\right]$$

After extracting the correct solutions, μ is eliminated with:

$$> \textbf{Eliminate}\,[\,\{\lambda==\frac{1}{4}\mu\left(2+(-1+\mu)\mu+\sqrt{(1+\mu)(-4+\mu(8+(-3+\mu)\mu))}\right),\ \kappa==\frac{1}{2}\left(-\mu+\mu^2+\sqrt{-4+4\mu(1+\mu)+(-2\mu+\mu(1+\mu))^2}\right)\,\},\ \mu]$$

Solving the result for λ gives the closed-form expression of the fixed-point equations:

$$\lambda^* = \frac{1}{4}\left(-1 + \kappa^* + \sqrt{5 + 2\kappa^* + 5\kappa^{*2} + 4\kappa^{*3}}\right) \tag{147}$$

B.3 Plotting the κ dependency on μ for HN5

$$\begin{aligned}
&> \textbf{Plot}\,[\,\{\mu, \frac{1}{2}\left(-\mu + \mu^2 + \sqrt{-4 + 4\mu(1+\mu) + (-2\mu + \mu(1+\mu))^2}\right)\,\}\,, \{\mu, 0, 1\,\},\\
&\quad \textbf{Frame} \to \textbf{True}, \textbf{PlotRange} \to \{\{0,1\},\{0,1\}\}, \textbf{PlotStyle} \to \textbf{Thickness}[0.0075],\\
&\quad \textbf{FrameLabel} \to \{\textbf{Style}[\mu, \textbf{FontSize} \to 24], \textbf{Style}[\kappa, \textbf{FontSize} \to 24]\},\\
&\quad \textbf{Epilog} \to \{\textbf{Arrow}[\{\{0.1, 0.1\}, \{0.1, 0\}\}],\\
&\quad \textbf{Arrow}[\{\{0.2, 0.2\}, \{0.2, 0\}\}], \textbf{Arrow}[\{\{0.3, 0.3\}, \{0.3, 0\}\}],\\
&\quad \textbf{Arrow}[\{\{0.4, 0.4\}, \{0.4, 0\}\}], \textbf{Arrow}[\{\{0.5, 0.5\}, \{0.5, 0\}\}],\\
&\quad \textbf{Arrow}[0.6, 0.6, 0.6, 0],\\
&\quad \textbf{Arrow}\,[\,\{\,\{0.7, 0.7\}, \{\,0.7, \frac{1}{2}\left(-\mu + \mu^2 + \sqrt{-4 + 4\mu(1+\mu) + (-2\mu + \mu(1+\mu))^2}\right)\\
&\qquad\qquad /.\mu \to 0.7\,\}\,\}\,]\,,\\
&\quad \textbf{Arrow}\,[\,\{\,\{0.8, 0.8\}, \{\,0.8, \frac{1}{2}\left(-\mu + \mu^2 + \sqrt{-4 + 4\mu(1+\mu) + (-2\mu + \mu(1+\mu))^2}\right)\\
&\qquad\qquad /.\mu \to 0.8\,\}\,\}\,]\,,\\
&\quad \textbf{Arrow}\,[\,\{\,\{0.9, 0.9\}, \{\,0.9, \frac{1}{2}\left(-\mu + \mu^2 + \sqrt{-4 + 4\mu(1+\mu) + (-2\mu + \mu(1+\mu))^2}\right)\\
&\qquad\qquad /.\mu \to 0.9\,\}\,\}\,]\,,
\end{aligned}$$

B.4 Calculating y_c

$$\begin{aligned}
&> \textbf{FindRoot}\,[\,\{0 == \frac{1}{2}\,(\,\mu^y + \mu\,(\,-2 + \mu^y\,)\,)\,, \frac{\mu^{2y}}{2}(1+\mu) == \frac{\mu^y}{2}(1-\mu) + \frac{\mu^{2y}}{4}(1+\mu)\,\}\,,\\
&\qquad \{\{\mu, 0.001\}, \{y, 0.001\}\}\,]
\end{aligned}$$

REFERENCES

[1] L.A.N. Amaral, A. Scala, M. Barthelemy, and H.E. Stanley. Classes of small-world networks. *Proc. Nat. Acad. Sci.*, 97:11149–11152, 2000.

[2] A.-L. Barabasi. The Origin of Bursts and Heavy Tails in Human Dynamics. *Nature*, 435:207–211, 2005.

[3] A.-L. Barabasi and R. Albert. Emergence of scaling in random networks. *Science*, 286:509–512, 1999.

[4] Albert-Laszlo Barabasi. *Linked: How Everything Is Connected to Everything Else and What It Means for Business, Science, and Everyday Life*. Plume Books, April 2003.

[5] K. Binder. Critical properties from Monte Carlo coarse graining and renormalization. *Phys. Rev. Lett.*, 47:693, 1981.

[6] S. Boccaletti, V. Latora, Y. Moreno, M. Chavez, and D.-U. Hwang. Complex networks: Structure and dynamics. *Phys. Rep.*, 424:175, 2006.

[7] S. Boettcher and C. T. Brunson. Renormalization group for critical phenomena in complex networks. *Frontiers in Physiology*, 2, 102:1–8, 2011.

[8] S. Boettcher, J. L. Cook, and R. M. Ziff. Patchy percolation on a hierarchical network with small-world bonds. *Phys. Rev. E*, 80:041115, 2009.

[9] S. Boettcher and B. Goncalves. Anomalous diffusion on the Hanoi networks. *Europhysics Letters*, 84:30002, 2008.

[10] Stefan Boettcher, Bruno Goncalves, and Julian Azaret. Geometry and dynamics for hierarchical regular networks. *Journal of Physics A: Mathematical and Theoretical*, 41(33):335003, 2008.

[11] Stefan Boettcher and Alexander K. Hartmann. Optimal vertex cover for the small-world Hanoi networks. *Phys. Rev. E*, 84:011108, 2011.

[12] Stefan Boettcher, Vijay Singh, and Robert M. Ziff. Ordinary percolation with discontinuous transitions. *Nature Communications*, 3:787, 2012.

[13] S. Buldyrev, R. Parshani, G. Paul, H. E. Stanley, and S. Havlin. Catastrophic cascade of failures in interdependent networks. *Nature*, 464:1025–1028, 2010.

[14] S. N. Dorogovtsev, A. V. Goltsev, and J. F. F. Mendes. Critical phenomena in complex networks. *Rev. Mod. Phys.*, 80:1275–1335, 2008.

[15] Stephen E. Fienberg. A brief history of statistical models for network analysis and open challenges. *Journal of Computational and Graphical Statistics*, 21, 4, 2012.

[16] N. Goldenfeld. *Lectures on Phase Transitions and the Renormalization Group*. Addison-Wesley, Reading, 1992.

[17] Harvey Gould and Jan Tobochnik. *Statistical and Thermal Physics: With Computer Applications*. Princeton University Press, Princeton, 2010.

[18] Takehisa Hasegawa and Tomoaki Nogawa. Absence of the nonpercolating phase for percolation on the nonplanar Hanoi network. *Phys. Rev. E*, 87:032810, 2013.

[19] M. Hinczewski and A. N. Berker. Inverted berezinskii-kosterlitz-thouless singularity and high-temperature algebraic order in an ising model on a scale-free hierarchical-lattice small-world network. *Phys. Rev. E*, 73:066126, 2006.

[20] M. Hinczewski and A. N. Berker. Inverted Berezinskii-Kosterlitz-Thouless singularity and high-temperature algebraic order in an Ising model on a scale-free hierarchical-lattice small-world network. *Phys. Rev. E*, 73:066126, 2006.

[21] Nicolai M. Josuttis. *The C++ Standard Library: A Tutorial and Reference.* Addison Wesley Longman, 2012.

[22] H. G. Katzgraber. Introduction to Monte Carlo Methods. http://arxiv.org/pdf/0905.1629.pdf.

[23] D.P. Landau and K. Binder. *A Guide to Monte-Carlo Simulations in Statistical Physics.* Cambridge University Press, 2009.

[24] Franklin de Lima Marquezino, Renato Portugal, and Stefan Boettcher. Spatial search algorithms on Hanoi networks. *Phys. Rev. A*, 87:012329, 2013.

[25] S. R. McKay and Berker. Magnetic susceptibilities of cluster-hierarchical models. *Phys. Rev. B*, 29:1315–1320, 1984.

[26] Stanley Milgram. The small world problem. *Psychology Today*, 1:60–67, 1967.

[27] M.E.J. Newman and G.T. Barkema. *Monte Carlo Methods in Statistical Physics.* Oxford University Press, 2006.

[28] T. Nogawa, T. Hasegawa, and K. Nemoto. Criticality governed by the stable renormalization fixed point of the ising model in the hierarchical small-world network. *Phys. Rev. E*, 86:030102, 2012.

[29] Tomoaki Nogawa, Takehisa Hasegawa, and Koji Nemoto. Generalized scaling theory for critical phenomena including essential singularities and infinite dimensionality. *Phys. Rev. Lett.*, 108:255703, 2012.

[30] R. K. Pathria. *Statistical Mechanics, 2nd Ed.* Butterworth-Heinemann, 1996.

[31] M. Plischke and B. Bergersen. *Equilibrium Statistical Physics, 2nd edition.* World Scientifc, Singapore, 1994.

[32] C.P. Poole Jr. R.J. Creswick, H.A. Farach. *Introduction to Renormalization Group Methods in Physics.* John Wiley & Sons, Inc., 1992.

[33] Daniel B. Stouffer, R. Dean Malmgren, and Luis A. N. Amaral. Log-normal statistics in e-mail communication patterns. http://arxiv.org/abs/physics/0605027.

[34] D. J. Watts and S. H. Strogatz. Collective dynamics of 'small-world' networks. *Nature*, 393:440–442, 1998.

[35] Duncan J. Watts. The "New" Science of Networks. *Annu. Rev. Sociol.*, 30:243–270, 2004.

[36] Kenneth G. Wilson. Renormalization Group and Critical Phenomena. i. Renormalization Group and the Kadanoff Scaling Picture. *Phys. Rev. B*, 4, 9:3174–3183, 1971.

[37] F.Y. Wu. The Potts models. *Rev. Mod. Phys.*, 54:235–268, 1982.